Development of Models for Optical Instrument Transformers

by

Sadik Kucuksari

A Dissertation Presented in Partial Fulfillment
of the Requirements for the Degree
Doctor of Philosophy

ARIZONA STATE UNIVERSITY

December 2010

Development of Models for Optical Instrument Transformers

by

Sadik Kucuksari

has been approved

September 2010

Graduate Supervisory Committee:

George G. Karady, Chair
Gerald T. Heydt
Keith Holbert
Raja Ayyanar
Richard Farmer

ACCEPTED BY THE GRADUATE COLLEGE

ABSTRACT

Optical Instrument Transformers (OIT) have been developed as an alternative to traditional instrument transformers (IT). The question "Can optical instrument transformers substitute for the traditional transformers?" is the main motivation of this study. Finding the answer for this question and developing complete models are the contributions of this work.

Dedicated test facilities are developed so that the steady state and transient performances of analog outputs of a magnetic current transformer (CT) and a magnetic voltage transformer (VT) are compared with that of an optical current transformer (OCT) and an optical voltage transformer (OVT) respectively. Frequency response characteristics of OIT outputs are obtained. Comparison results show that OITs have a specified accuracy of 0.3% in all cases. They are linear, and DC offset does not saturate the systems. The OIT output signal has a 40~60 μs time delay, but this is typically less than the equivalent phase difference permitted by the IEEE and IEC standards for protection applications. Analog outputs have significantly higher bandwidths (adjustable to 20 to 40 kHz) than the IT. The digital output signal bandwidth (2.4 kHz) of an OCT is significantly lower than the analog signal bandwidth (20 kHz) due to the sampling rates involved. The OIT analog outputs may have significant white noise of 6%, but the white noise does not affect accuracy or protection performance. Temperatures up to 50^{o}C do not adversely affect the performance of the OITs.

Three types of models are developed for analog outputs: analog, digital, and complete models. Well-known mathematical methods, such as network synthesis and Jones calculus methods are applied. The developed models are compared with experiment results and are verified with simulation programs. Results show less than 1.5% for OCT and 2% for OVT difference and that the developed models can be used for power system simulations and the method used for the development can be used to develop models for all other brands of optical systems. The communication and data transfer between the all-digital protection systems is investigated by developing a test facility for all digital protection systems. Test results show that different manufacturers' relays and transformers based on the IEC standard can serve the power system successfully.

ACKNOWLEDGMENTS

I would like to thank Power Engineering Research Center (PSERC) for providing me an opportunity to perform this research work. I am deeply grateful to my advisor, Dr. George G. Karady, for his advice, feedback, and direction. His expertise and approach have been significant in performing this research work. I appreciate the contributions of Dr. Farnoosh Rahmatian, Dr. Allen Rose, and Dr. Jim Blake at NxtPhase towards this research. I would also like to thank the members of my supervisory committee, Dr. Gerald T. Heydt, Dr. Keith Holbert, Dr. Raja Ayyanar, and Prof. Richard Farmer, for their time and support. I am pleased to acknowledge the help of people including but not limited to Dr. Emre Araci, Dr. Omer D. Guney, Osman Erol, Yunus Emre, the faculty of the power systems group, and students and staff at Arizona State University. I also would like to thank my father Cengiz Kucuksari, my mother Ayfer Kucuksari, my brother Mehmet Kucuksari, and my wife Gulsum Kucuksari for their endless support and patience.

TABLE OF CONTENTS

Page

APPENDIX

LIST OF TABLES

LIST OF FIGURES

Figure Page

Figure Page

Figure Page

NOMENCLATURE

CT	current transformer
EMTP	electromagnetic transient program
EOVT	electro-optic voltage transducer
FFT	fast Fourier transform
FOCS	fiber-optic current sensor
FR	frequency response
GIS	gas insulated switchgear
HEA	high-energy analog
HV	high voltage
IT	instrument transformer
JEC	Japan electric commission
LEA	low-energy analog
LED	light emitting diode
LTI	linear time invariant
MOCT	magneto-optical current sensor
NIST	National Institute of Standards and Technology
NXCT	NxtPhase current transformer
NXVCT	NxtPhase voltage and current transformer
NXVT	NxtPhase voltage transformer
OCT	optical current transformer
OIT	optical instrument transformer
OVT	optical voltage transformer
PM	polarization maintaining
rms	root mean square
TGG	terbium gallium garnet

VCVS	voltage controlled voltage source
VT	voltage transformer

CHAPTER 1

INTRODUCTION TO OPTICAL INSTRUMENT TRANSFORMERS

1.1 Statement of Problem and Motivation

Traditional measurement and protection systems consist of instrument transformers (IT), such as magnetic current transformers (CT) and voltage transformers (VT). ITs are used for conversion of voltage and current from one level to another [1]. The primary sides of the instrument transformers are supplied by the network voltage and current. The secondary side supplies the protection relays or energy measurement systems. Signals generated by the ITs are transported through electrical cables to the substation control room.

Magnetic instrument transformers have an iron core in order to convert the primary signal to a secondary manageable signal level (5 A or 1 A for CT and 120 V for VT). The performances of magnetic instrument transformers have been investigated for many years for protection and measurement applications by evaluating the secondary signals. When the magnetic core is saturated, the secondary signals are distorted. Therefore, the protection and measurement system performance is affected since the distorted signals are incorrect information for the relays. In addition, the bandwidth of the magnetic transformers is limited and unable to generate proper signals for the relays above certain frequencies. Furthermore, power system transient studies have been simulated for many years with successfully developed models of CTs and VTs.

The development of digital technology has impacted power systems as well. Optical instrument transformers (OIT) are an example of digital system applications in power systems. They have become more available and continue to develop over time. They are also called electronic transformers since their hardware is based on electronics. Optical transformers not only provide high accuracy but also eliminate the saturation problem that magnetic ITs face. Unlike the magnetic instrument transformers, OITs have no iron core and have three types of output signals: low energy, high energy, and digital outputs. Furthermore, according to the manufacturers and designers, an OIT has better accuracy compared to a conventional magnetic instrument transformer and a better transient response due to the lack of an iron core that limits the bandwidths. Typically, the OITs are safer as well as lighter and smaller. On the other hand, whether OITs can be completely

replaced with magnetic ITs is still under investigation. The investigation requires a complete comparison of the two systems and field applications. In addition, power system simulations are also another method to investigate system behavior and performance as long as the proper models of the equipment exist. Specifically for the protection applications, models of the magnetic ITs exist and are well defined for simulations. However, complete models of the optical ITs are not very well presented.

1.2 Literature Review

The literature presents several developments and testing of OITs that can be used for understanding the system behaviors. Since the current and voltage transformers are the two types of instrument transformers, this literature review section presented each transformer type separately dealing with the accuracy, transient behavior, bandwidth, comparison of the systems, and flexibility of digital and analog systems.

1.2.1 Optical Current Transformer

The first studies on the optical current transformers (OCT) were published at the end of 1970s and during 1980s. Those studies mainly focused on the feasible power system applications of optical sensors. Most of the studies concentrated on the development of a Faraday effect-based low-voltage optical current sensor. In late 1980s and the early 1990s, researchers began to study the high voltage (HV) applications of optical current sensors. The transient behaviors of OCTs were investigated since it is important for high voltage applications. From the beginning of the 1990s until today, large numbers of studies have dealt with the performance improvement of OCTs that are used for power system protection. Different variations of the Faraday effect and the effect of various environmental conditions were studied. At present, several different OCTs have been developed and offered for application in power systems.

Steer, Turner, et al. described a design and test of a developed OCT and compared the OCT with a conventional CT in [2]. The Faraday effect was used for the current-sensing method. A 10 kA current was applied using 25 turns of cable around the sensing head that carried a 400 A current. A direct current test was also performed to determine the performance of the developed

OCT. A shunt was connected to the circuit, and the voltage across the shunt was compared with the output voltage of the OCT. Results showed that the OCT was linear and well below the saturation limit. The step function responses of the optical and conventional CTs were obtained. A DC pulse was applied on the OCT and magnetic CT. Results showed that magnetic CT was saturated and differentiated the pulse. There was a 1 ms delay in the current reading for the optical system because of the digital processing technique.

Sawa, Kurosawa, and other Japanese researchers [3] presented a paper that is frequently cited as a reference. Toshiba Electric Power Co. and Toshiba Corp. performed the study. A gas insulated switchgear (GIS) type OCT was developed and presented. The Faraday effect was used for sensing the primary current, and two different methods were used. The accuracy test of the OCT was performed, and it met the requirements of the Japanese JEC 1201 standard. The paper also presented temperature characteristics and transient characteristics of the CTs. The transient response of the OCT was obtained by applying 63 kA rms transient primary current. It was observed that the transient error was below the requirements and the OCT was not saturated with high current above the rated value.

Leung and others overviewed various types of optical current sensors and developed a fiber-optic current sensor in [4]. System configuration and characteristics were presented, and the developed OCT was used for an application of fault detection in a power transformer. The effect of temperature on current sensor measurement was also investigated. Results show that the sensor was temperature dependent. The total cost of the developed system was presented as $2,500 USD.

Cruden and others [5] described a Faraday effect-based measuring device, which meets the British Standard BS3938 requirements. A terbium gallium garnet (TGG) crystal was used as a current sensor. The performance of the sensor was also discussed with respect to harmonic content, vibration, and temperature effects. The linearity of the sensor was tested by comparing the applied and measured primary current. The designed optical CT was tested in a current range of 0 to 5000 A, and the spectrum analysis of the sensor was compared to the output from 0.1% accuracy class .

Cruden et al. continued to develop an OCT in [6]. The system was tested with large short circuit current. A class 0.1% 100.00/5 A CT was used to compare the OCT output. During the experiments, it was noticed that the sensor had a poor signal-to-noise ratio. An interface to an over-current protection relay was developed, and the OCT was tested with the relay. The relay tripping time was recorded, and it met with the manufacturer specifications. The OCT performance was tested for any neighboring magnetic field effect on the sensor and tested for temperature and vibration changes in the environment. According to the test results, compensation methods developed for temperature and vibration changes in the environment were effective.

Maffetone and McClelland presented a 345 kV optical current measurement system in [7]. The operation principal of the OCT was described, and the system was tested for metering and protection applications. The system was installed in a substation, and the waveform quality of the system was compared with magnetic CT output both in time and frequency domains. Test results showed that the OCT output was very noisy compared to the magnetic CT output and the designed OCT can replace the magnetic CT successfully.

Zhang and Halliday [8] studied an optical current transformer that was also based on the Faraday effect. Among the three-sensor materials, diamagnetic, paramagnetic, and ferromagnetic materials were used and tested for temperature dependence since all the sensor materials are temperature sensitive. The effect of neighboring phase magnetic field was also tested in this study. According to the results, neighboring phase magnetic field was eliminated not to affect the measurements. The linearity test was performed for 20A to 1300A currents, and the results showed that the input-output relation was not linear. The average relative error was less than 0.13% within a range of 20 A to 1300 A for the AC current. The OCT was tested with DC, and the average relative error was found to be less than 0.6%, within the range of 120 A to 300 A.

Werthen and others described the ABB Power System Company's optical current transformer in [9]. The optical current transformer was tested for DC, 10 kHz, and 16 kHz AC current. The test obtained 0.2% accuracy, which met the specifications. As in the other studies, the temperature effect on measurements was tested. Temperature tests were conducted between -60 ^{o}C to

+100 ^{o}C. Results showed a decrease in the output voltage of OCT as the temperature increased. A phase angle characteristic of the system was obtained. Results showed that there was no phase shift until the frequency reached 1 kHz.

Nie and others described in [10] an optical current transformer that is slightly different from a high voltage CT. A magnetic potentiometer that produces a signal proportional with the line current was used to sense the current, and the signal was transmitted with fiber-optic cable. The accuracy of the system was tested with a current generator from 0 to 15 kA. The error was less than 0.08% in the measurements. The temperature impact on measurements was tested for 3kA constant current, and the results show that the error was negative at lower temperatures and positive at higher temperatures.

Willsch and Bosselmann presented three magneto-optical current sensors (MOCT) that were placed inside a 120 MVA power generator in [11]. Tests were performed under the influence of high temperature, vibration, and current up to 120 kA. Test results show that the output signal versus the current characteristics of the system was linear.

Michie and others presented a harmonic analysis of current waveforms using an optical current sensor in [12]. The OCT output signal and reference voltage were analyzed by fast Fourier transform (FFT) to make the harmonic analysis. Although the rms values of the signals were different, the harmonic content was identical. The maximum difference between the signals was less than 0.25%.

Hrabliuk investigated the CT saturation and the behaviors of optical CT in the case of saturation in [13]. Due to the magnetic core, conventional current transformers have saturation, which affects the secondary side output signal that is connected to meters and relays. On the other hand, in an optical current sensor there is no saturation because it does not have an iron core. However, the distortion of signals can be a problem during the fault. The current changes rapidly, and it affects the linearity of the signal. In the designed OCT, this problem was compensated by the use of electronics. This paper discussed the characteristics of NxtPhase designed optical current sensors and presented the compensation technique for nonlinearity of the signal.

Interfacing the optical current sensors with conventional meters and relays requires a new approach. Hrabliuk studied interfacing of optical current sensors with the existing meters and relays in a substation in [14]. The optical CT output is an inherently digital signal in a NxtPhase produced OCT. This digital signal was converted to an analog voltage signal and to analog current signal. The device had three types of output: digital, low-energy-analog (LEA) (e.g., 4 V represents rated current), and high-energy-analog (HEA) (e.g., 1 A represents rated current). The low-energy analog (LEA) output is designed for either metering or relaying.

High-energy analog (HEA) output allows for use of optical sensors in substations with conventional relays and meters. A power amplifier allows the connection of an optical CT in parallel with a conventional CT. The NxtPhase optical current transducer output had an inherent noise that can affect the sensitivity of both meters and relays. These incorrect readings appeared at low current levels, 100 A. One effective method of reducing the signal-to-noise ratio was wrapping the conductor with multiple turns of fiber. This method increased the sensitivity of the sensor and reduced noise to an insignificant level.

The reliability performance of the NxtPhase developed OCT was defined by Nicholson in [15]. The importance of dependability, reliability, maintainability, and interchangeability brought attention to this study. It provided a structure for the development of a reliability program. Military standards and handbooks were used to describe the planning methods and implementation techniques. In conclusion, it was stated that reliability performance of the system must be implemented during the theoretical design.

Blake [16] studied the fiber-optic current sensor calibration technique for NxtPhase products. The aim of the calibration was to prove the accuracy of an OCT in which the optical sensor must have better than 0.2% accuracy. The OCT accuracy depended on the current level, and each output type had to be calibrated. The dynamic range for this study was ~1 amp to 3.6 kA. Generally, at low, current the accuracy decreased. Consequently, the calibration was performed in two levels: low current levels (<100 A) and high current levels (100 to 3600 A). Each output (LEA and HEA) was calibrated with these two levels by using a high precision current transformer.

Rahmatian and Chavez [17] described the NxtPhase-produced (according to the IEC 60044-7, 60044-8, IEEE C57.13, IEEE C37.92 standards) 550 kV class three-phase combined optical voltage and current transducer (NXVCT). Dielectric performance and the effect of temperature and vibration on the accuracy were tested in an HV laboratory. The device met the accuracy requirements of IEC 0.1% class voltage transformers when the temperature was in the range of –40 ^{o}C to +60 ^{o}C. The device also maintained 0.1% class accuracy when subjected to vibration.

Blake and Rose, who are also from NxtPhase Cop., tested a NxtPhase produced OCT and OVT with a Landis-Gyr class 2 MAXsys 2510 power meter in [18]. The current was varied between 0.01% to 150% of the CT rated current, and the voltage was kept constant. The thermal rating of the OCT was tested using 63 kA for a few cycles. The mechanical integrity of the OCT was tested using 171 kA peak dynamic current. The accuracy test was performed according to the method described by Blake in [16]. The results show that NxtPhase products had better accuracy than described in the standards.

Chen et al. presented in a comparative method for the development of an OCT in [19]. A permanent magnet was used as a reference source, and the sensor was designed accordingly. Performance of the new designed was tested, and results were satisfactory.

Chen et al. presented a developed OCT in [20] using a Rogowski coil to detect and measure the line current. The developed OCT was compared with magnetic CT for steady state and transient measurements. Results showed that the developed OCT could serve better than the magnetic CT for distance protection.

Rahmatian and Blake presented NxtPhase-produced, improved OCTs in [21]. A new type of the OCT that did not include an insulator chain was presented. The design included a flexible sensing head. The new product and the improved product were tested for AC and DC applications, and the results included tests for accuracy and the frequency response. Results were presented, and they were all in the range of desired values.

1.2.2 Optical Voltage Transformer

Optical voltage transformers are designed based on Pockels effect. The Pockels effect is the electrical field-produced birefringence of polarized lights in crystals that are placed in an electrical field. Different types of crystals exist and have been used for the OVT applications in the literature. The Pockels effect is similar to the Kerr effect, which is observed mainly in liquids; both are described in the literature in detail [22]. Many publications present the development of Pockels effect-based optical sensors. Most of them are focused on crystal sensor development and the material aspect of crystals, as well as the problem of the temperature sensitivity of these crystals. The optical voltage transformers are usually combined with optical current transformer applications in the literature. This literature review presents the studies on power system applications of the Pockels effect and the studies of OVTs for high voltage applications.

In 1986, Cease, Driggans and Weikel [23] developed an optical voltage sensor using the current sensing method. This current sensing method was used in their earlier studies to develop a magneto-optic current transducer (MOCT) in [24]. However, voltage measurements need sensors that are sensitive to electric fields. The MOCT was sensitive only to magnetic fields, not to electric fields. The technique used in this study was to measure the current flowing through the series-connected capacitors proportional to the voltage to be measured. The MOCT measured the current; consequently, the output of the MOCT was proportional with the voltage. Test results were compared with the magnetic VT, and 0.8% deviation was observed.

In 1995, Christensen [25] designed a prototype 132-150 kV optical voltage transformer (OVT) based on the Pockels effect, which was not include capacitor divider. A $Bi_4Ge_3O_{12}$ type crystal was placed in an electrical field that was created by two electrodes. This passive OVT did not require any power supply to operate. Temperature dependency and voltage output accuracy were tested. Results were within the specifications. The ratio of transformer could be adjusted by changing the shape of one of the electrodes, and voltage measurements were repeated for different ratios.

Kurosawa, Yoshida, Mori, Takahashi, and Saito [26] developed and tested an optical voltage transformer for DC voltage measurement. The authors had studied on development of optical voltage transformers for AC voltage measurement in gas-insulated switchgears earlier. The Pockels effect did not work properly for DC measurements, so the authors developed a method that overcomes this problem. In the later study, the developed DC voltage measurement system was described, and a series of tests that examined ratio error and temperature characteristics were presented. Field tests of the equipment were also presented. Results met with the desired values and proved that the designed transformer was suitable for control and protection of DC power systems.

Bauerschmidt and Lerch [27] proposed an optical voltage sensor based on a quartz resonator. A quartz resonator was used as a voltage/frequency *(V/f)* converter, which converted electrical voltage or electric field strength into a proportional frequency shift. A capacitive voltage divider was used to reduce the effects of voltage on the resonator since the Pockels effect-based resonator cannot withstand high voltage. The optical sensor received the frequency modulated light signal and the system generated voltage accordingly. The transformer was tested for AC and DC electrical fields, and temperature sensitivity was tested for these electrical fields. Results showed that the designed transformer was suitable for voltage measurements.

Filippov, Starodumov and others [28] proposed a novel design for an optical voltage sensor based on the $Bi_{12}TiO_{20}$ crystal. This study focused on the investigation of temperature effects on optical sensors and attempted to minimize these effects by utilizing different techniques. The sensors used in voltage transformers are temperature sensitive and most of the time an additional temperature control system is needed. In this study, a glass-back-reflecting prism was used as a phase-retarding element instead of the typical quarter-wave plate. Using this method, the designed system did not need an additional temperature control channel. Temperature sensitivity of the system was tested for different measurements results.

Santos, Taplamacioglu, and Hidaka [29] developed a new high-voltage measurement technique. The system can measure 400 kV of voltage and 0 to 30 MHz wide signal. The proto-

type of the transformer used Pockels crystals, super luminescent diode, and a special optical fiber link. AC and DC voltage tests, impulse voltage tests, and step voltage tests were performed successfully on the prototype transformer. Results matched analytically and numerically predicted values.

In 2005, Li and Cui [30] presented a new optical voltage and current sensor with an electrically switchable quarter wave-plate. A $Bi_4Ge_3O_{12}$ (BGO) crystal was used as a sensor. The paper described the principles of system operation, which included a new application of polarization multiplexing technology for the measurement of multiple variables. Sensitivity and measurement ranges were tested for both AC and DC. The presented experimental results proved the feasibility of the proposed combined optical current and voltage sensor.

Zhang and Halliday [31] described a fiber optic-based high-voltage sensor that used the Pockels effect. A capacitive voltage divider supplied the sensor head with reduced voltage. The sensor used $Bi_{12}SiO_{20}$ crystals to generate a light signal proportional with the voltage. Fiber-optic cable transmitted the sensor-generated signal to the ground level, where photodiodes converted the light signal to an electric signal. The paper described the operation in detail and presented test results proving the feasibility of the presented method.

Rahmatian, Chavez, and Jaeger [32] presented 138 kV and 345 kV optical voltage transducer (OVTs) designs and their high voltage test results. The Pockels effect was used for the voltage measurements. A quadrature method was applied to obtain voltage from electric field measurements by placing three miniature optical field sensors placed inside the column. This method defined the needed number of sensors, as well as their positions. A novel shielding technique and multi-sensor quadrature method was used to minimize the stray field-caused errors. Accuracy of the OVTs was tested according to the IEC 60044-2 (1997) and IEEE C57.13-1993 standards. The developed OVT units met the 0.2 class (IEC) and the 0.3 class (IEEE) revenue metering requirements. It was known that OVTs had 40 kHz bandwidth; however, due to the difficulties of generating high-voltage high-frequency signals, devices were tested for 3 kHz. A standard capacitive divider and a step-up power transformer were used as harmonic sources to test the bandwidth. In

order to test the accuracy of transformers under severe contamination, fog pollution tests were conducted. The pollution test proved that pollution does not affect the accuracy. Insulation performances of the OVTs were tested and a 650 kV peak lightning impulse test as well as 750 kV peak chopped impulse test were applied to the 138 kV class OVTs. A 345 kV OVT was also tested with a switching impulse under wet conditions. Partial discharge tests were performed as well on both OVTs. All units performed satisfactorily under tests.

Rahmatian, Chavez, and Jaeger [33] presented an early design of a 230 kV optical voltage transducer using a similar method that was described in [32]. In addition to the study in [32], the quadrature method was tested for different conditions. It was found that three sensors were able to measure accurately the voltage of 230 kV. N_2 gas was used for insulation, and the OVT's weight was around 220 kg. The transformer ratio was 70,000:1 V where the 140 kV corresponds to 2 V. Lightning impulse testing, wet testing, power-frequency resistance testing, partial discharge testing, chopped impulse testing, mechanical testing, and linearity testing were conducted for three different transformers. The accuracy of the transformers met with the standards, and each transformer had a 0.95-degree phase delay due to signal processing. These three OVTs were installed as a three-phase voltage measurement system at BC Hydro's Ingledow substation in Surrey, BC, Canada.

The accuracy of optical voltage transducers under pollution and other field distributions was tested by Rahmatian, Chavez, and Jaeger in [34]. The operation principle of the transformer was described in [32]. It was known that the outside disturbances could affect the electric field distribution inside the OVT. Resistive shielding was used in OVTs in order to avoid any impact on accuracy. In this study, a series of tests were conducted to test the performance of the shielding. Two OVTs were placed very close to each other. The sensing head of one of the OVTs was grounded, and the other OVT was energized with 50 kV. This situation represented the worst-case scenario in a substation. The output voltage of the grounded transformer was zero. It was observed that the neighboring 50 kV-produced electric field did not affect the grounded transformer output

and accuracy. The bandwidth of the NXVT optical voltage transformer was about 40 kHz where the conventional voltage transformer has a bandwidth of 1.5 kHz.

Rahmatian, Romalo, and others [35] also studied the effect of electrical field distribution on an older version of the OVT. A grounded metallic plane was used in order to simulate the neighboring electric fields and to distribute the electric field close to the OVT. The OVT was energized to 170 kV, which was 120% of rated voltage, and the introduced error was less than 1% in this extreme case. The field distribution was also affected by rain and water flow. Wet-without-water flow and wet-with-water flow conditions were tested, and the introduced error was again less than 1% on this early prototype OVT.

Rahmatian, Chavez, Jaeger [36] tested the 138 kV OVT under severe dynamic field disturbances, including salt-clay pollution. The dielectric performance of voltage sensors was also verified by high-voltage dielectric tests. The tests included a lightning impulse test, chopped impulse tests, and a partial discharge test. The voltage sensors were placed in a hollow-core composite insulator filled with low-pressure dry nitrogen. The effect of melting ice was investigated in this paper. The results were similar to those in the previous studies. The linearity and accuracy of the OVT was not affected by pollution and melting ice.

Bohnert, Gabus, and Brändle [37] of ABB in Switzerland developed optical current and voltage sensors for high-voltage substations and presented them in this study. The electro-optic voltage transducer (EOVT) was based on the Pockels effect. An additional temperature sensor was used to compensate for the temperature dependence of the Pockels effect. The insulator supporting the EOVT was filled with a soft polyurethane resin instead of the usual SF6 gas. Different applications of the equipment were described and tested according to the standards. Results proved that the designed transformers are suitable for high voltage applications.

1.2.3 Literature Review Summary

The literature on both optical voltage and current transformers presents many studies. All of the works aim to prove that the developed ITs have higher performance, are suitable for power system applications, and can replace the conventional ITs. Different comparison methods are used

to show the compatibility of optical ITs with conventional ITs. Furthermore, few ITs have been installed in addition to conventional ITs at substations, which would allow a comparison of the two devices' performances in practical power system conditions. Results are encouraging but have been limited. The literature reports only a few comprehensive laboratory studies on the comparison of these ITs. Specifically, there is no study to analyze the digital output characteristics of ITs. In addition, the literature shows that models of magnetic instrument transformers have existed for many years. However, models for optical instrument transformers are not very well presented. A few modeling studies have been performed only on optical elements of the current transformers in order to improve the accuracy, but a complete model that considers the optics and the electronics together has not been presented. Hence, there are no simulation results and methods presented due to the lack of complete model existence. In addition, models for optical voltage transformer are not found in the literature.

1.3 Objectives and Scope of This Research

In this research, the characteristics of optical voltage and current transformers are investigated, and the steady state and transient performances of magnetic and optical current and voltage transformers are compared. All tests are performed in ASU's high voltage laboratory. Actual field conditions (load current and fault current, high voltage and sag voltages) are reproduced, and responses of magnetic and optical transformers are compared. Transient performance of the OCT is measured using a step-function, and the transient performance of OVT is measured using an impulse function. The impact of increased temperature on the OCT measurements is determined by increasing the sensor head temperature. Amplitude-frequency and phase-frequency characteristics of the optical voltage and current transformers are obtained.

Based on the characteristics, three models are developed for analog outputs: analog, digital, and complete models. In the analog model, transfer functions (s-domain) are developed and their representations with circuit elements are presented. Digital representation of the analog outputs are presented by transforming the s-domain transfer functions to z-domain transfer function. Realizations of the digital models are presented with direct form block diagrams. The complete

model consists of two parts: optics, and electronics. Optical elements are modeled with the Jones calculus method. This model provides the voltage and current information for the electronics of the transformers. The previously developed transfer functions are used as the electronics model. These transfer functions process the signal information coming from the optical model and generate analog outputs. All the developed models are simulated and tested. Digital output signals of OCT are captured from the process bus by a computer, and both steady state performance and frequency response are evaluated.

1.4 Dissertation Overview

The outline of the thesis is as follows:

Chapter 1 presents the statement of the problem and motivation, literature review about optical instrument transformers, and the objective of the report.

Chapter 2 concentrates on the optical current transformer characteristics and presents an experimental comparison of magnetic and optical current transformers.

Chapter 3 concentrates on the optical voltage transformer characteristics and presents an experimental comparison of magnetic and optical voltage transformers.

Chapter 4 presents the experiments performed to determine the amplitude- frequency and phase- frequency characteristics of optical transformers. Three different models are developed for analog outputs: analog, digital, and complete models.

Chapter 5 presents the characteristics of digital output of optical current transformer. Experiments performed to determine the amplitude-frequency characteristics are presented.

Chapter 6 concludes the report and suggests future work.

CHAPTER 2

OPTICAL CURRENT TRANSFORMER CHARACTERISTICS AND COMPARISON WITH MAGNETIC CT

2.1 Introduction

Before answering the question "Can an OCT substitute for a magnetic CT?" the operation principle and all characteristics of the OCT needs to be well understood. Indeed, any models that are developed for OCT have to be based on the experiment results and characteristics of the OCT. The experimental work requires the building of a high-current generator as well as understanding of the operation of the NxtPhase OCT. In this chapter, a detailed analysis of OCT for measurement and protection applications is investigated, the operation principle of the OCT is presented, experiments are performed, and test results are presented. Tests are conducted for magnetic CT, and the comparisons of the test results are presented. NxtPhase supplied an OCT and Salt River Project donated a 69 kV magnetic CT to ASU's high voltage laboratory for this study.

2.2 NxtPhase Optical Current Transformer Structure

NxtPhase is one of the companies that manufacture optical current transformers in the market. The company provided a CT marked NXCT to ASU for testing. The NXCT uses the Faraday effect but in a different structural design. The magnetic field due to the current carrying conductor changes the velocities of circularly polarized light waves that travel around the conductor. The operation of the NxtPhase OCT is described in the manufacture's data sheet and in [38] and is reproduced here.

The optical circuit of the NXCT is shown in Fig. 2.1. Light from a light source, mainly light emitting diode (LED), enters into an optical fiber polarizer. The light is polarized and then splits into two orthogonally polarized light waves in the polarizer and pass through a modulator. Travel finalizes by a polarization maintaining (PM) fiber travelling through the sensing head. A fiber optic quarter-wave plate converts the two linear orthogonal waves into circular waves, right and left-hand polarized light waves. These circular waves travel through fiber optic cable and wind around the conductor.

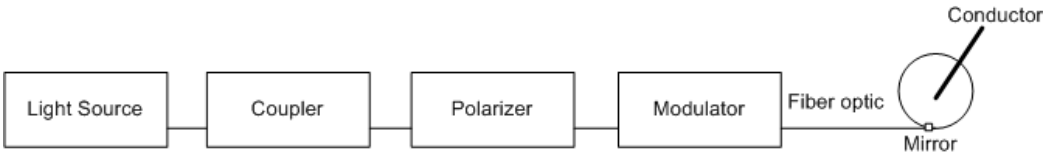

Fig. 2.1. NXCT optical CT structure [38]

The two waves travel at different speeds through the sensing fiber. The difference in speeds is proportional to the strength of the magnetic field aligned with the sensing fiber. After completing their journey in the sensing region, the two waves reflect off a mirror. The reflection causes a reversal of circular polarization of the two waves, and the two waves then travel in the opposite direction with respect to the magnetic field. While traveling in the opposite direction, the two waves continue to maintain their velocity difference for the return trip through the sensing fiber.

During their return journey, once the light has retraced its way through the sensing region, the two waves again encounter the quarter-wave plate that converts them back to their linear polarization states. Circular polarized lights become linearly polarized, but x-polarization returns in the y-polarization state and vice-versa. As shown in Fig. 2.1, the path followed by the two waves during their entire journey can be pictorially depicted.

The magnetic field on the sensing head is the only physical quantity that affects the difference between the two light waves. This process is called as Faraday effect, and the difference is proportional with the amount of current passing though the conductor.

Fig. 2.2 shows the NXCT physical layout. NXCT is divided into four separable elements: the opto-electronics chassis, the fiber optic cabling, the sensor head, and standoff. The opto-electronics chassis incorporates all the electronics as well as the light source and optical components up through the modulator. This chassis is located in the control room.

One interesting feature of the fiber current sensor is that the dynamic range of the sensor can be scaled to fit almost any application simply by changing the number of fiber turns on the sensor head. The first prototypes use four turns of sensing fiber, which allows the sensor to relia-

bly detect currents over range of 100 mA to 100 kA. This range covers the majority of requirements of high voltage metering and relaying applications.

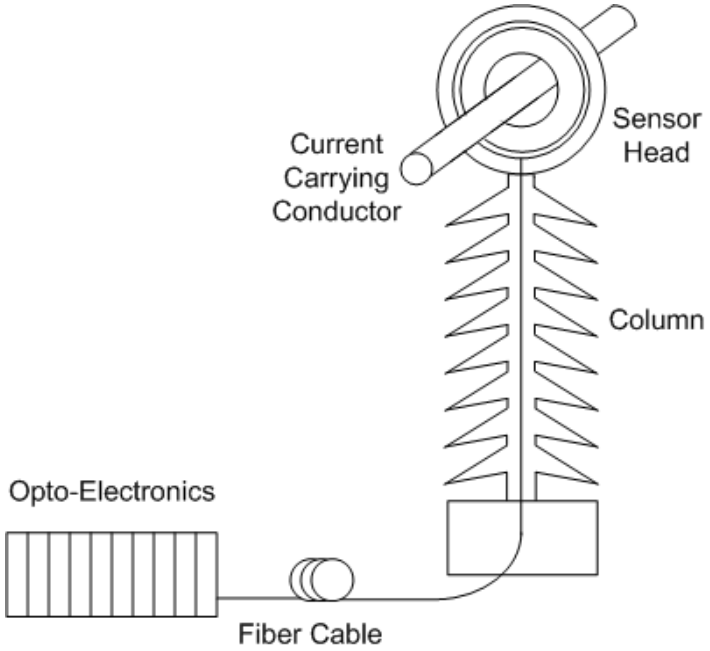

Fig. 2.2. NXCT optical current transformer [38]

Fig. 2.3 shows the block diagram of OCT. There are three outputs based on IEC 60044-8 standard [39]. Both analog (LEA protection output) and digital outputs are tested in this study. The outputs are:

1. Digital
2. Low energy analog (LEA) rated at 4 V for metering and 200 mV for protection. In this case, the ratio was programmed to be 1 V output at 1000 A primary current. The accuracy in protection (relaying) mode is 0.3% and 0.15% in metering mode.
3. High energy analog (HEA) (5 A at 3000 A rated current).

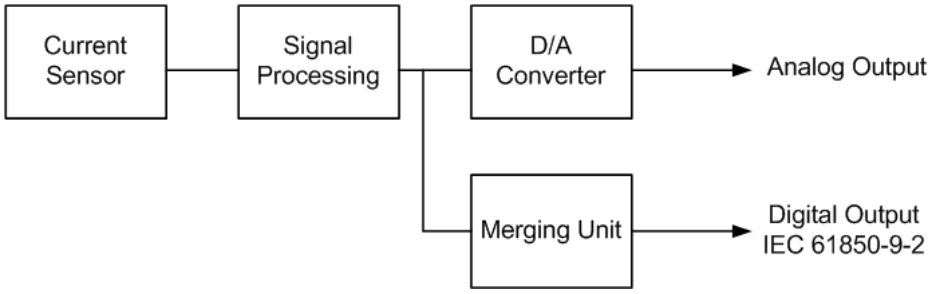

Fig. 2.3. OCT block diagram

2.3 Experimental Test Setup

The performance of optical and magnetic CTs is measured and compared. The specification of the tested conventional magnetic CT is:

- Voltage 69 kV, BIL 350 kV
- Rated frequency: 60 Hz
- Weight: 625 lbs
- Current 800 A/ 400 A/5 A
- ASA Accuracy classification 0.3 B-0.1, B-0.2, B-0.5, B-2 at 60 Cycles (B- 0.1 class 2.5 VA, PF= 0.9, Z=0.1 Ω)
- 5 A High energy analog output

The optical CT specification is:

- Voltage: 145 kV, BIL: 650 kV
- Rated frequency: 60 Hz
- Weight: 152 lbs
- Rated maximum thermal current: 3000 A
- Rated short-circuit current : 63 kA
- 1C Accuracy (relaying): n/a
- 2C Accuracy (metering): 0.15
- Rated delay time: 40 μs

It can be seen that the OCT, even though it is of a higher voltage class, is significantly lighter than the conventional magnetic CT.

In this study, the LEA output was used. An OCT of this type can be configured for metering or for protection application. The physical design of the OCT is identical for both applications, but certain settings are optimized for each application. When configured for metering, the rated secondary output is typically 4 V with two times over-current measurement capability. For protection application, the rated output is typically 200 mV, allowing for 40 times fully-offset fault over-current (transient) measurement. Naturally, when using the protection rating, the signal-to-noise ratio (SNR) on the output signal is lower at low currents (due to a fixed electronic noise) as compared to when the 4 V rated metering output is used.

When intended for metering applications with rated currents below 4000 A, typical OCTs of this type are built with 20 fiber turns. More fiber turns will result in higher SNR, which is of interest when metering low currents. For protection applications, on the other hand, OCTs of this type are typically built with 2 (or 3) fiber turns to allow for easy reproduction of current waveforms with peaks as high as 200 kA. Naturally, at an optical level, a 20-fiber-turn OCT is 10 times more sensitive than a 2-fiber-turn OCT. In this study, the OCT is specifically configured for ease of testing. Instead of using a 2000 A rated 2-fiber-turn OCT, a 200 A rated 20-fiber OCT is used. In this way, all the tests could be performed at much lower currents, which were easily produced in a laboratory. The ratio of this 20-turn metering CT (3000 A: 4 V) is changed via software to 200 A: 200 mV. Its performance would be equivalent to a typical 2-turn 2000 A: 200 mV OCT while operating at one tenth the primary current.

The optical CT is set in a protection mode with a ratio of 200 A: 200 mV (i.e., 1 V secondary = 1000 A primary), and the Low energy analog (LEA) output is connected to the second input of the digital oscilloscope.

The current generator that simulates the high current consisted of three ring types of current transformers. The 5 A secondary coils of these three ring type current transformers are connected in parallel and supplied with a regulating transformer. This regulating transformer controls the magnitude of the generated current. A heavy, insulated conductor forms a short-circuited loop

as the primary conductor that carries the current thread through both current transformers. Fig. 2.4 shows the experimental setup.

A low voltage circuit breaker protects the system from overload, and an electronic switch is used for current initiation between 0 and 180 degrees on the source voltage wave. The maximum current of the system without the load is 1200 A. All tests are performed at room temperature. Fig. 2.5 shows the laboratory environment and the test setup.

The tested magnetic CT is set to 800 A/ 5 A and is loaded with a 0.1-ohm high precision resistor. The 0.1-ohm burden provides metering accuracy. The voltage across this resistor is proportional with the current (1 V=1600 A), and it is measured by a digital oscilloscope. The optical CT is set in protection mode, and the low energy analog (LEA) output (1 V = 1000 A) is connected to the second input of the digital oscilloscope.

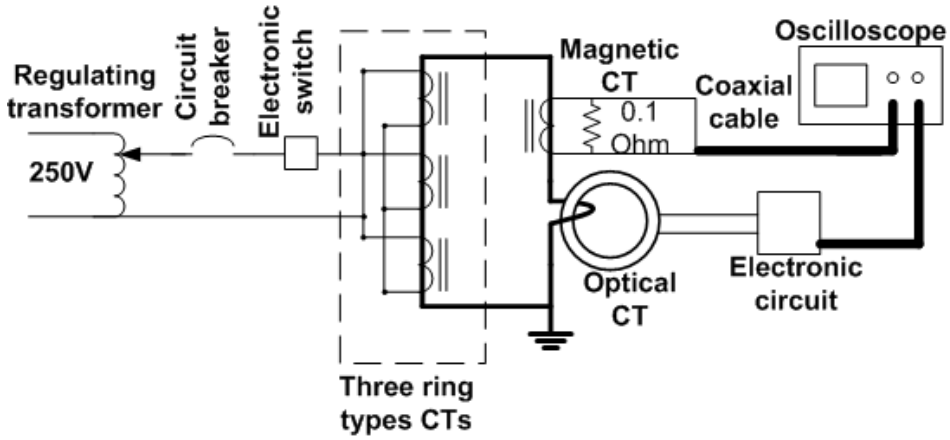

Fig. 2.4. Experimental test setup

The voltage magnitude measurement accuracy of the oscilloscope is ± 2%. However, since only the difference between the two channels is considered in this study, the digital oscilloscope is calibrated by supplying the two input channels with the same signal, and the difference of the two inputs is measured. The amplification of the channels is adjusted so that the difference between the two channel readings is less than 0.5%. This test is repeated for different settings of the input amplifier. The described calibration is repeatedly performed during the tests to assure high accuracy.

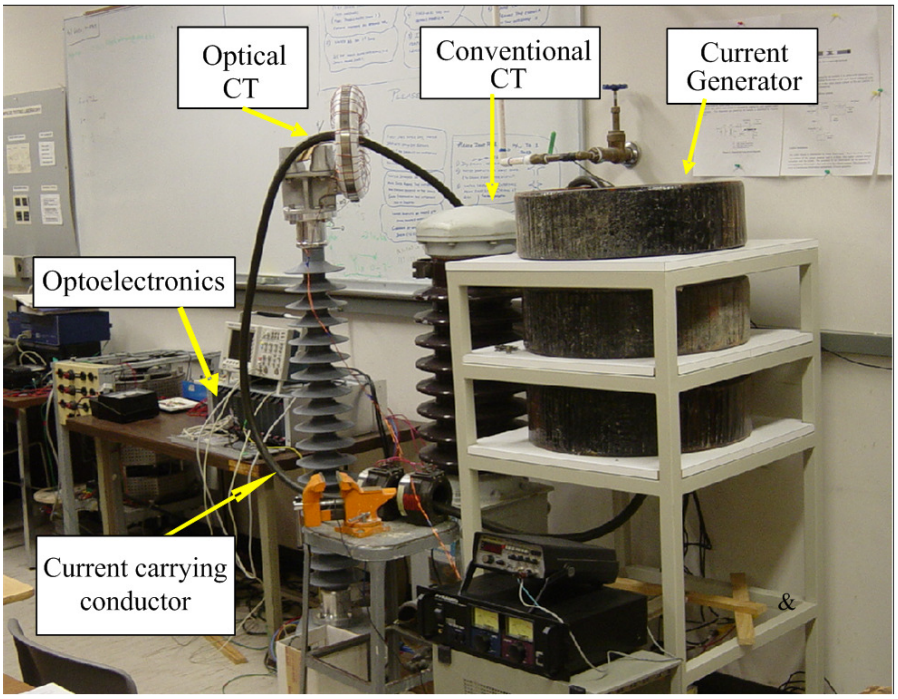

Fig. 2.5. Experimental test setup in laboratory environment

2.3.1 Steady State Performance

The purpose of this test series is to compare the two CT operations, rather than verifying their accuracy, and to show the linearity of CTs as opposed to absolute calibration. The manufacturers use standardized methods [39], [40] to verify the rating and accuracy of both CTs.

For the steady state response performance tests, both the circuit breaker and the electronic switch are closed, and the current level is adjusted between 248 A-762 A in eight steps using the regulating transformer. Although the maximum generated current in the setup is 1200 A, the impedance of the magnetic current transformer limited the generated current to 762 A. The waveforms begin with a transient mode and gradually reach their steady state value. The tests are repeated by both increasing and decreasing the current level. At each current level, the wave shapes and rms values are recorded.

The recorded wave shapes of the transformers are compared. It is noticed that the OCT output voltage has white noise. Fig. 2.6 shows the recorded OCT output signal when measuring 476 A. The measured rms value of the noise is 26 A rms (6.0% of signal). The amplitude of the

noise is independent from the load current, and it is easily observable at low primary current levels. The white noise of the conventional CT output is 0.48%, which is less than the white noise measured on the OCT's output. The majority of this noise may be attributed to the oscilloscope and the waveform capture circuit used in conjunction with the OCT electronics. The OCT LEA output consists of two floating conductors with common-mode electronic noise on them. When one side is ground via oscilloscope, the common-mode noise appears as additional noise on the signal observed on the other conductor.

All optical and/or electronic systems have some kind of inherent noise, and the amount of noise depends on the sensor design. The measured white noise average value is zero with Gaussian distribution. Filtering can remove this white noise [16]. Consequently, it does not affect metering accuracy or protection relay operation.

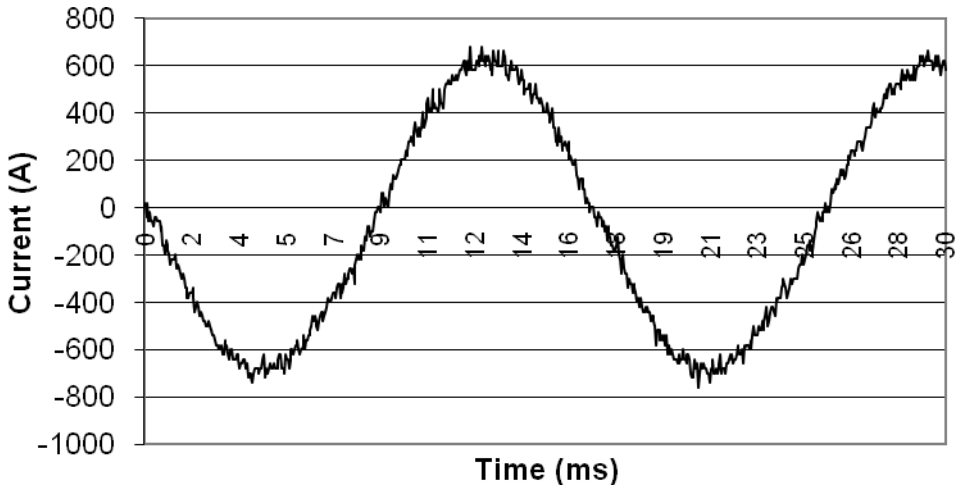

Fig. 2.6. OCT output signal

The comparison of the CT measurements in steady state is performed by using the measuring technique recommended in [16]. The test includes a high precision magnetic CT in which the output is compared with the tested CT output. The magnetic CT and optical CT are tested separately and the differences are compared.

The optical CT output is compared with a 1000:1 A high precision calibration CT output, and Fig. 2.7 shows the test setup. The outputs of the CTs are connected to a differential amplifier in order to make comparison and to find the difference between them. The precision CT output is

connected to a 1-ohm calibrated resistor, and the voltage across this resistor is used as input 1 for the differential amplifier. In this case, 1 V across the 1-ohm resistor corresponded to 1000 A primary current.

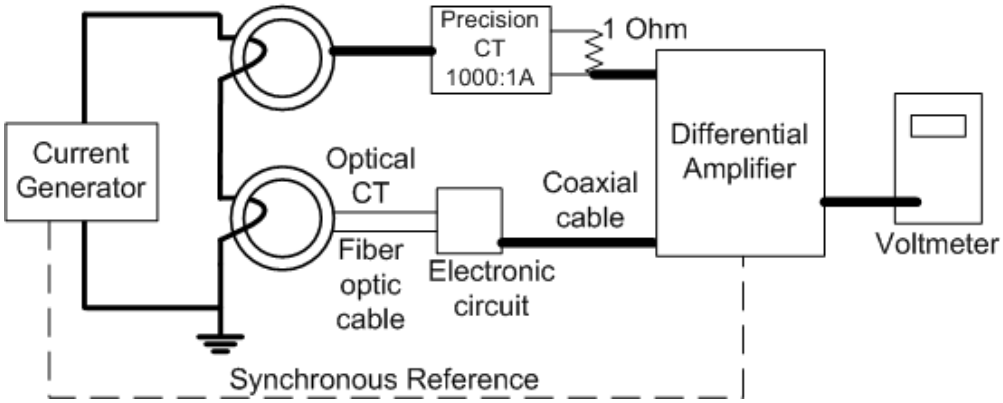

Fig. 2.7. OCT measurement with the differential amplifier method

The optical CT LEA output is used as input 2 for the differential amplifier. The OCT output of 1 V corresponded to 1000 A primary current. Hereby, the outputs of the two CTs become equal at 1 V per 1000 A. The differential amplifier takes these voltages and generates a voltage that represents the difference. This voltage difference is read with a true rms voltmeter.

Table 2-1 shows the test results for the experiment. The applied current is changed from 248 A to 762 A. Eight different current values are tested and the corresponding voltmeter readings are recorded. Differences are presented in amperes and percentages. The test results show that the differences between the precision CT and optical CT are less than 0.3% in all cases.

Table 2-1
OCT linearity test results

Applied Current (A)	*Difference (A)*	*Difference (%)*
248	0.4	0.16
313	0.7	0.22
390	0.8	0.20
466	0.8	0.17
543	0.6	0.11
619	0.6	0.09
688	0.4	0.05
762	0.2	0.02

The magnetic CT in 800/5 A mode is compared with a 1000:1 A high precision calibration CT as well. Fig. 2.8 shows the test setup. The previous test setup is modified so that it does not include the differential amplifier since the outputs of the precision CT and magnetic CT are not in the same scale.

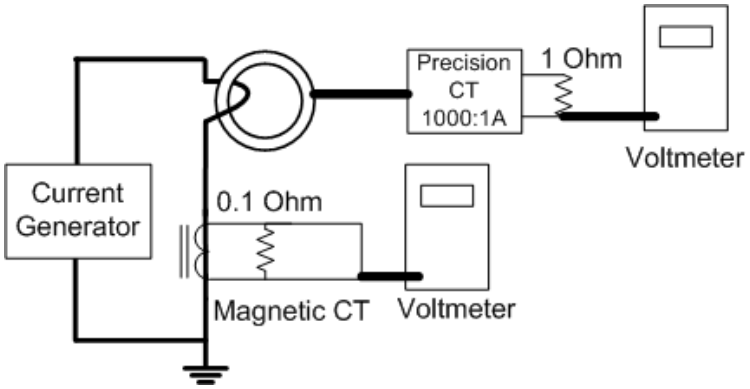

Fig. 2.8. Magnetic CT measurement with differential amplifier method

A 0.1-ohm calibrated resistor is connected to the secondary side of the magnetic CT, and the voltage across this resistor is connected to a voltmeter for the current readings. This voltage represents the secondary current of CT, and it is converted to the primary current using the turn ratio of 800 A/ 5 A. In this way, 1 V corresponds to 1600 A primary current.

The 1-ohm resistor connected to the output of precision CT is still in the circuit but connected to a voltmeter rather than differential amplifier. The 1 V still represents 1000 A primary current. The two outputs of the CTs are connected to two voltmeters, and the applied current is changed from 248 to 762 A. Eight different current values are tested, and the corresponding voltmeter readings are recorded.

Table 2-2 shows the test results and the voltmeter readings. The voltmeter readings are converted to primary current and presented with the differences. The results show that the differences between the precision CT and magnetic CT are higher than 0.3% at some of the primary current values, higher than the expected value. The higher errors are possibly related to the test setup; nevertheless, since investigating the characteristics (including the accuracy) of this particular conventional CT by itself is not the purpose of the study, this issue is not investigated any fur-

ther. In addition, the differences of each CT with the precision CT are combined and presented as positive in the last column of Table 2-2.

Table 2-2
Magnetic CT and OCT comparison test results

Difference of OCT and Precision CT (A)	*Difference of Mag. CT and Precision CT (A)*	*Difference of Mag. CT and Optical CT (A)*	*Difference of Mag. CT and Optical CT (%)*	*OCT vs. Mag. CT Difference (%)**
0.4	0.66	0.26	0.26	0.10
0.7	1.40	0.70	0.44	0.22
0.8	2.40	3.20	0.61	0.82
0.8	0.70	0.10	0.15	0.02
0.6	0.70	1.30	0.12	0.23
0.6	0.00	0.60	0	0.09
0.4	4.50	4.90	0.65	0.71
0.2	4.00	4.20	0.52	0.55

* The combination of the errors from two separate tests

The magnetic CT is switched to 400 A/ 5 A mode, and the test is repeated. The objective of this test is to investigate the CT linearity and the effect of saturation on both CTs. A hand-held clamp-on current transformer measured the primary current. Test results show that magnetic CT started to saturate after 400 A (as expected).

The magnetic CT is removed from the circuit in order to increase the generated current to be able to test the saturation of the optical CT. The heavy, insulated conductor that carried the primary current is threaded 5 turns through the OCT sensor head. This is equivalent to five times the increase in the primary current. The current is gradually increased to a maximum value of 4130 A, which is more than 20 times the rated current of the OCT. Results show that the OCT output is linear and no saturation effect is observed. The OCT output sine wave is not distorted. Fig. 2.9 shows the outputs of the two current transformers as functions of the primary current in per unit (pu) scales.

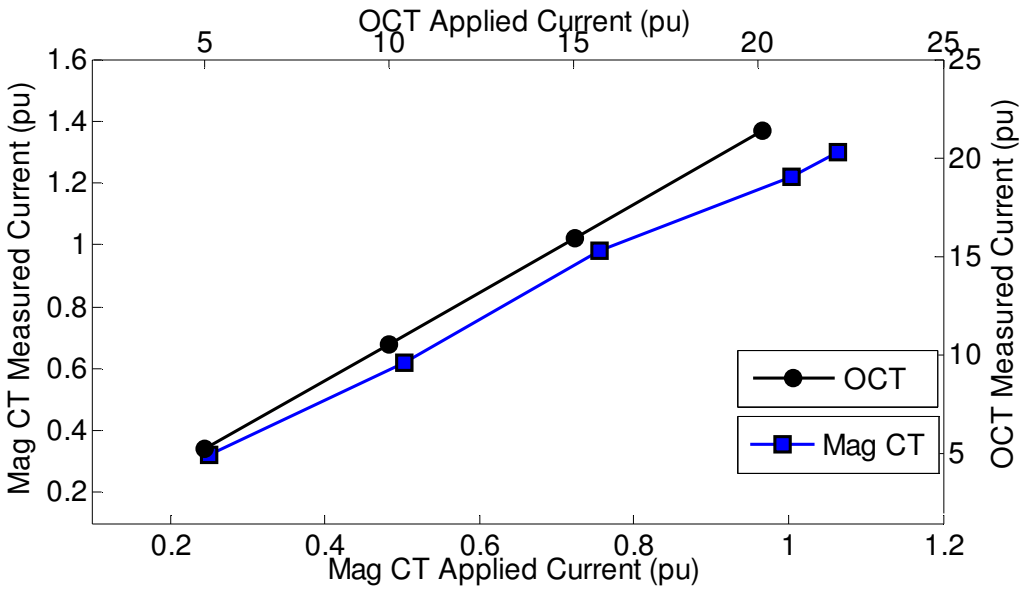

Fig. 2.9. Saturation effect (1 pu = 400 A for the conventional CT, and 1 pu = 200 A for the OCT)

The Magnetic CT is switched to the 800 A/5 A mode, and 200 A maximum primary current is applied to both CTs. The current sine waves generated by the magnetic and optical CTs recorded in a steady state condition, and the point-by-point differences of the two sine waves are calculated by subtracting one measurement from the other. A digital oscilloscope noise filter is used during this measurement to reduce the inherent output noise of the signals. Fig. 2.10 shows the recorded one cycle current sine waves and the current level difference for this cycle. The figure shows that the current difference in this cycle is 5.3 A rms. A detailed investigation of this result shows that this difference is mostly due to the phase difference between the current transformers' output signals. The OCT output signal has a 40 μs rated delay, which is less than one degree (0.86 degrees) of equivalent phase offset. This rated time delay is due to the transit time of the light and the digital signal processing. These results are within specifications of devices under the test. For metering applications where a one degree phase offset is undesirable, this rated phase offset is reduced to zero for the power frequency signal (50 Hz or 60 Hz) using digital phase advancement algorithms in the OCT electronics.

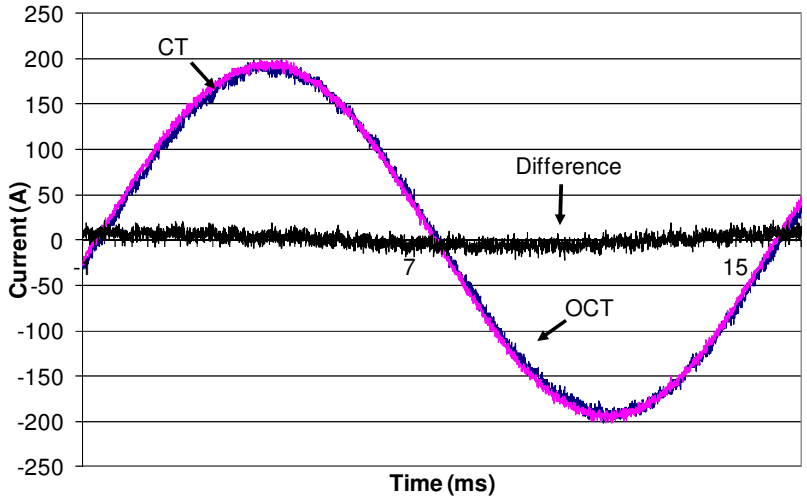

Fig. 2.10. Sine wave comparison of optical CT and magnetic CT

2.3.2 Transient Performance

In this experiment, the transient performances of both current transformers are investigated by applying a primary current that is over the rated current of each current transformer. The primary current is changed from zero to the maximum applied primary current level. The test is performed separately for both transformers because the magnetic CT limited the maximum value of the primary current. The magnetic CT is switched to the 400 A/5 A mode, and the regulating transformer output voltage is adjusted to generate 425 A rms or 656 A peak primary current. The closing of the electronic switch initiates the transient current.

The DC offset component and the peak value of the current are depend on the switching time. The available test setup is not capable of producing a significant DC offset; nevertheless, the switching time is selected experimentally to produce maximum offset. The transient current attenuated very rapidly. The current is reduced to the steady state value after a few cycles.

Fig. 2.11 shows the magnetic CT transient response. The magnetic CT is set to the 400 A/5 A mode, and the regulating transformer output voltage is adjusted to generate 425 A rms or 656 A peak primary current. Results show that the transient current reached the steady state value after three cycles. No distortion can be observed on the sine wave as the current is only slightly above the rated value. Since the magnetic CT is not the main target of testing, no extra effort is

made to produce currents higher than those necessary to properly test its transient performance at 20 times the rated current.

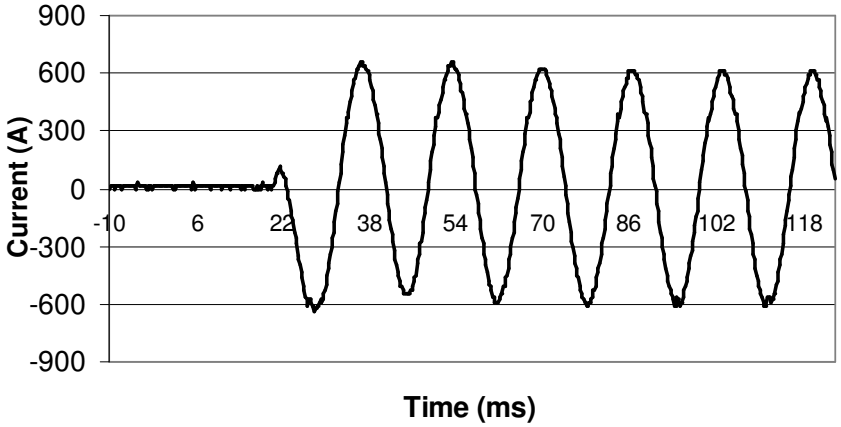

Fig. 2.11. Magnetic CT transient response

The magnetic CT is removed from the circuit in order to increase the generated current for testing the transient response of the optical CT. The heavy, insulated conductor that carried the primary current is threaded 5 turns through the OCT sensor head as it is done for the saturation test. A maximum 4130 A rms or 5440 A peak current, which is 1.376 times the rated current, is applied. Fig. 2.12 shows the optical CT transient response. Results show that the transient current reached the steady state value after three cycles. The non-distorted signal sine wave shows that 20 times rated current does not saturate the OCT.

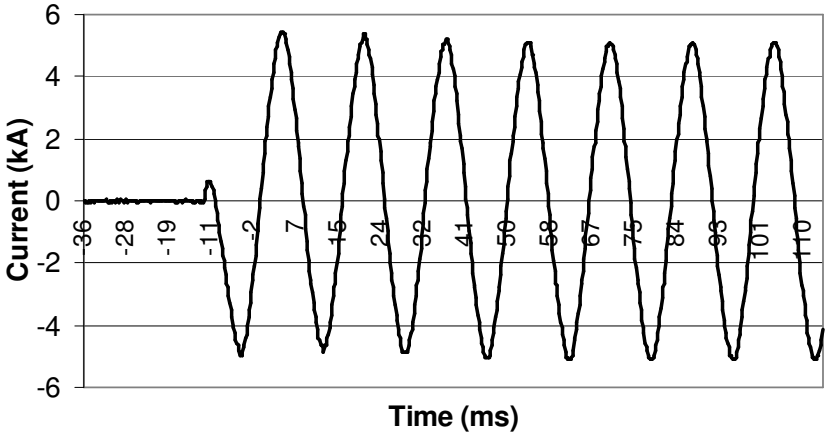

Fig. 2.12. Optical CT transient response

2.3.3 Step Response

In order to test the step response of the systems, a DC bias circuit is built. The circuit contains a thyristor switch connected to a 12 V battery and 0.1 ohm shunt. The DC current in the circuit is measured and recorded by using a 0.1-ohm shunt resistance. This circuit generates a 2.5 A current pulse. Only the step response of the optical CT is investigated. The magnetic CT is not tested because the literature indicates that even a small DC current produces saturation. Therefore, the magnetic CT is removed from the circuit. Fig. 2.13 shows the test setup. In order to increase the current's effect, 25 turns of conductor is threaded through the OCT sensor head. The equivalent OCT current is 62.5 A. This current value is low compared to a rated current of 3 kA; however, the test aims to compare the input step function and the output of OCT. The response of the OCT is analyzed. The test is repeated 5 times for both polarities.

Fig. 2.14 shows one applied impulse signal and the OCT response. Results show that the OCT delays the current impulse by 40 μs and increases the rise time of the pulse from 33 μs to 160 μs. The rise time here is defined as the time required for the pulse to increase from 10% to 90% of peak value. Results also showed that the OCT has the capability of measuring DC current without any saturation, unlike the magnetic CTs.

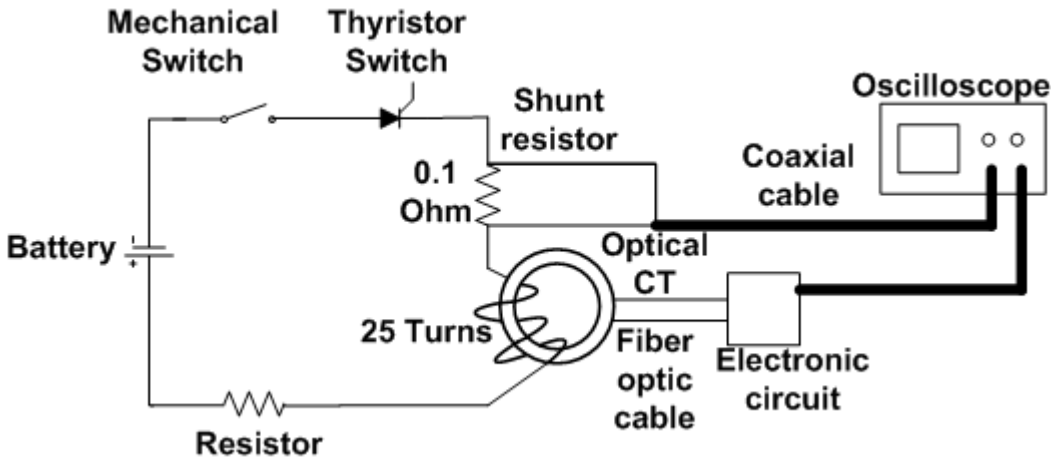

Fig. 2.13. Step response test setup

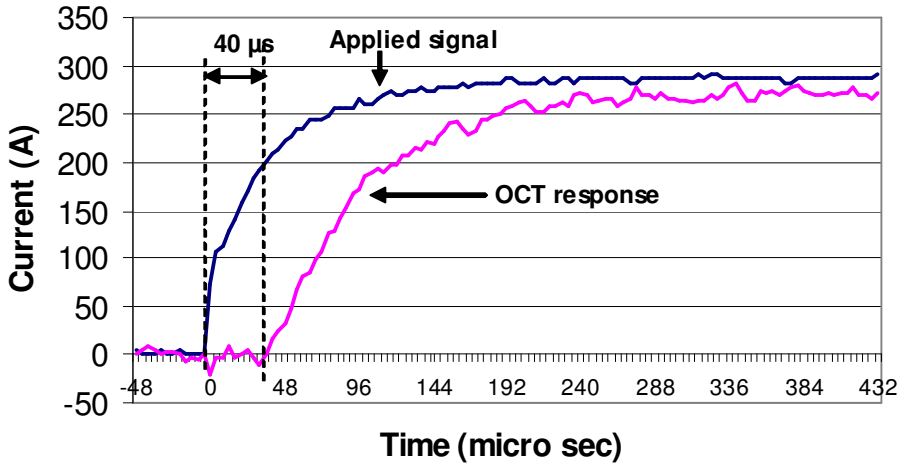

Fig. 2.14. Optical CT step response test result

2.3.4 Temperature Performance of Optical CT

The literature survey shows that the Faraday effect is temperature sensitive. Accordingly, the manufacturers of OCTs compensate for the temperature effect either optically or by using an electronic circuit (using an external temperature sensor). The OCT sensor head is heated with an electric heater in the experiment. The temperature is recorded using a thermocouple. The system is loaded by 392 A. The load current is maintained at a constant level. The temperature of the OCT sensor head is increased, and the output voltage of the OCT and the unheated magnetic CT are recorded. Table 2-3 shows the results. The result shows that temperature does not affect the OCT output to 47 ^{0}C, which proves that the manufacturer had applied an effective temperature compensation technique.

Table 2-3
Temperature effect test results

Temperature (^{o}C)	*OCT (A)*	*Mag. CT (A)*
23.5	392	392
27.5	392	392
30.0	391	391
39.8	393	393
43.5	393	393
47.3	390	390

2.4 Comparison of Magnetic and Optical CT Based on Field Recorded Data

One of the utility companies in the country has installed both magnetic and optical CTs for protection at one of its substations. Optical CT low-energy-analog output and magnetic CT 5A output are recorded by an event recorder and by the digital protection relays when a fault occurs on the adjacent line. Fig. 2.15 shows an event recording. Both CT recorded waveforms are converted to primary current and plotted together. The difference of the waveforms, which is around 80 A, is also plotted in the same figure. It can be seen that the difference is almost always dominated by a constant amount of noise and the transient fault does not affect the measurements. The maximum instantaneous difference seen in Fig. 2.15 is about 80 A peak (less than 3% of the 3000 A rated current) and is due to the noise in signals and the data acquisition system quantization noise. As expected, such a low level of noise has no adverse impact on the performance of the protection systems.

Among many recordings from the field records, 12 events, such as one phase fault and ground fault, are selected, and analyzed. Protection equipment readings, signals, and the CT readings are compared. The comparisons show that both CTs reproduced the primary current signal successfully and the protection system operated successfully with both CTs.

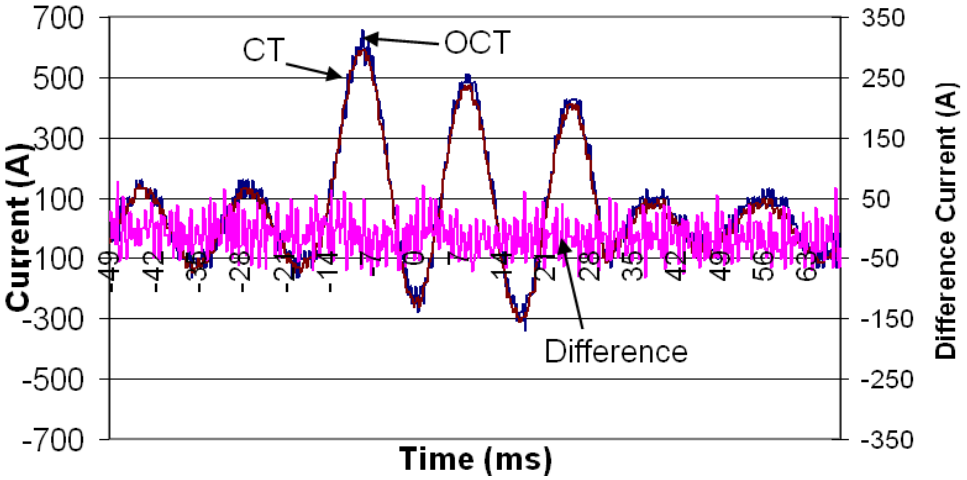

Fig. 2.15. Field recorded data

2.5 Conclusion

This chapter compared the performance of an optical current transformer with a conventional magnetic current transformer based on experimental work. The results confirmed that the OCTs are suitable for power system protection and can replace the magnetic CTs. The details are:

1. The optical CT analog output has significantly higher bandwidths (~20 kHz) than the magnetic CT does.
2. The OCT reproduced the simulated short circuit current correctly, and the DC offset current does not saturate the OCT.
3. The OCT analog output has significant white noise, but the white noise does not affect accuracy or protection performance.
4. The overheating up to 50 ^{0}C does not affect the performance of the OCT.
5. The OCT output signal has a 40 μs delay, corresponding to 0.86 degrees, that meets the manufacturer's data.

CHAPTER 3

OPTICAL VOLTAGE TRANSFORMER CHARACTERISTICS AND COMPARISON WITH MAGNETIC VT

3.1 Introduction

In this chapter, a detailed analysis of the optical voltage transformer (OVT) for measurement and protection applications is presented. The operation principle of the OVT is investigated. The steady state and transient performance of the OVT and magnetic VT are tested with a series of experiments. Comparisons of the test results are presented. NxtPhase supplied an optical VT and Salt River Project donated a 69 kV magnetic VT to ASU's high voltage laboratory for this study. High voltage signals generated with laboratory facilities are used to conduct the experiments.

3.2 NxtPhase Optical Voltage Transformer Structure

Similar to the OCT, NxtPhase also manufactures OVT in their facilities. NxtPhase provided ASU with a combined optical voltage and current transformer (NXVCT) to conduct the experiments. Only the voltage transformer part of NXVCT is used for the voltage transformer tests. NXVT uses a fiber optic voltage sensor based on the principle that the electric field changes the circular polarization to an elliptical polarization. The operation of the NXVT is described in the manufacturer's data sheet, referenced in a detailed way, and reproduced here.

NXVT sensors are placed in a post-type high voltage composite insulator. The post insulator is built with a fiberglass tube, which is covered on the outside by rubber sheds. Inside the insulator tube is a smaller tube, which is a hollow cylindrical resistor used for shielding. Three Pockels cell-based sensors are placed in the inner tube. Dry nitrogen is used for insulation. Two electrodes are placed at the ends of this structure: a high voltage electrode at the top (connected to the line) and a ground electrode at the bottom [32], [36]. The voltage on the line creates an electric field between the line and the ground. This field is used by Pockels cell-based sensors to measure the voltage. The effect of the external field is eliminated by the resistive inner tube providing permittivity shielding [41].

Three electric field sensors are located in the inner tube: one in the middle, one near the high voltage, and one near the ground electrode. These sensors are connected to the optoelectronic system by fiber optic cables through the inner tube. The location of these sensors has a

crucial importance to the accuracy of voltage measurement. A numerical integration formula (Quadrature Method) is used to define the sensor locations. This method also minimizes the stray field effect for the electric field sensors, caused by the external electric field. The number of electric field sensors is optimized and defined as three for NXVT. Both resistive shielding and the Quadrature method help to reduce the electric field effect caused by neighboring phase voltages. Consequently, the accuracy of OVT becomes more reliable [34], [42].

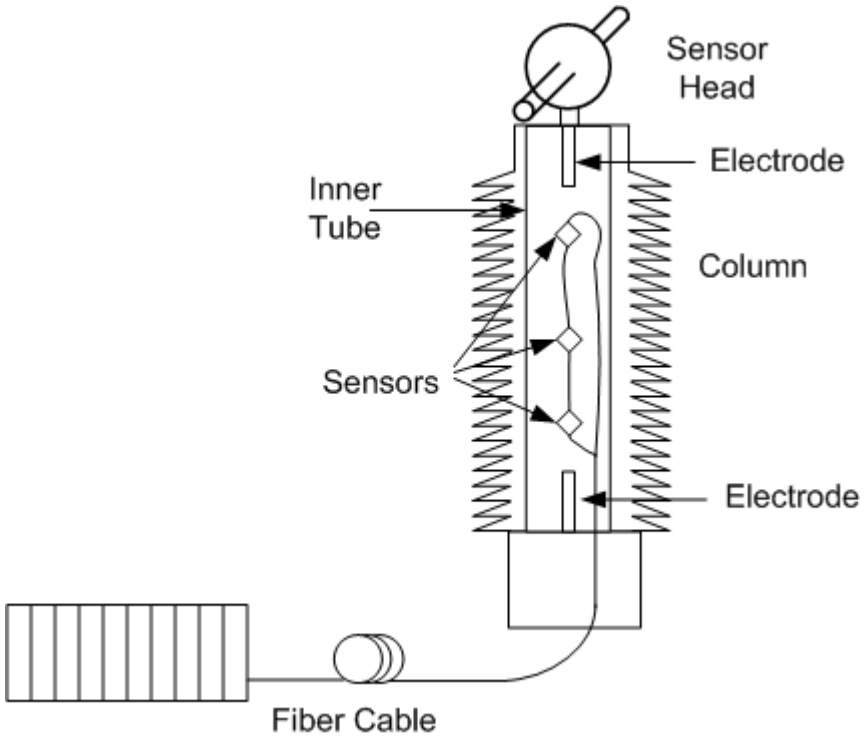

Fig. 3.1. NxtPhase optical voltage transformer [42]

The light signal from a light emitting diode is sent from the NxtPhase opto-electronics through the fiber optic cable. The light signal travels up the unit's column. Light enters sensors (Pockels cells) that are located halfway between the electrodes and the other two sensors, which are located above and below the middle sensor. While light passes through the sensors, the electric field, created by line-to-ground voltage, changes the polarization of the light from circular to elliptical. These changes at the three sensors are collected and processed by electronics to calculate the line-to-ground voltage of the line [32], [43].

Detected sensor signals are connected to opto-electronics in the control room through a fiber optic cable. These signals are processed, and analog and digital outputs are generated as a NXVT output signal. There is a 40 μs time delay because of this signal processing. At 60 Hz, digital phase compensation is used to set the phase displacement to 0 degrees [32].

Fig. 3.2 shows the block diagram of the OVT. It is similar to the OCT block diagram presented earlier. There are three outputs based on the standard. Analog output is tested in this study. The outputs are;

1. Digital output
2. Low voltage analog output (LEA) (4 V)
3. High voltage analog output (HEA) (69-115 V) [44]

The high energy analog output transformer ratio changed easily with software since it is an electronic system; 700:1 is used for the test purposes. The tested OVT is designed as a combined optical voltage and current transformer; however, only the OVT part is used.

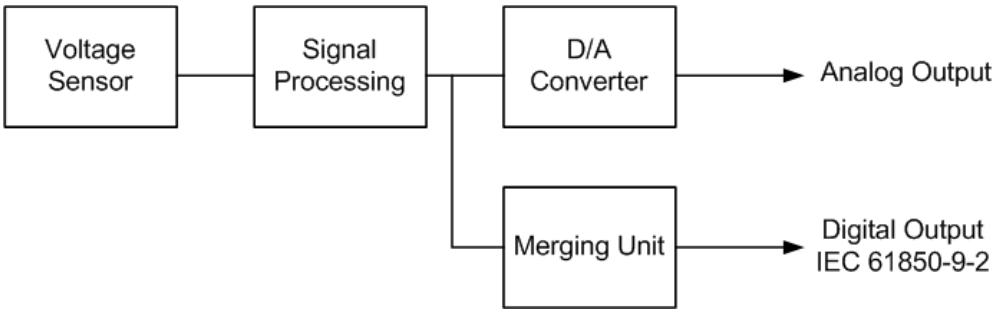

Fig. 3.2. OVT block diagram

3.3 Experimental Test Setup

The performance of the optical and magnetic VTs are measured and compared. The specification of the tested outdoor substation class magnetic CT is:

- Voltage 69 kV, BIL 350 kV
- Rated frequency: 60 Hz
- Weight: 600 lbs
- Pri Volts/ Sec Volts 40250 V/ 115 V
- Accuracy/Burden 0.3 0, W, X, M, Y, Z and ZZ

- 115 V high energy analog output

The optical VT specification is:

- Voltage: 145 kV, BIL: 650 kV
- One minute withstand voltage (wet): 275 kV
- Rated frequency: 60 Hz
- Weight: 320 lbs
- Rated maximum thermal current: 3000 A, Rated Short-circuit current : 40 kA
- 1C Accuracy (relaying): IEC 0.5/5P
- 2C Accuracy (metering): 1.2-30 A 0.30% , 30-600 A 0.30%
- Voltage accuracy: IEC class 0.2, IEEE class 0.3
- Rated delay time: 42 μs

The main difference between the two transformers is that the OVT is lightweight and it is even though designed as a combined optical transformer. This lightweight is considered one of the benefits of the OVT in the literature.

The laboratory testing of the VTs requires high voltage. A 100 kV, 5 kVA high voltage transformer, 200 kV impulse generator has been used to compare the magnetic VT and optical VT performance. Fig. 3.3 shows the connection diagram of the test system.

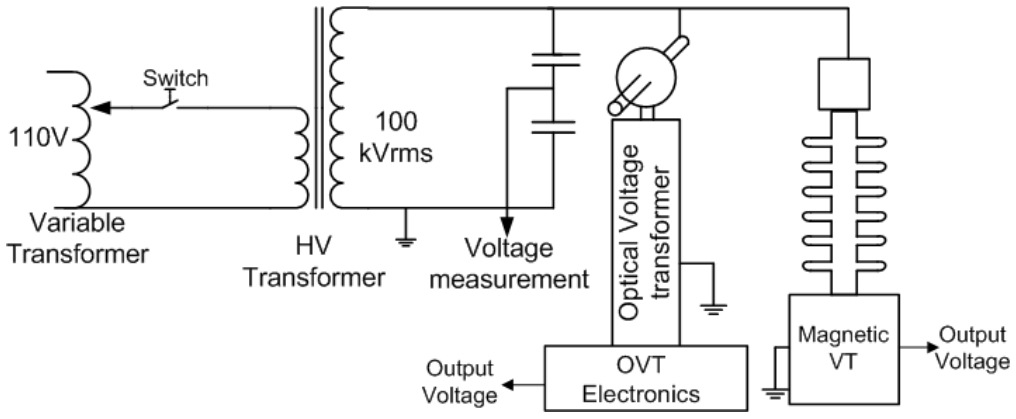

Fig. 3.3. Experimental test setup

Optical and magnetic voltage transformers are connected in parallel and supplied by the high voltage transformer. The voltage is varied by a regulating transformer. The maximum applied

voltage is 80 kV, which is more than the rated voltage of the magnetic transformer. The over-excitation is permitted in the investigation of the transformer's saturation effect on the measured voltage. The applied voltage is measured with a capacitive voltage divider. This divider is used to adjust the test voltage to the desired value.

The high energy analog (HEA) output of the optical VT was compared with the output voltage of the magnetic VT. The OVT output voltage was 1 V when the primary voltage was 700 V, and the magnetic VT has 2 V output voltage for 700 V primary voltage. These ratios were used for the calculations. Outputs of the two transformers were connected to the digital oscilloscope, which recorded the wave shapes and calculated the rms values of the voltages. Fig. 3.4 shows the laboratory environment and the test setup. The same oscilloscope that is used for current transformer tests is used. The same calibration and amplification methods are followed during the experiments.

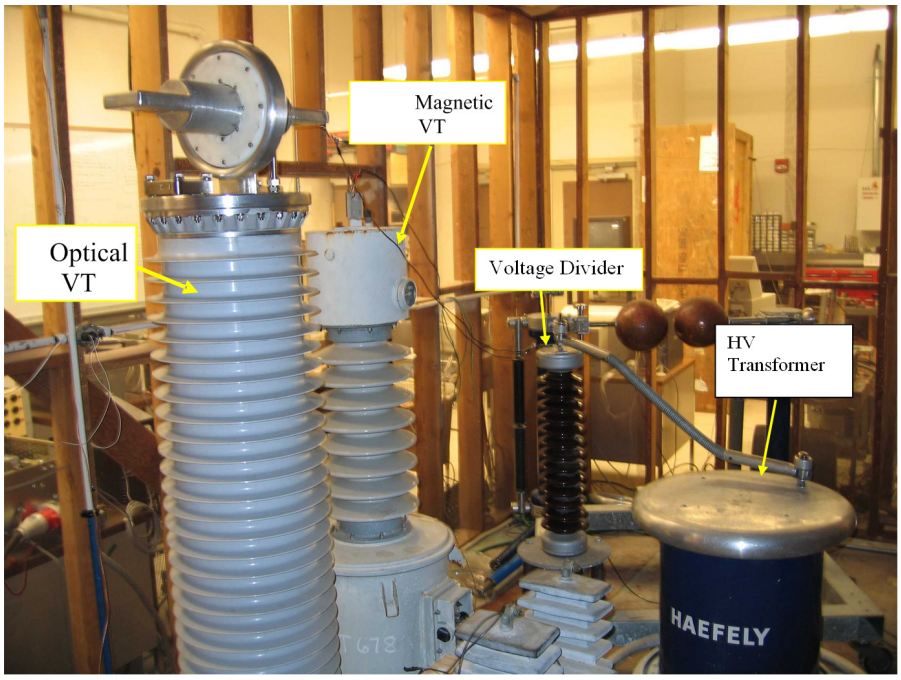

Fig. 3.4. Experimental test setup in laboratory environment

3.4 Steady State Performance

This test series aims to compare the two VT operations rather than verifying their accuracies since the manufacturers use standardized methods (IEC 60044, IEEE C57.13) to verify the

rating and accuracy of transformers before delivering them to their clients. It also intends to observe the linearity of the VTs as opposed to their absolute calibration. For the steady state response measurements, the voltage on the parallel-connected optical and magnetic transformer is increased in nine steps between 5 kV and 80 kV. The regulating transformer voltage is adjusted to the desired voltage level. The main switch on the control box is closed, and the VTs are energized. The waveform begins with a transient and gradually reaches its steady state value. The digital oscilloscope provides the rms value of the two output voltages in steady state condition. The obtained values are recorded manually. The tests are repeated by both increasing and decreasing the voltage level. The optical VT HEA output is compared with the output of the magnetic VT.

The recorded wave shapes of the transformers are compared. It is noticed that the OVT output voltage has white noise. Fig. 3.5 shows the recorded OVT output signal for maximum 1.8 kV. The measured peak-to-peak value of the noise is 2.2%. The peak-to-peak amplitude of the noise is independent from the voltage, and it is more observable at low voltages. Most of this noise may come from the oscilloscope and the waveform capture circuit.

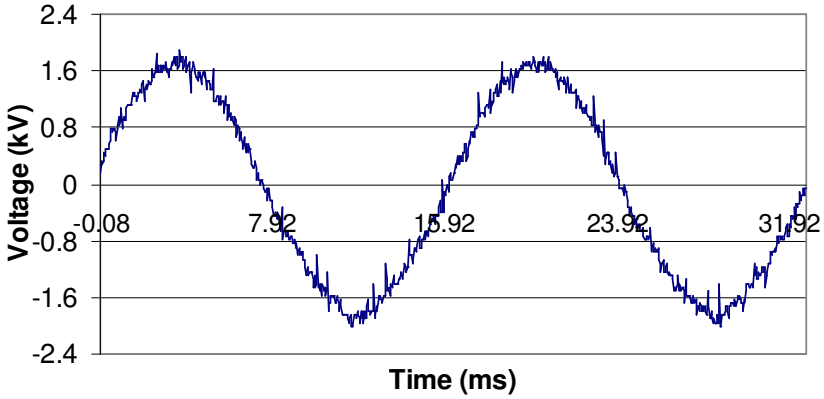

Fig. 3.5. OVT output signal

Optical systems have built-in noise, the amount of which depends upon the design, as described in Chapter 2. In general, the white noise average value is measured as zero with Gaussian distribution and filtering removing this white noise [39]. As the voltage increases, the white noise is less visible and the percentage decreases. Consequently, this noise does not have an effect in metering accuracy or the protection relay operation.

The applied voltage is increased gradually to 80,500 V in nine steps, and the output signals of the two transformers are compared. Although the high voltage transformer has a capability of generating 100 kV, maximum generated voltage is 80 kV. The impedance of the magnetic voltage transformer that is tested limits the generated voltage to 80 kV. Each of the nine steps is repeated five times. The average values for each step are given in Table 3-1. The values given in the table are the converted voltage values of the voltage outputs of the transformers.

Table 3-1
Test results for rms comparison of VTs

OVT (V)	*VT (V)*	*Difference (V)*	*Difference (%)*
4922.4	4956	33.6	0.677
9800	9870	70	0.709
24556	24696	140	0.566
34970.6	35000	29.4	0.084
40096	40250	154	0.382
49294	49700	406	0.816
59948	59500	448	0.752
70000	69300	700	1.010
80500	78120	2380	3.046

Table 3-1 shows the difference between the two VTs in volts and in percentage. In order to calculate the percentage difference, magnetic VT values are considered as base. It is seen that the percentage difference increases as the voltage increases. The maximum difference is 3.046%.

These test results also show the nonlinearity of the magnetic VT. It is noted that the applied voltage of 80,500 V is over the voltage ratings (69 kV) of the magnetic VT. Saturation is observed after 70 kV, and the output voltage sine wave is distorted. In order to investigate the optical VT linearity, the magnetic VT was removed from the circuit to increase the source voltage to supply optical VT. The voltage was applied up to the source limit of 100 kV that allows testing the optical VT over its voltage rating. The transformer ratio of the optical VT was adjusted to 700:1 V, which defines the voltage rating as 80,500 V (115x700=80,500 V). Results show that the OVT output is linear and no saturation effect was observed. The OVT output sine wave is not distorted. Fig. 3.6 shows the outputs of the two voltage transformers as functions of the primary current in

per unit (pu) scales. The figure shows the measurements after 0.7 pu values to make the nonlinearity more visible. The two lines are linear below 0.7 pu.

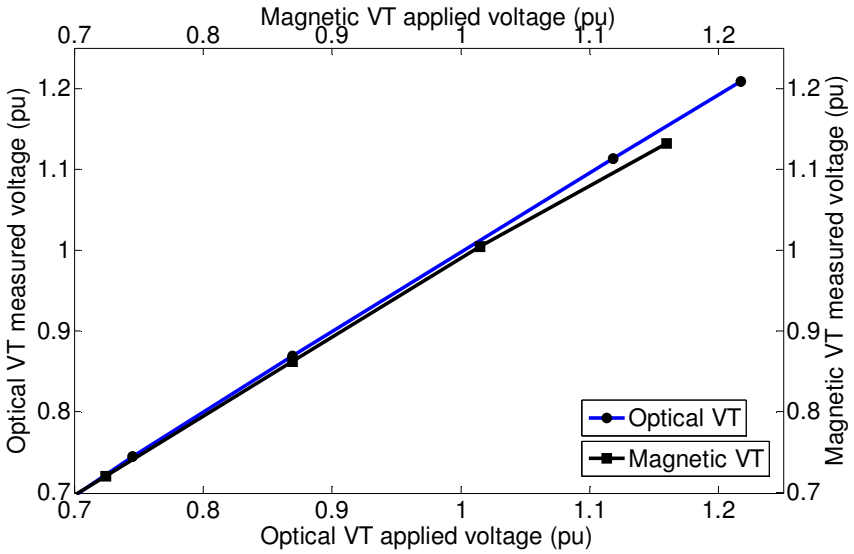

Fig. 3.6. Optical VT and magnetic VT linearity in rms

The output voltage signals of the two VTs are recorded simultaneously in the steady state condition. The point-by-point differences of the two sine waves are calculated by subtracting one measurement from the other. A digital oscilloscope noise filter is used during this measurement to reduce the inherent output noise of the signals. Fig. 3.7 shows the recorded one cycle voltage sine waves and the voltage level difference for this cycle. The figure shows that the maximum voltage difference in this cycle is 1,680 V, which is a high voltage level. A detailed investigation of this result shows that this difference is due to the phase difference between the voltage transformer output signals. The OVT output signal has a 42 μs delay, which is less than one degree (0.9 degrees) of equivalent phase offset. This delay is verified by measuring the time difference between the zero crossings of the two signals using the oscilloscope feature. This rated time delay is due to the transit time of the light and the digital signal processing. These results are within specifications of the devices under test.

3.5 Transient Performance

In this experiment, the transient performances of both voltage transformers are investigated by applying a lightning impulse signal. The VT responses to the standard 1.2 μs /50 μs lightning impulse are measured.

A standard 1.2 μs/ 50 μs impulse supplies the parallel-connected magnetic and optical VTs. The impulse voltage is measured by an impulse voltage divider and digital oscilloscope. The responses of the magnetic and optical VT are recorded with the same digital oscilloscope. The test is performed at 87 kV peak voltage level.

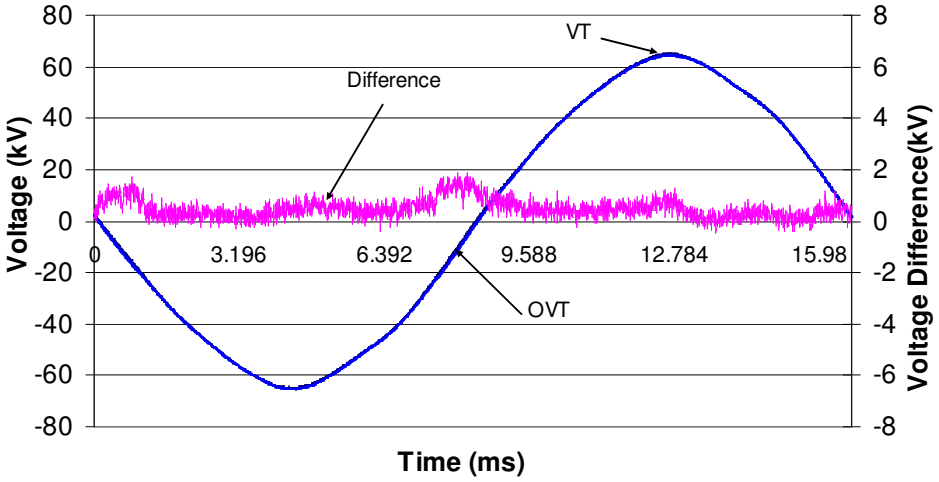

Fig. 3.7. Sine wave comparison of magnetic and optical VTs

Fig. 3.8 shows the applied impulse and the response of the OVT high energy analog (HEA) output. Fig. 3.8 shows that the optical VT delays the impulse by 40 μs as specified in OVT specifications. The rise time is increased from 1.2 μs to 13 μs. It can be seen that the perceived half time of the pulse also increases from 50 μs to 68 μs.

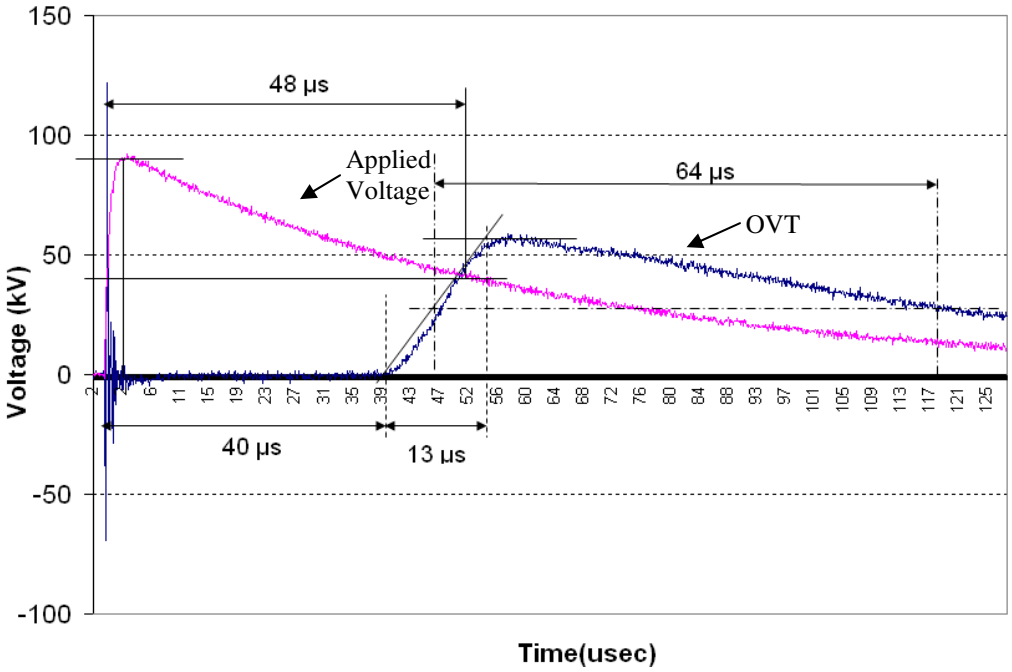

Fig. 3.8. OVT impulse response

The same lightning impulse signal is applied to the magnetic VT. The impulse produced large-scale oscillation. No delay is observed. The front time and half time cannot be determined. Fig. 3.9 shows the magnetic transformer response to the 87 kV lightning impulse. In summary, as expected, the magnetic VT does not reproduce the impulse voltage.

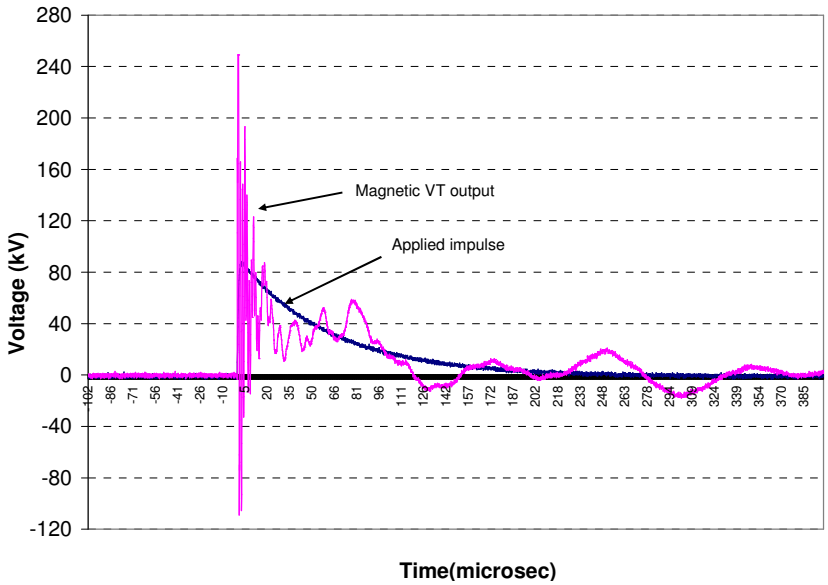

Fig. 3.9. Magnetic VT impulse response

The impulse tests show that the OVT has a delay, but it produces a lightning-type impulse with longer front and in half time. This shows that the OVT bandwidth response is much better than that of the magnetic VT, and the OVT can be used successfully for switching surge measurements.

3.6 Comparison of Magnetic and Optical VT Based on Field Recorded Data

One of the utility companies in the country has installed magnetic and optical VTs at one of their substations for protection. Optical VT high-energy-analog output and magnetic VT outputs are recorded by an event recorder and by protection relays when faults occurred. One of the selected faults is shown in Fig. 3.10. The recorded waveforms are expressed in primary voltage and plotted together. The differences of the two waveforms are calculated and plotted in the same figure. It can be seen that the difference is almost dominated by noise and the fault does not affect the measurement. The maximum difference is 7.7 kV (2.7% of maximum voltage) due to the noise in the signal and data acquisition system. This also shows that such a low level of noise has no impact on the performance of the protection system.

Among many recordings from the field records, different types of faults are selected and analyzed like those presented in Fig. 3.10. VT readings and recorded signals were compared, and the tripping signals were analyzed. The comparison shows that both VTs reproduced the primary voltage successfully, and the protection system operated properly.

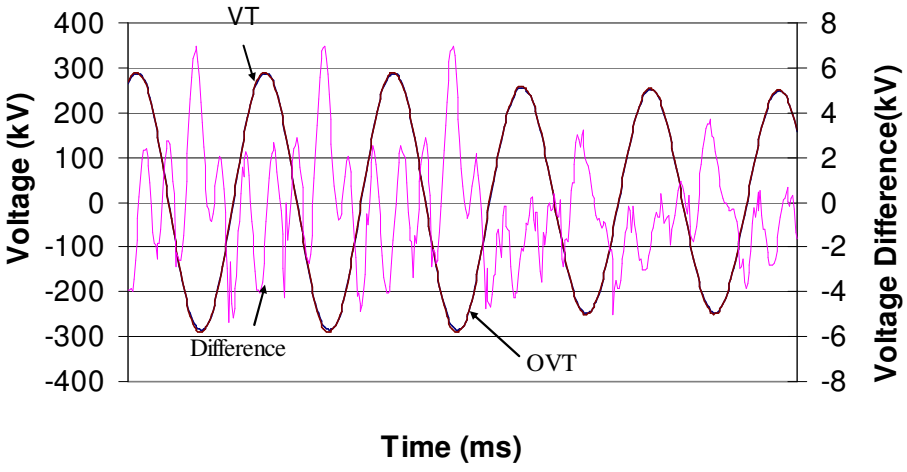

Fig. 3.10. Field recorded voltage sag event

3.7 Conclusion

This chapter used experimental work to compare the performance of an optical voltage transformer with a conventional magnetic voltage transformer. The results confirmed that the OVTs are suitable for power system protection and can replace the magnetic VTs. The details are:

1. The optical VT analog output has significantly higher bandwidths (40 kHz) than the magnetic VT does (1.5 kHz).
2. The OVT reproduced a lightning-type impulse with longer front end in half time.
3. The OVT analog output has significant white noise, but the white noise does not affect accuracy or protection performance.
4. The OVT output signal has a 40 μs delay, corresponding to 0.86 degree, that meets the manufacturer's data and is less than the permitted phase difference by the IEEE standard.

CHAPTER 4

DEVELOPMENT OF VARIOUS MODELS FOR OPTICAL INSTRUMENT TRANSFORMERS ANALOG OUTPUTS

4.1 Introduction

Developing an appropriate model for an optical instrument transformer is crucial for many power system applications such as protecting the system equipment against damages caused by system faults [45]. Instrument transformers reproduce the primary voltage and current signals to manageable values according to their characteristics. Specifically, the transient response of instrument transformers affects the reproduced signal characteristics. Therefore, producing models of instrument transformers is crucial for the relay testing and relay performance evaluations in Electromagnetic Transients Program (EMTP) transient studies [46], [47]. Precise representation of physical systems by a transfer function is always desirable for purposes of analysis and simulation. If there is not enough information about the structure of the system, frequency response (FR) measurements can be used as suitable data to approximate the transfer function parameters [48]. A frequency sweep/response method is beneficial to identify the key characteristics of the transformers for kHz levels and helpful to develop the wideband characteristics of transformers [49], [50]. The physical structure and operational principle of the transformers also give insight about the systems and are fundamental for the model developments.

Literature shows that the equivalent circuit models of magnetic instrument transformers have been developed for different purposes and for different frequency ranges in many studies [49], [51], and [52]. However, models for optical instrument transformers are not very well presented. A few modeling studies are performed only on optical elements of the current transformers in order to improve the accuracy, but a complete model that considers the optics and the electronics together is not presented. In addition, models for optical voltage transformer were not found in the literature.

The objective of this chapter is to present a method to develop various models for OCT and OVT analog outputs. Various well-known mathematical methods, such as network synthesis and Jones calculus methods are used for modeling purposes. Models are presented in three parts:

1. Analog model of analog output: Transformers are considered as a black box and frequency response characteristics are obtained experimentally. A transfer function in *s*-domain is approximated using the FR characteristics and an analog circuit model is developed from the transfer function.
2. Digital model of analog output: A developed analog model transfer function is converted to a digital model transfer function using bilinear transformation in order to simulate the transformer models in a digital environment. A direct form representation of the digital model is presented for simulation studies.
3. Complete model: The optics of the transformers and the electronics of the transformers are modeled separately and are combined together for the final model. The Jones calculus method is used to model optical elements of the transformers. The obtained FR characteristics and the developed analog/digital model transfer functions are used to model the electronics part.

4.2 Analog Model for OCT Analog Output

This method presents an analog model by considering the optical CT transformer as a black box. The model is represented by a transfer function and a circuit derived from the transfer function. The input data for this technique are the measured frequency response (FR) of the OCT, which has two parts: amplitude vs. frequency and phase-angle vs. frequency.

The steps of the procedure are:

1. Obtaining the frequency response of the system experimentally.
2. Approximation of polynomial transfer function coefficients using the frequency response data by the complex curve fitting method to minimize error.
3. Reconstruction of the developed transfer function as a sum of first order rational functions.

4. Combination of the first order transfer functions to the second order transfer functions.
5. Representation of the second order transfer functions by RLC circuits and of the remaining first order transfer functions by RL circuits.
6. Interconnection of the RLC and RL circuits to form the equivalent circuit representing the OCT or OVT.
7. Validation of the developed equivalent circuits.

4.2.1 Measurement of OCT Frequency Characteristics

One of the advantages of the OCT is that it has a better frequency response than the magnetic CT. According to the manufacturer, the OCT analog output has a built in 40-microsecond delay and a low pass filter with a cutoff frequency at 6 kHz (selectable). The OCT output above 20 kHz is almost zero. In order to verify the manufacturer specifications, the frequency response of the OCT is measured. These measurements are used for the development of the OCT model. The OCT is supplied by a current that has a variable frequency. The input current and the output voltages are measured and compared. Fig. 4.1 shows the experimental test setup.

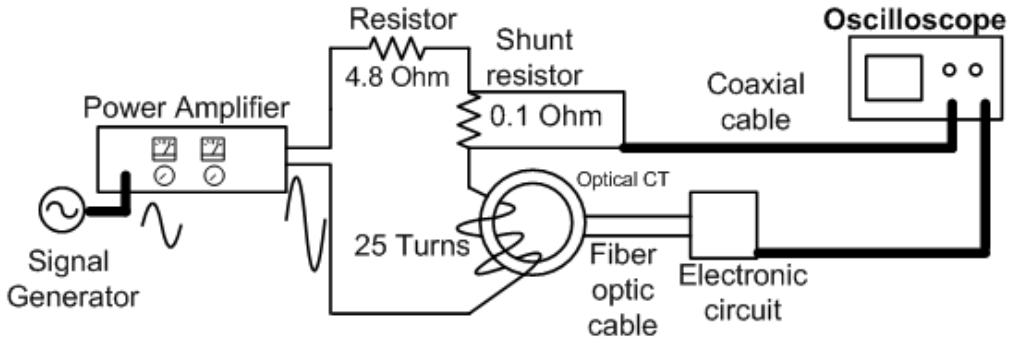

Fig. 4.1. Experimental setup for frequency response test

A signal generator, up to 1 MHz, is used as a signal source. The variable frequency output voltage of the signal generator is amplified by a 1,000 W power amplifier. The power amplifier is setup to mono-mode, and it supplies a current loop, which has 25 turns, through the Optical CT. In addition, the loop contains a 4.8-ohm limiting resistance and a 0.1-ohm measuring resistance. The power amplifier drives around 4 A current through the loop; this corresponds to 25 x

4=100 A. The frequency of the current is varied between 60 Hz ~ 16.8 kHz. Current in the loop is measured using voltage across the shunt resistance of 0.1 ohm as an Input 2 of the digital oscilloscope. Input 1 is used to measure the output voltage of the OCT. The voltage magnitude measurement accuracy of the oscilloscope is ± 2%. Fig. 4.2 shows the input current and OCT output voltage at 2 kHz frequency.

The loop current is kept constant while the frequency is varied for twelve different frequencies between 60 Hz to 16.8 kHz. The waveforms of both signals are recorded simultaneously with the rms value at each frequency. The time difference between the zero crossings of the signals are determined and converted to degrees by using the method in (4.1):

$$Phase.lag[\text{deg}] = \frac{Time.lag[\text{sec}] \times 360}{\frac{1}{f[Hz]}}$$

$$\frac{72.6 \times 10^{-6} \times 360}{\frac{1}{4000}} = 104.54^{\circ} \tag{4.1}$$

Fig. 4.3 shows the signals at 4 kHz and demonstrates the method used for phase angle calculation. This figure that the OCT output is lagging and the time difference is calculated as 72.6 µs where it is 104.54 degrees. A digital oscilloscope noise filter is used during this measurement to reduce the inherent output noise of the OCT signal.

The phase shift at 60 Hz is 40 µs, which corresponds to 0.86 degrees. According to the manufacturer, 27 µs of 40 µs delay is due to the 6 kHz analog filter, and 13 µs of 40 µs delay is due to the transit time of the light and the digital signal processing. The observation of the amplitude-frequency characteristics suggests that OCT frequency response can be represented by using a low-pass filter.

Table 4-1 shows the results of the measurements and calculated phase differences. Using the data in The phase shift at 60 Hz is 40 µs, which corresponds to 0.86 degrees. According to the manufacturer, 27 µs of 40 µs delay is due to the 6 kHz analog filter, and 13 µs of 40 µs delay is due to the transit time of the light and the digital signal processing. The observation of the ampli-

tude-frequency characteristics suggests that OCT frequency response can be represented by using a low-pass filter.

Table 4-1, the normalized amplitude-frequency and phase angle/frequency characteristics of the optical CT are plotted in Fig. 4.4.

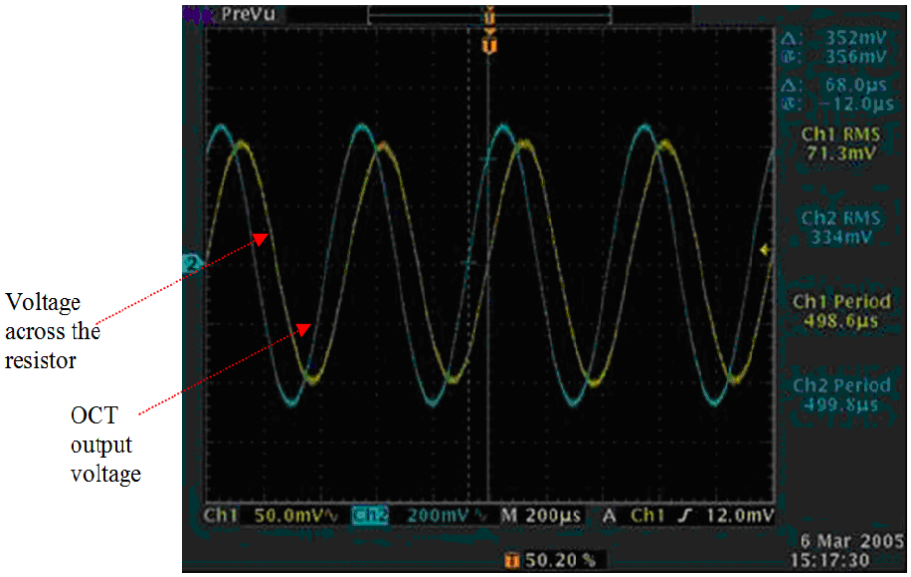

Fig. 4.2. Applied current and OCT output signals at 2 kHz

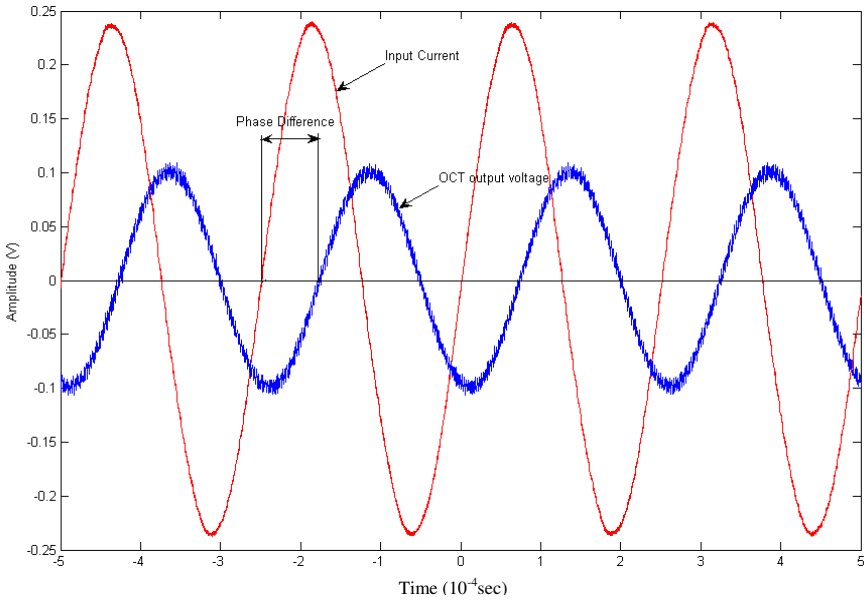

Fig. 4.3. Applied current and OCT output signals at 4 kHz

The phase shift at 60 Hz is 40 µs, which corresponds to 0.86 degrees. According to the manufacturer, 27 µs of 40 µs delay is due to the 6 kHz analog filter, and 13 µs of 40 µs delay is due to the transit time of the light and the digital signal processing. The observation of the amplitude-frequency characteristics suggests that OCT frequency response can be represented by using a low-pass filter.

Table 4-1
Frequency response test results

Freq (Hz)	*OCT (mV)*	*Current (A)*	*Resistor Voltage (mV)*	*Loop Current (A)*	*Normalized Amplitude*	*Phase Difference (µs)*	*Lagging*	*Phase (deg)*
60	92.1	3.684	438	4.38	1	40	OCT	-0.86
300	91.37	3.6548	437	4.37	0.992074	72	OCT	-7.78
1000	89.64	3.5856	437	4.37	0.971343	70	OCT	-25.20
2000	85.13	3.4052	437	4.37	0.924321	72.8	OCT	-52.42
4000	70.47	2.8188	437	4.37	0.763616	72.6	OCT	-104.54
6000	55.53	2.2212	437	4.37	0.601726	69.2	OCT	-149.47
7670	43.44	1.7376	437	4.37	0.466982	65.6	Current	-181.13
8200	40.17	1.6068	435	4.35	0.435284	55.2	Current	-197.05
10000	30.92	1.2368	438	4.38	0.335722	38	Current	-223.20
12000	22.48	0.8992	438	4.38	0.242624	23.2	Current	-259.78
14000	16.68	0.6672	437	4.37	0.181836	11.6	Current	-301.54
16800	11.51	0.4604	436	4.36	0.137844	1	NO diff	-353.95

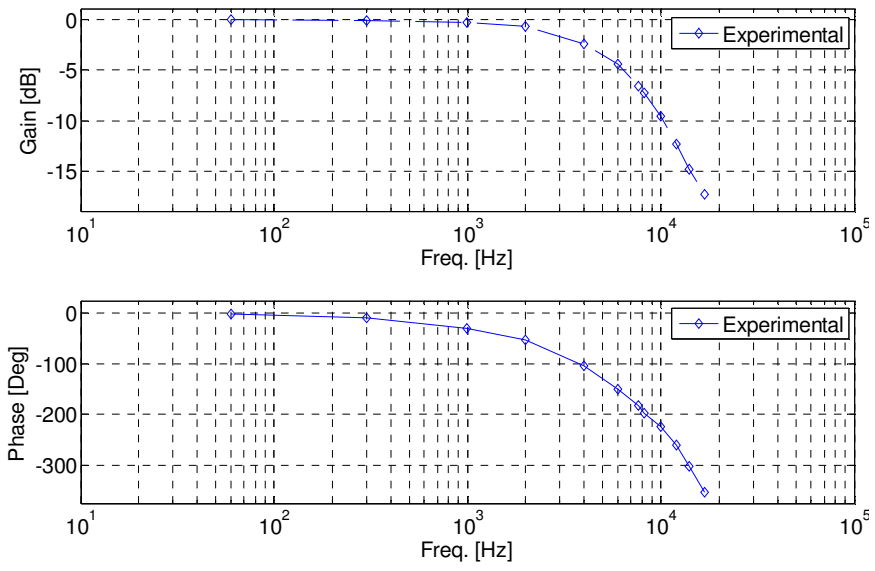

Fig. 4.4. Amplitude-frequency and phase angle-frequency characteristics of OCT

4.2.2 Development of Transfer Function Using the Frequency Response Data

Since the OCT is complex and has many components, it is desirable to identify a transfer function based on test results for modeling purposes. The transfer function can be defined by two functions, the amplitude ratio and phase angle, and it can be represented by a ratio of two polynomials

$$H(s) = \frac{B(s)}{A(s)} = \frac{b_0 + b_1 s^1 + b_2 s^2 + ...b_n s^n}{a_0 + a_1 s^1 + a_2 s^2 + ...a_m s^m} = \frac{\sum_n a_n s^n}{\sum_m b_m s^m} \tag{4.2}$$

where

- "n" and "m" are the rank of the polynomials (the order of the denominator is greater than or equal to the order of the numerator.)
- "a" and "b" are constant coefficients.

In order to develop the *H(s)* transfer function, determination of "a" and "b" coefficients is needed. The frequency response characteristics plots presented in Fig. 4.4 fit with the *H(s)* transfer function. A complex curve fitting method presented in [54] is used to determine the coefficients. In order to fit the measurement data and *H(s)* function, the *G(s)* transfer function is formed in polar form in terms of amplitude and phase for each frequency level. The numerical difference between the *G(s)* and *H(s)* transfer functions represents the error in fitting. This numerical iterative method uses Gauss-Newton iterations that search for the minimum error and estimates the *H(s)* transfer function.

$$error(s) = G(s) - H(s) \tag{4.3}$$

The Matlab® command "invfreqs" is used in this step. This function performs the least squares fit and identifies the transfer function using the amplitude and phase data [53]. Frequency vector, selected order of numerator and denominator, and selected number of iterations are the inputs to the function. The number of iterations is set to 50 to achieve sufficient accuracy of less than 2%. The order of the numerator and denominator are selected as 1, 2, 3, and 4 for numerator and 3, 4, 5, and 6 for denominator for optimization and to find the best fit. Some of the coeffi-

cients and the errors in amplitude and phase are given in Table 4-2. Results show that the best prediction is 3 for numerator and 5 for denominator. The program used for the fitting process is presented in Appendix A. The experimental values are changed by hand to test the robustness of the program. The program fallows the same procedure and develops new transfer functions within an error of less than 3%. Based on the experimental values, the approximate transfer function is

$$H(s) = \frac{-3.337.10^{9}\,s^{3} + 4.911.10^{14}\,s^{2} - 6.259.10^{19}\,s + 3.578.10^{24}}{s^{5} + 2.497.10^{5}\,s^{4} + 4.564.10^{10}\,s^{3} + 4.487.10^{15}\,s^{2} + 2.115.10^{20}\,s + 3.603.10^{24}} \qquad (4.4)$$

The error in the optimization process for each order number is calculated by comparing the frequency response of the derived transfer function with the measured frequency response. Fig. 4.5 shows the comparison for five-order system. The maximum error in amplitude is found to be 0.41%, and the maximum error in phase is 1.11% as shown in Table 4-2 for iteration number 3 for numerator and 5 for denominator. Considering the measurement accuracy as 2%, the deviation of 0.41% is a close fit. However, the user of the proposed method can select the values appropriate to specific applications. The program used for iteration of different order numbers is presented in Appendix A.

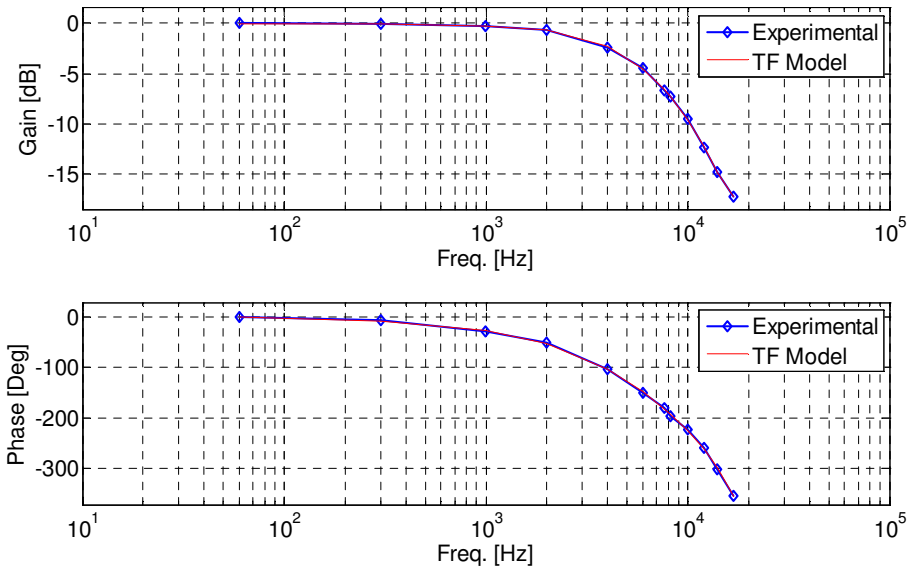

Fig. 4.5. Frequency response comparison of model and experimental results

Table 4-2
Transfer function coefficients for various iterations

	Order numbers (num / den)			
Coefficients	*3 / 4*	*4 / 5*	*3 / 5*	*4 / 6*
a_0	2.608e19	1.686e23	3.603e24	9.93e29
b_0	2.586e19	1.685e23	3.578e24	9.923e29
a_1	1.467e15	2.976e19	2.115e20	1.756e26
b_1	-5.133e14	1.633e19	-6.259e19	9.651e25
a_2	2.908e10	1.302e15	4.487e15	7.694e21
b_2	4.275e9	-3.493e14	4.911e14	-2.055e21
a_3	2.38e5	2.491e10	4.564e10	1.475e17
b_3	-2.938e4	2.868e9	-3.337e9	1.685e16
a_4	1	1.955e5	2.497e5	1.167e12
b_4		-2.061e4	0	-1.211e11
a_5		1	1	6.01e6
b_5				0
a_6				1
Maximum Error (%) Amplitude	0.52	1.04	0.41	1.03
Maximum Error (%) Phase	1.20	1.13	1.11	1.12

4.2.3 Reconstruction of the Developed Transfer Function as Sum of First Order Rational Functions and Their Circuit Implementations

The developed transfer function can be written in terms of rational functions using real poles, complex conjugate poles, and residues as follows;

$$f(s) = \sum_{n=1}^{N} \frac{c_n}{s - a_n} + d \tag{4.5}$$

where c_n are residues, a_n are poles, and N is the total number of poles. The poles and residues can be real or complex conjugate pairs, but d is always real [51]. The developed transfer function in (4.4) has two complex conjugate pair and one real pole as shown in Table 4-3.

Complex conjugate poles and residues have two parts: real (p_{rn} and c_{rn}), and imaginary (p_{in} and c_{in}). The residues are represented as z and $c_{2n} = c_{rn} - jc_{in}$ where $n = 1,2,....,K$ and K is

the number of complex conjugate pole pairs. The poles are represented as $a_{2n-1} = -p_{rn} + jp_{in}$ and $a_{2n} = -p_{rn} - jp_{in}$ where $n = 1,2,....,K$.

Table 4-3
Poles and zeros of transfer function

Residues [c_n] ($x10^5$)	*Poles [a_n] ($x10^5$)*	*Constant [d]*
-0.1261-j0.1297	-0.4610 + j1.4201	0
-0.1261+j0.129	-0.4610 – j1.4201	
-1.2140+j2.3843	-0.6015 + j0.2686	
-1.2140-j2.3843	-0.6015 - j0.2686	
2.6802	-0.3724	

The rational functions can be classified as $\frac{c_n}{s-a_n}$ for real poles, $\frac{c_{rn}+jc_{in}}{s-(p_{rn}+jp_{in})}+\frac{c_{rn}-jc_{in}}{s-(p_{rn}-jp_{in})}$ for complex conjugate pole pairs, and d for the constant. Based on these classifications, the approximated transfer function can be re-written as follows:

$$H(s) = \underbrace{\left.\begin{aligned} &\frac{(-0.1261 - j0.1297)\times 10^5}{s-(-0.4610+j1.4201)\times 10^5}+\frac{(-0.1261+j0.1297)\times 10^5}{s-(-0.4610-j1.4201)\times 10^5}+ \\ &\frac{(-1.2140+j2.3843)\times 10^5}{s-(-0.6015+j0.1286)\times 10^5}+\frac{(-1.2140-j2.3843)\times 10^5}{s-(-0.6015-j0.1286)\times 10^5}+ \end{aligned}\right\}}_{\text{Complex conjugate pole pairs}} \underbrace{\frac{(2.6802)\times 10^5}{s-(-0.3724)\times 10^5}}_{\text{Real pole}} \tag{4.6}$$

The electrical circuit model for OCT can be developed after forming the transfer function in terms of rational functions and a constant. The summation of rational transfer functions means parallel connections of circuits of each transfer function are present [56]. As an implementation process, the method presented in [51] and [55] is used; however, these methods need correction and more explanation. The first step of modeling is circuit implementation of each rational function and the constant. Each rational function or pair of rational functions is implemented as a series of circuit elements. The real poles that have low-pass filter characteristics are implemented as

RL, and complex conjugate pole pairs that have band-pass filter characteristics are implemented as RLC circuits. Each pole is implemented as follows:

Real Poles: The real poles are represented as a low-pass filter with a series connection of L and R, and a Voltage Control Voltage Source (VCVS). This circuit is similar to a typical RL low-pass filter where the transfer function *A(s)* is in (4.7).

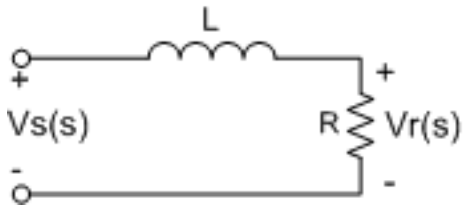

Fig. 4.6. Typical low-pass filter circuit

$$A(s) = \frac{V_r(s)}{V_s(s)} = \frac{R}{sL + R} \tag{4.7}$$

Substituting 1Ω into the *A(s)* transfer function in place of R in (4.7) yields $A(s) = \frac{1}{sL+1}$.

The real pole rational function of the transfer function is a form of $F_1(s) = \frac{C_n}{s - a_n} = \frac{(2.6802)\times 10^5}{s - (-0.3724)\times 10^5}$. This function is similar to the *A(s)* transfer function of RL circuit; however, it needs some manipulation. In order to make $\frac{1}{sL+1} = \frac{C_n}{s - a_n}$, a "$G_1$" multiplication factor is used as

$$\frac{1}{sL+1} = G_1 \frac{1}{\frac{s}{p_n} + 1} \tag{4.8}$$

where $G_1 = \frac{C_n}{p_n} = \frac{2.6802\times 10^5}{0.3724\times 10^5} = 7.1971$ and, hence, $L = \frac{1}{p_n} = \frac{1}{0.3724\times 10^5} = 26.85\mu H$. G_1 can be called the multiplication factor of the 1Ω resistor voltage and be represented with a VCVS where the G_1 is the gain. As a result, the circuit is a typical RL low-pass filter circuit with the addi-

tion of a VCVS. Circuit parameters are founded for the inductor as 26.85 μH for resistor 1Ω, and for VCVS gain 7.1971. Fig. 4.7 shows the final circuit for real pole rational function representation.

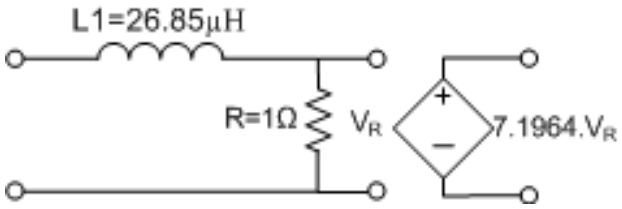

Fig. 4.7. Real pole implementation circuit

Complex poles: The transfer function has two complex conjugate pairs. Each pair is re-formed and two rational functions are summed in order to make the function similar to well-known transfer functions in terms of *s* as follows:

$$\frac{c_{rn}+jc_{in}}{s-(p_{rn}+jp_{in})}+\frac{c_{rn}-jc_{in}}{s-(p_{rn}-jp_{in})}$$
$$=\frac{(-0.1261-\mathrm{j}0.1297)\times10^5}{s-(-0.4610+j1.4201)\times10^5}+\frac{(-0.1261+j0.1297)\times10^5}{s-(-0.4610-j1.4201)\times10^5} \quad (4.9)$$

After going further in calculations and formulating the function as rational functions of *s*, the function can be re-written as the sum of two functions as follows:

$$F_2(s)=\frac{2c_{rn}p_{rn}-2p_{in}c_{in}}{s^2+2p_{rn}s+{p_{rn}}^2+{p_{in}}^2}+\frac{2c_{rn}s}{s^2+2p_{rn}s+{p_{rn}}^2+{p_{in}}^2}$$
$$F_2(s)=\underbrace{\frac{2.522\times10^9}{s^2+9.22\times10^4\mathrm{s}+2.229\times10^{10}}}_{B_1(s)}+\underbrace{\frac{-2.522\times10^4 s}{s^2+9.22\times10^4\mathrm{s}+2.229\times10^{10}}}_{B_2(s)} \quad (4.10)$$

The $F_2(s)$ transfer function is formed as the sum of two transfer functions, $B_1(s) + B_2(s)$, where each function has band-pass filter characteristics. $B_1(s)$ is implemented as a series RLC band-pass filter circuit, and $B_2(s)$ is implemented as a parallel band-pass filter circuit. In both circuits, an additional VCVS is used as a multiplication factor. $B_1(s)$ implementation is as follows:

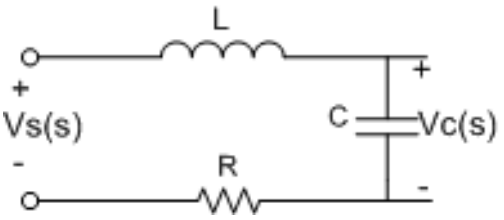

$$C_1(s) = \frac{V_c(s)}{V_s(s)} = \frac{1}{1 + sCR + s^2 LC}$$

Fig. 4.8. Typical low-pass filter circuit and its transfer function

A typical RLC low pass filter has the circuit and the transfer function as given in Fig. 4.8. If R is selected as 1Ω then the transfer function becomes $C_1(s) = \frac{1}{1 + sC + s^2 LC}$. On the other hand, $B_1(s)$, one part of developed transfer functions, has a form of

$$B_1(s) = \frac{2c_{rn}p_{rn} - 2p_{in}c_{in}}{s^2 + 2p_{rn}s + p_{rn}^2 + p_{in}^2} = \frac{D}{E + sF + s^2 G} = \frac{2.522\times10^9}{s^2 + 9.22\times10^4 s + 2.229\times10^{10}}, \tag{4.11}$$

which is similar to $C_1(s)$ but needs some manipulation. In order to make $C_1(s) = B_1(s)$, the "G_2" multiplication factor is used as

$$\frac{1}{1 + sC + s^2 LC} = G_2 \frac{1}{1 + Ys + Xs^2} \tag{4.12}$$

where

$$\begin{aligned}
G_2 &= 2\frac{c_{rn}p_{rn} - p_{in}c_{in}}{p_{rn}^2 + p_{in}^2} = \frac{2.522\times10^9}{2.229\times10^{10}} = 0.1131 \\
Y = C &= \frac{2p_{rn}}{p_{rn}^2 + p_{in}^2} = \frac{9.2198\times10^4}{2.229\times10^{10}} = 4.1363\mu F \\
X = LC &= \frac{1}{p_{rn}^2 + p_{in}^2} = \frac{1}{2.229\times10^{10}} = 4.4863\times10^{-11} \\
L &= \frac{X}{C} = \frac{1}{2p_n} = \frac{1}{9.2198\times10^4} = 10.846\mu H
\end{aligned} \tag{4.13}$$

As a result, the circuit parameters are found for the inductor as 10.846 μH, for capacitor as 4.1363 μF, for resistor 1Ω, and for the VCVS gain 0.1131; there are shown in Fig. 4.9.

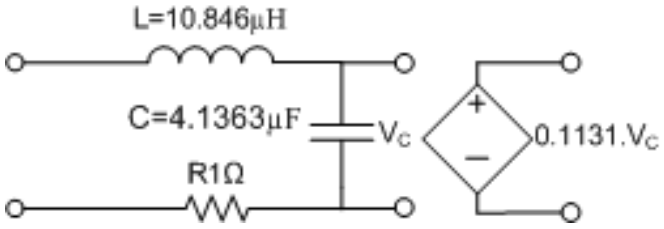

Fig. 4.9. *$B_1(s)$* implementation circuit

$B_2(s)$ implementation is implied in a similar way. Parallel RLC connection of a band-pass circuit is used for implementation as follows:

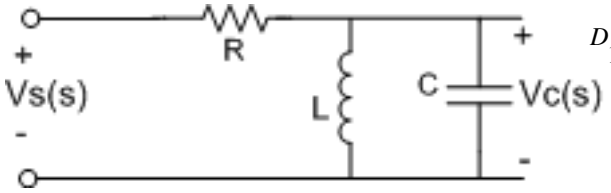

$$D_1(s) = \frac{V_C(s)}{V_S(s)} = \frac{sL}{R + sL + s^2 RLC}$$

Fig. 4.10. Typical band-pass filter circuit and its transfer function

A typical RLC band-pass filter has the circuit and the transfer function as given in Fig. 4.10. If R is selected as 1Ω, then the transfer function of the circuit becomes $D_1(s) = \frac{V_C(s)}{V_S(s)} = \frac{sL}{1 + sL + s^2 LC}$. On the other hand, *$B_2(s)$*, one part of developed transfer function, has a form of

$$B_2(s) = \frac{2c_{rn}s}{s^2 + 2p_{rn}s + p_{rn}^2 + p_{in}^2} = \frac{Ds}{E + sF + s^2 G} = \frac{-2.522\times10^4 s}{s^2 + 9.22\times10^4 s + 2.229\times10^{10}}, \qquad (4.14)$$

which is similar to *$D_1(s)$*. However, it needs some manipulation. In order to make *$D_1(s)$* = *$B_2(s)$*, the "*G_3*" multiplication factor is used as

$$\frac{sL}{1 + sC + s^2 LC} = G_3 \frac{Ys}{1 + Ys + Xs^2} \qquad (4.15)$$

where

$$G_3 = \frac{c_{rn}}{p_{rn}} = \frac{-1.2609\times10^{4}}{4.6099\times10^{4}} = -0.2735$$

$$Y = L = \frac{2p_{rn}}{p_{rn}^{2} + p_{in}^{2}} = \frac{9.2198\times10^{4}}{2.229\times10^{10}} = 4.1363\mu H$$

$$X = LC = \frac{1}{p_{rn}^{2} + p_{in}^{2}} = \frac{1}{2.229\times10^{10}} = 4.4863\times10^{-11}$$

$$C = \frac{X}{L} = \frac{1}{2p_{n}} = \frac{1}{9.2198\times10^{4}} = 10.846\mu F \tag{4.16}$$

As a result, the circuit parameters are found for the inductor as 4.4863 µH, for capacitor as 10.846µF, for resistor 1Ω, and for VCVS gain -0.2735; the circuit is given in Fig. 4.11.

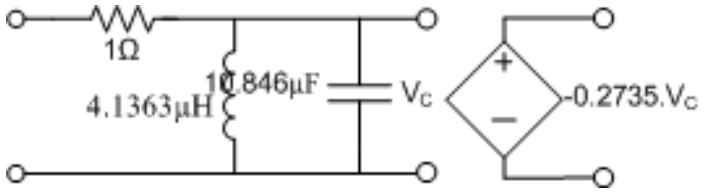

Fig. 4.11. $B_2(s)$ implementation circuit

The same procedure is applied for the second complex conjugate pair pole as follows:

$$\frac{c_{rn} + jc_{in}}{s-(p_{rn} + jp_{in})} + \frac{c_{rn} - jc_{in}}{s-(p_{rn} - jp_{in})}$$

$$= \frac{(-1.2140 + \text{j}2.3843)\times10^{5}}{s-(-0.6015 + \text{j}0.1286)\times10^{5}} + \frac{(-1.2140 - \text{j}2.3843)\times10^{5}}{s-(-0.6015 - \text{j}0.1286)\times10^{5}} \tag{4.17}$$

After further calculations and making the function as rational functions of *s*, the function can be re-written as the sum of two functions as follows:

$$F_3(s) = \underbrace{\frac{-2.741\times10^{10}}{s^{2} + 1.203\times10^{5}\text{s} + 4.34\times10^{9}}}_{B_3(s)} + \underbrace{\frac{-2.428\times10^{5}\,s}{s^{2} + 1.203\times10^{5}\text{s} + 4.34\times10^{9}}}_{B_4(s)} \tag{4.18}$$

$F_3(s)$ transfer function is formed as the sum of two transfer functions, $B_3(s) + B_4(s)$. Each part is implemented as series of RLC circuits. For $B_3(s)$ following circuit is considered:

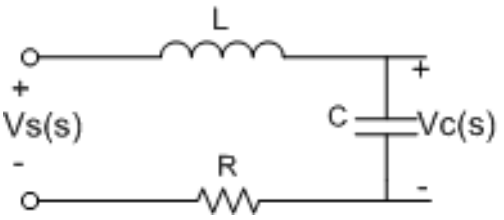

$$E_1(s) = \frac{V_C(s)}{V_S(s)} = \frac{1}{1 + sCR + s^2 LC}$$

Fig. 4.12. Typical low-pass filter circuit and its transfer function

If R is selected as 1Ω, then the transfer function becomes $E_1(s) = \dfrac{1}{1 + sC + s^2 LC}$. On the other hand, $B_3(s)$ in (4.18) has a form of

$$B_3(s) = \frac{2c_{rn}p_{rn} - 2p_{in}c_{in}}{s^2 + 2p_{rn}s + p_{rn}^2 + p_{in}^2} = \frac{D}{E + sF + s^2 G} = \frac{-2.741\times10^{10}}{s^2 + 1.203\times10^5 s + 4.34\times10^9}, \tag{4.19}$$

which is similar to $E_1(s)$; however, it needs some manipulation. In order to make $E_1(s) = B_3(s)$, the "G_4" multiplication factor is used as

$$\frac{1}{1 + sC + s^2 LC} = G_4 \frac{1}{1 + Ys + Xs^2} \tag{4.20}$$

where

$$\begin{aligned}
G_4 &= 2\frac{c_{rn}p_{rn} - p_{in}c_{in}}{p_{rn}^2 + p_{in}^2} = \frac{-2.741\times10^{10}}{4.34\times10^9} = -6.3157 \\
Y = C &= \frac{2p_{rn}}{p_{rn}^2 + p_{in}^2} = \frac{2.4061\times10^5}{4.34\times10^9} = 27.721\mu F \\
X = LC &= \frac{1}{p_{rn}^2 + p_{in}^2} = \frac{1}{4.34\times10^9} = 2.304\times10^{-10} \\
L &= \frac{X}{C} = \frac{1}{2p_n} = \frac{1}{1.2031\times10^5} = 8.3121\mu H
\end{aligned} \tag{4.21}$$

As a result, the circuit parameters are found for the inductor as 8.3121μH, for capacitor as 27.721μF, for resistor 1Ω, and for VCVS gain ratio is -6.3157.

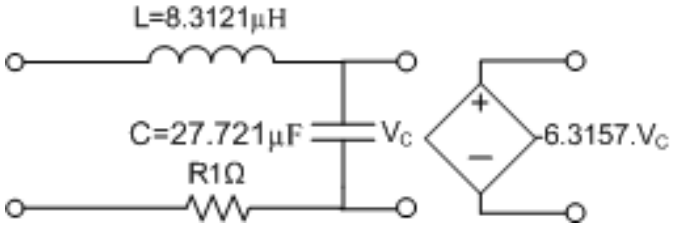

Fig. 4.13. *$B_3(s)$* implementation circuit

$B_4(s)$ implementation is developed in a similar way. A parallel RLC connection of a band-pass circuit is used for implementation as follows:

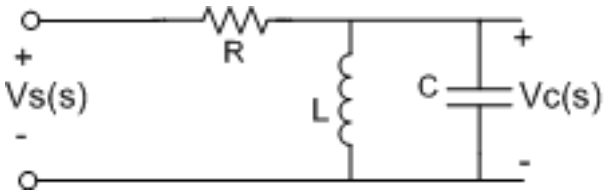

$$F_1(s) = \frac{V_C(s)}{V_S(s)} = \frac{sL}{R + sL + s^2 RLC}$$

Fig. 4.14. Typical band-pass filter circuit and its transfer function

If R is selected as 1Ω, then the transfer function becomes $F_1(s) = \frac{V_C(s)}{V_S(s)} = \frac{sL}{1 + sL + s^2 LC}$. On the other hand, *$B_4(s)$* has a form of

$$B_4(s) = \frac{2c_{rn}s}{s^2 + 2p_{rn}s + p_{rn}^2 + p_{in}^2} = \frac{Ds}{E + sF + s^2 G} = \frac{-2.428\times10^5 s}{s^2 + 1.203\times10^5 s + 4.34\times10^9}, \qquad (4.22)$$

which is similar to *$F_1(s)$;* however, it needs some manipulation. In order to make *$F_1(s) = B_4(s)$,* the "*G_5*" multiplication factor is used as

$$\frac{sL}{1 + sC + s^2 LC} = G_5 \frac{Ys}{1 + Ys + Xs^2} \qquad (4.23)$$

where

$$G_5 = \frac{c_{rn}}{p_{rn}} = \frac{-1.214\times10^5}{6.0154\times10^4} = -2.0182$$

$$Y = L = \frac{2p_{rn}}{p_{rn}^2 + p_{in}^2} = \frac{1.2031\times10^5}{4.3398\times10^9} = 27.722\mu H$$

$$X = LC = \frac{1}{p_{rn}^2 + p_{in}^2} = \frac{1}{4.3398\times10^9} = 2.3043\times10^{-10}$$

$$C = \frac{X}{L} = \frac{1}{2p_n} = \frac{1}{1.2031\times10^5} = 8.3121\mu F \tag{4.24}$$

As a result, the circuit parameters are found for the inductor as 27.722 µH, for the capacitor as 8.3121µF, for resistor 1Ω, and for VCVS gain -2.0182.

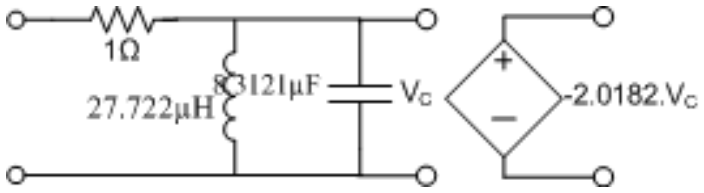

Fig. 4.15. *$B_4(s)$* implementation circuit

4.2.4 Interconnection of the RLC Circuits to Form the Equivalent Circuit Representing the OCT

Fig. 4.16 shows the connection of the developed circuits for each transfer function that forms the final circuit model for OCT. The real and complex poles are implemented as RL and RLC circuits, respectively. The *G* multiplication factors are represented with a VCVS, and the gain of the VCVS is selected as the *G* multiplication factors. The primary sides of the circuits are connected in parallel and the secondary sides of the circuits are connected in series. A VCVS that represents the transformer ratio added to the circuit and 1 ohm resistor is connected to generate voltage input for the circuit. The circuit elements are calculated and shown in Table 4-4.

Table 4-4
Transfer function coefficients for various iterations

L *(µH)*	*C* *(µF)*	*G*
L1=26.85	C1=4.1363	G1=7.1964
L2=10.846	C2=10.846	G2=0.1131
L3=4.1363	C3=27.722	G3=-0.2735
L4=8.3121	C4=8.3121	G4=-6.3166
L5=27.722		G5=-2.0182

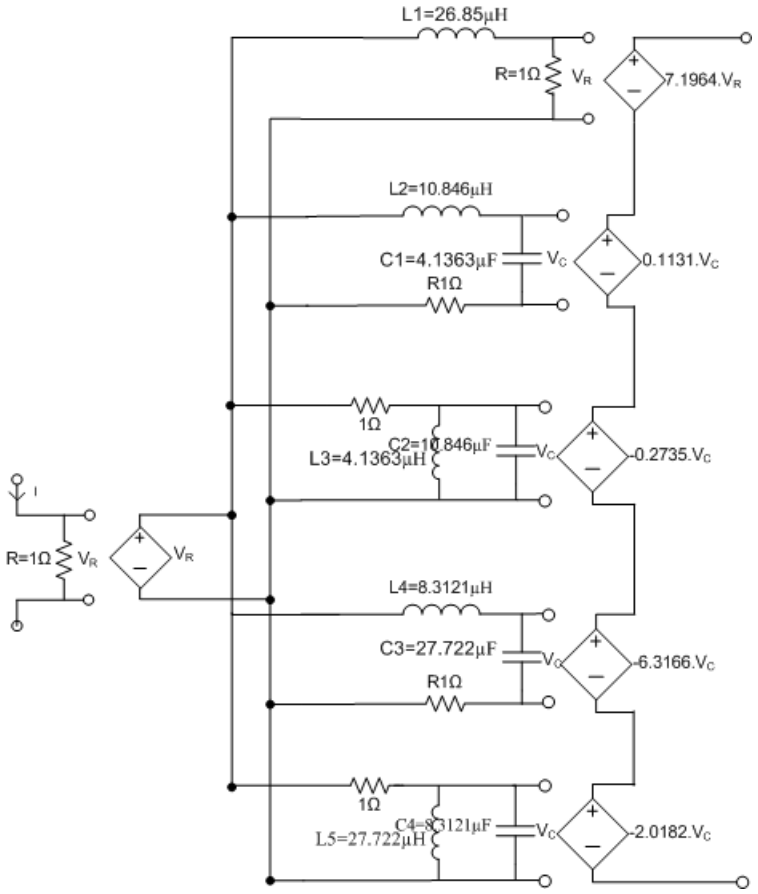

Fig. 4.16. OCT equivalent circuit model

4.2.5 Validation of the Developed Transfer Function and Equivalent Circuit Models

In order to validate the developed models, two types of comparisons are performed for transfer functions and circuit models. Both model outputs are compared with experimental test data. Results are presented in the same plots, and errors are given based on the experimental data. The types of comparison are:

1. Comparison of frequency response characteristics of transfer function and circuit models with experimental frequency response test results.
2. Transfer function and electrical circuit models are supplied with an experimental test signal that is close to a step function presented in Chapter 2.

Fig. 4.17 shows the frequency response comparison. It is seen that both the transfer function and circuit models follow the experimental test results. The errors are given in percentages in Table 4-5 where the experimental results are based. Compared to the 2% experimental errors, the results are within the desired range and show that the models can represent the OCT in simulation studies.

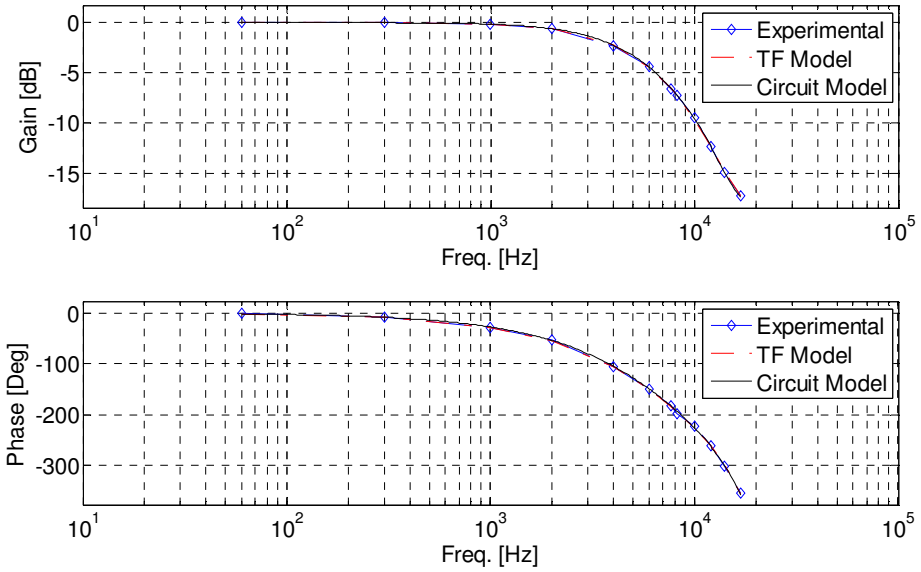

Fig. 4.17. Frequency response comparison of developed models

Fig. 4.18 shows the second comparison method's result. A step like signal is applied to OCT, and the output and input signals are recorded as presented in Chapter 2. The same signal is applied to the approximated *H(s)* transfer function and the output is recorded. The same input signal is applied to the circuit model in PSpice simulation. The circuit output is recorded and plotted together with the experimental output and the transfer function output. As seen from Fig. 4.18, the model outputs follow the experimental output. The transfer function output and the circuit model output are very close to each other. This shows that the developed circuit model from the transfer function is successful. Based on the experimental output signal, the maximum error for both models is 12%. Considering the noisy experimental test data, this much error is reasonable. The program used for calculations is presented in Appendix A.

Table 4-5
Errors between models and experimental results

Errors	*Amplitude*	*Phase*
Transfer function	0.41%	1.11%
Circuit Model	1.43%	0.72%

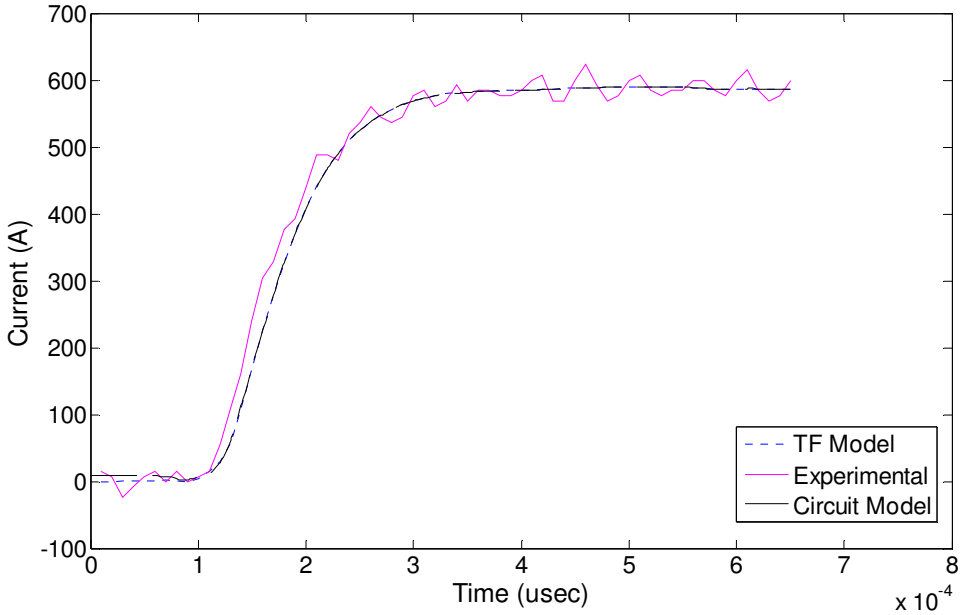

Fig. 4.18. Comparison of model output signals with experimental output signal

4.3 Digital Model for OCT Model

Since the OCT is based on electronics and it includes a signal-processing unit, it would be beneficial to use digital representation of the analog output in addition to the analog model for simulation purposes. There are commonly used techniques to design a digital filter that represents an analog filter. One of these methods is to make the frequency response of the digital filter match the frequency response of the analog filter. The bilinear transformation method is used to transform the *s*-domain transfer function developed in the previous section, *H(s)*, into the *z*-domain transfer function, *H(z)*. The Bilinear transformation is an exact mapping of the z-plane to the s-plane by performing the following transformation:

$$s \to \frac{2}{T}\frac{z-1}{z+1} \quad \text{or} \quad z \to \frac{2+sT_s}{2-sT_s} \tag{4.25}$$

where T is the sampling time. This method successfully transforms any stable continuous time system into a stable discrete time system [57]. The transformation from $H(s)$ to $H(z)$ is performed using the Matlab® "c2d" command with a sampling rate of 7.8125μs, and the calculation method is selected as "Tustin." $H(z)$ is found as:

$$H(z)=\frac{-0.01102z^5+0.01763z^4+0.0156z^3-0.03298z^2+0.01282z^1+0.03276}{z^5-2.738z^4+3.394z^3-2.425z^2+0.9712z-0.1669} \tag{4.26}$$

The frequency response of the $H(s)$ and $H(z)$ are compared with experimental data and shown in Fig. 4.19. It is seen that the two responses match and follow each other successfully. The residues and poles of the $H(z)$ transfer function are calculated and presented in Table 4-6. By looking at the poles and zeros and the z-map of the transfer function, it is seen that all the poles are inside the unit circle and the system is stable.

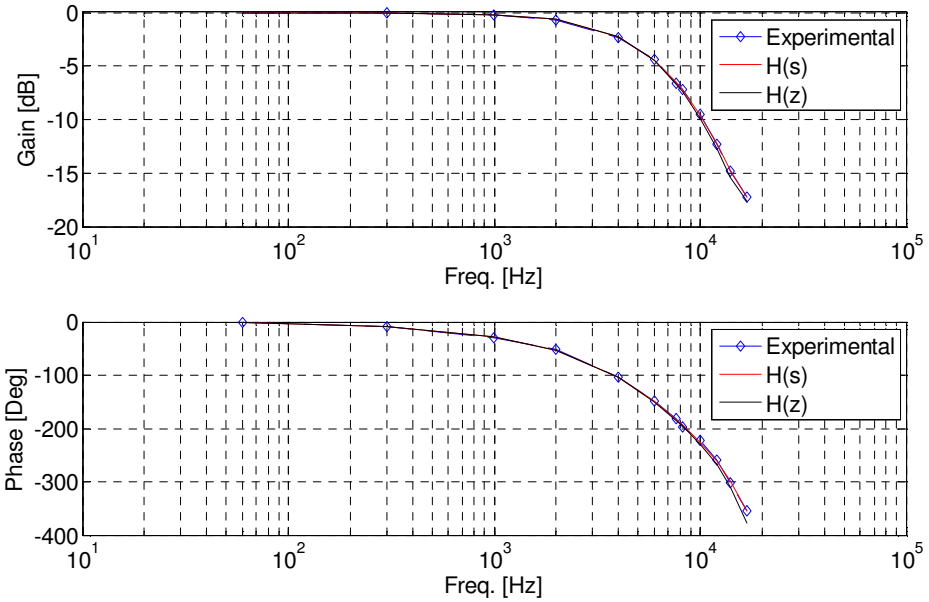

Fig. 4.19. Comparison of $H(s)$ and $H(z)$ frequency responses

Table 4-6
Poles and residues of transfer function

Residues	*Poles*	*Constant*
0.0089-j0.0826	0.3881+j0.6525	-0.0110
0.0089+j0.0826	0.3881-j0.6525	
1.5958	0.7460	
-0.8131+j1.0910	0.6079+j0.1366	
-0.8131-j1.0910	0.6079-j0.1366	

4.3.1 Realization of Digital Model

The transfer function of the digital filter is calculated as *H(z)*, and the structure of the filter must be realized with a block diagram. Realization with a block diagram is a signal flow diagram. It includes delays, additions, multiplications, and constant coefficients. The ordering of operations, scaling, and accuracy are ignored. The designed filter can be realized in many ways with differing properties. Some of the realization forms are direct form I and II, cascade, parallel, ladder, lattice, and multifeedback [58]. Direct form I is used to realize the *H(z)* transfer function.

The three basic types of elements for realization are unit delay, adder, and multiplier. Unit delay holds the input signal for a unit of time and delivers it to output. It is indicated with the delay operator "Z^{-1}" in *z*-domain. Adder adds two or more input signals, and multiplier multiplies a signal by a constant number.

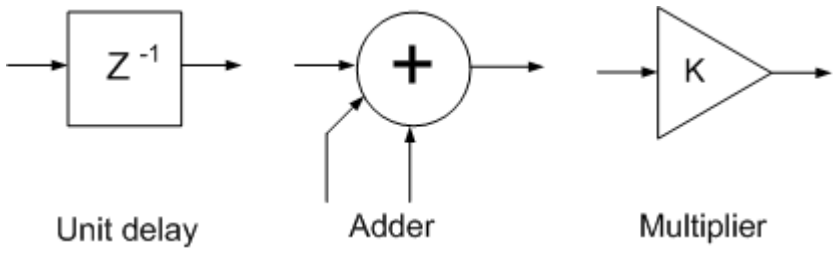

Fig. 4.20. Block diagram elements

The first step of realizing a digital filter is making the transfer function a difference equation. The transfer function is the ratio of the output z transform to the input z transform. The *H(z)* transfer function is divided by the highest order of z and rewritten as

$$\frac{Y(z)}{X(z)}=\frac{-0.01102+0.01763\,z^{-1}+0.0156\,z^{-2}-0.03298\,z^{-3}+0.01282\,z^{-4}+0.03276\,z^{-5}}{1-2.738\,z^{-1}+3.394\,z^{-2}-2.425\,z^{-3}+0.9712\,z^{-4}-0.1669\,z^{-5}} \tag{4.27}$$

Performing cross-multiplication yields

$$\begin{aligned}&X(z)(-0.01102+0.01763z^{-1}+0.0156z^{-2}-0.03298z^{-3}+0.01282z^{-4}\\&+0.03276z^{-5})=Y(z)(1-2.738z^{-1}+3.394z^{-2}-2.425z^{-3}\\&+0.9712z^{-4}-0.1669z^{-5})\end{aligned} \tag{4.28}$$

Taking the inverse transform yields

$$\begin{aligned}&-0.01102x[n]+0.01763x[n-1]+0.0156x[n-2]-0.03298x[n-3]\\&+0.01282x[n-4]+0.03276x[n-5]=y[n]-2.738y[n-1]+3.394y[n-2]\\&-2.425y[n-3]+0.9712y[n-4]-0.1669y[n-5]\end{aligned} \tag{4.29}$$

and finally, solving for $y[n]$ yields

$$\begin{aligned}&y[n]=-0.01102x[n]+0.01763x[n-1]+0.0156x[n-2]-0.03298x[n-3]\\&+0.01282x[n-4]+0.03276x[n-5]+2.738y[n-1]-3.394y[n-2]\\&+2.425y[n-3]-0.9712y[n-4]+0.1669y[n-5]\end{aligned} \tag{4.30}$$

Using the direct form I, the block diagram in Fig. 4.21 is built for the digital model. This block diagram is tested in Matlab Simulink and compared with the *H(z)* transfer function output. Block diagram output follows the transfer function output and the represents the transfer function successfully.

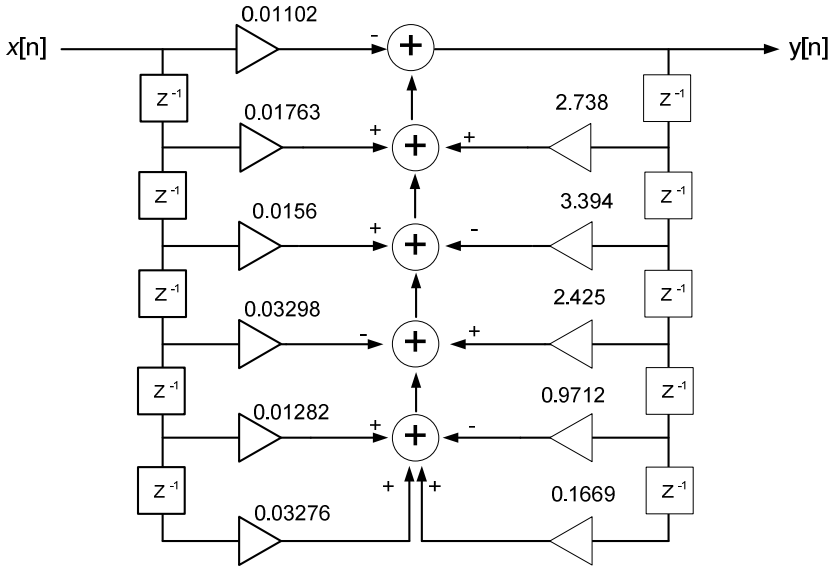

Fig. 4.21. Digital representation of OCT analog output

4.4 Complete Model for OCT Analog Output

As its name implies, optical CT optically measures the current signal by using a light beam. The output voltage of the transformer is generated by opto-electronics, which process the information coming from the light carried by fiber optic cable. Typically, OCTs consist of a light source, fiber optic cable, polarizer, modulator, and electronics. In order to model the optical part of the OCT, the optical elements and their transfer matrixes are used. The electronics of the transformers are modeled separately by using the frequency response characteristics of the transformers. The two models are combined and presented as the complete transformer model.

4.4.1 Optical Modeling

Jones Matrix Calculus is one of the well-known methods to describe the polarized light and its state in terms of amplitude and phase. Polarized light is represented by classical electric field components in terms of 2x1-column vector (Jones vector), and the linear polarizing elements are represented as 2x2 matrices (Jones matrices). The final state of the polarized light that travels through an optical element that has its own Jones matrix M is calculated by taking the product of the Jones vector of the incident light and the Jones matrix of the optical element [59]-[61]. Please note that the multiplication of the matrices has to be in the correct order.

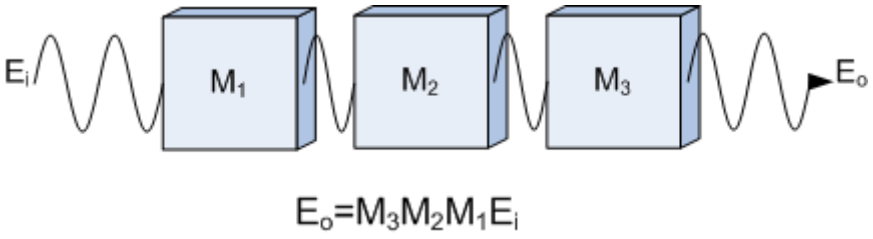

Fig. 4.22. Jones calculus method

4.4.2 Jones Vector

The incident light wave is represented by electric filed (or optical field) in terms of complex quantities. The components of a light propagating in z direction are

$$E_x(z,t) = E_{ox} e^{i(\omega t - kz + \delta_x)}$$
$$E_y(z,t) = E_{oy} e^{i(\omega t - kz + \delta_y)} \tag{4.31}$$

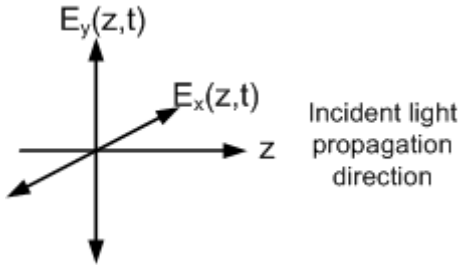

Fig. 4.23. Incident light and its representation

If the propagator (the phase of the light wave) "*wt-kz"* is suppressed, then (4.31) becomes

$$E_x = E_{ox}e^{i\delta_x}$$
$$E_y = E_{oy}e^{i\delta_y} \tag{4.32}$$

where E_{ox} and E_{oy} are the maximum amplitudes and δ_x and δ_y are the phases of each of the components. Equation (4.32) can be arranged in a 2x1-column matrix E as

$$E = \begin{pmatrix} E_x \\ E_y \end{pmatrix} = \begin{pmatrix} E_{0x}e^{i\delta_x} \\ E_{0y}e^{i\delta_y} \end{pmatrix} \tag{4.33}$$

It can be called the Jones vector. The maximum amplitudes, E_{0x} and E_{0y}, are real quantities. There are different Jones vectors for various states of polarized light, such as linear horizontally/vertically polarized light, linear 45 degree polarized light, and circularly polarized light. Horizontally and vertically linear as well as circularly polarized light are used for modeling purposes. The following are the Jones vectors for the polarized lights:

Linear, horizontally polarized (LHP): For this state E_y =0 and the Jones vector becomes

$$E_{LHP} = \begin{pmatrix} E_x \\ E_y \end{pmatrix} = \begin{pmatrix} E_{0x}e^{i\delta_x} \\ 0 \end{pmatrix} \tag{4.34}$$

The normalized Jones vector for LHP light is written as:

$$E_{LHP} = \begin{pmatrix} 1 \\ 0 \end{pmatrix} \tag{4.35}$$

Linear, vertically polarized (LVP): For this state E_x=0 and the Jones vector becomes

$$E_{LVP} = \begin{pmatrix} 0 \\ 1 \end{pmatrix} \tag{4.36}$$

Circularly polarized light: For this state $E_{0x}=E_{0y}$ and δy-δy=90 deg. for right circular and -90 deg. for left circular. Then $2E_{0x}^2=1$ and the Jones vector becomes

$$E_{RCP} = \frac{1}{\sqrt{2}}\begin{pmatrix} 1 \\ i \end{pmatrix} \text{for right circular and}$$

$$E_{LCP} = \frac{1}{\sqrt{2}}\begin{pmatrix} 1 \\ -i \end{pmatrix} \text{for left circular light} \tag{4.37}$$

4.4.3 Jones Matrices for the Polarizer, Waveplate, and Rotator

Jones matrices for optical elements are formed as 2x2 matrices in order to present the new state of the light with a 2x1 vector. The calculations and derivations of the Jones matrices for optical elements are very well presented in literature [59]-[61]. For modeling purposes, the polarizer, waveplate, Faraday and Pockels rotators, and mirror matrices are used as in Table 4-7.

Table 4-7
Jones matrices of optical elements

Optical Element	*Corresponding Jones matrix*
Linear horizontal polarizer(M_p^x)	$\begin{pmatrix} 1 & 0 \\ 0 & 0 \end{pmatrix}$
Linear vertical polarizer(M_p^y)	$\begin{pmatrix} 0 & 0 \\ 0 & 1 \end{pmatrix}$
Quarter wave plate (M_q^f),(M_F^b)	$\frac{1}{\sqrt{2}}\begin{pmatrix} 1 & -i \\ -i & 1 \end{pmatrix}, \frac{1}{\sqrt{2}}\begin{pmatrix} 1 & i \\ i & 1 \end{pmatrix}$
Mirror (M_m)	$\begin{pmatrix} -1 & 0 \\ 0 & 1 \end{pmatrix}$
Faraday rotator (M_F^f), (M_F^b)	$\begin{pmatrix} \cos(\theta) & -\sin(\theta) \\ \sin(\theta) & \cos(\theta) \end{pmatrix}\begin{pmatrix} \cos(\theta) & \sin(\theta) \\ -\sin(\theta) & \cos(\theta) \end{pmatrix}$
Pockel cell (M_P)	$\begin{pmatrix} \cos(\frac{\gamma}{2}) & i\sin(\frac{\gamma}{2}) \\ i\sin(\frac{\gamma}{2}) & \cos(\frac{\gamma}{2}) \end{pmatrix}$

4.4.4 Complete Optical Current Transformer Model

Literature shows many studies on modeling of optical parts of optical current transformers [62]-[64]. Since the operational principles of the systems are different, the developed models are various. Most studies use the Jones calculus method in order to model optical elements of the transformers and to improve the accuracy of the systems. However, they all focus on only the optical elements and without considering the electronic part of the OCTs. This section presents the complete model of the OCT that includes its electronic parts as well as its optical elements. The Jones calculus method presented in [62] is used to model the optical parts of the optical CT.

The optical block diagram of the NxtPhase optical CT is shown in Fig. 4.24. The operational principle of the OCT is given earlier in Chapter 2, section 2, and it is summarized here in order to remind readers and help them better understand the optics and optical elements of the OCT. The light from a light source, mainly light emitting diode (LED), enters an optical fiber polarizer. The light is polarized and then splits into two orthogonally polarized light waves in the polarizer. Light enters the sensing head that includes a quarter-wave plate, which converts the two linear orthogonal waves into circular waves right, and left-hand polarized light waves, respectively.

The two waves travel at different speeds through the sensing fiber. The difference in speeds is proportional to the strength of the magnetic field aligned with the sensing fiber. After completing their journey in the sensing region, the two waves reflect off a mirror. The reflection causes a swapping or reversal of circular polarization of the two waves, and the two waves then travel in the opposite direction with respect to the magnetic field. While traveling in the opposite direction, the two waves continue to maintain their velocity differences for the return trip through the sensing fiber.

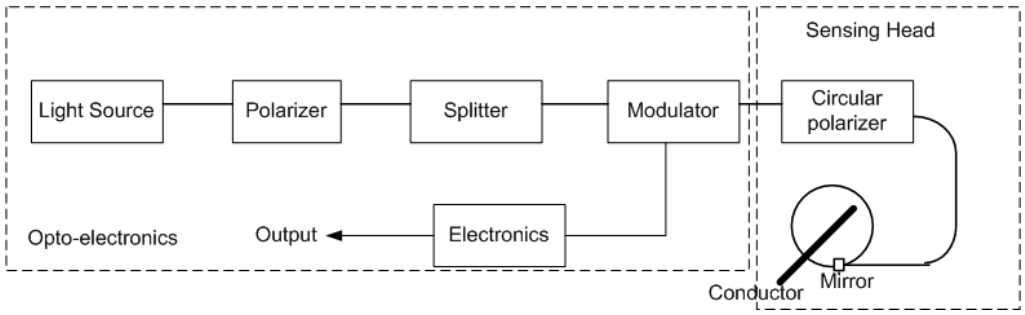

Fig. 4.24. Optical CT block diagram [38]

During their return journey, once the light has retraced its way through the sensing region, the two waves again encounter the quarter-wave plate that converts them back to linear polarization states. The change in the states of the two linearly polarized lights is compared, and the phase difference between them is measured. This difference is proportional to the current passing through the conductor due to the Faraday effect.

Considering the Jones matrices of the optical elements in OCT, the system transfer matrices that represent the final states of the two waves can be written as:

$$\begin{aligned} E_{y1} &= M_p^y M_q^b M_F^b M_m M_F^f M_q^f E_{xo} \\ E_{x1} &= M_p^x M_q^b M_F^b M_m M_F^f M_q^f E_{yo} \end{aligned} \tag{4.38}$$

where E_{xo} and E_{yo} are input lights and E_{y1} and E_{x1} are the final states of the return light Jones vectors. M_q^f and M_q^b are quarter wave (circular polarizer) matrices for forward and backward passes. An additional multiplication factor (phase shifter) of $e^{i(\pi/2)}$ is added to these matrices in order to make the calculations appropriate. M_m is the matrix for the mirror. M_F^f and M_F^b are Faraday rotator matrices for the forward and backward passes. M_p^x and M_p^y are the reduced polarizer matrices from 2x2 to 1x2 where the zeros are eliminated to make calculations appropriate. The matrices presented in Table 4-7 are used for the calculations, and the following calculations are performed.

$$E_{y1} = \begin{bmatrix} 0 & 1 \end{bmatrix} \frac{1}{\sqrt{2}} \begin{bmatrix} 1 & i \\ i & 1 \end{bmatrix} e^{i(\pi/2)} \begin{bmatrix} \cos(\theta) & \sin(\theta) \\ -\sin(\theta) & \cos(\theta) \end{bmatrix} \begin{bmatrix} -1 & 0 \\ 0 & 1 \end{bmatrix} \begin{bmatrix} \cos(\theta) & -\sin(\theta) \\ \sin(\theta) & \cos(\theta) \end{bmatrix} \frac{1}{\sqrt{2}} \begin{bmatrix} 1 & -i \\ -i & 1 \end{bmatrix} e^{i(\pi/2)} \begin{bmatrix} 1 \\ 0 \end{bmatrix}$$

$$E_{x1} = \begin{bmatrix} 1 & 0 \end{bmatrix} \frac{1}{\sqrt{2}} \begin{bmatrix} 1 & i \\ i & 1 \end{bmatrix} e^{i(\pi/2)} \begin{bmatrix} \cos(\theta) & \sin(\theta) \\ -\sin(\theta) & \cos(\theta) \end{bmatrix} \begin{bmatrix} -1 & 0 \\ 0 & 1 \end{bmatrix} \begin{bmatrix} \cos(\theta) & -\sin(\theta) \\ \sin(\theta) & \cos(\theta) \end{bmatrix} \frac{1}{\sqrt{2}} \begin{bmatrix} 1 & -i \\ -i & 1 \end{bmatrix} e^{i(\pi/2)} \begin{bmatrix} 0 \\ 1 \end{bmatrix} \tag{4.39}$$

Faraday rotator matrices M_F^f and M_F^b include a θ rotation angle, which is the amount of rotation of the light in the presence of magnetic field, and can be represented as

$$\theta = VNI \tag{4.40}$$

where *V* is the Verdet constant of the fiber, *N* is the number of fiber turns, and *I* is the current passing through the current carrying conductor.

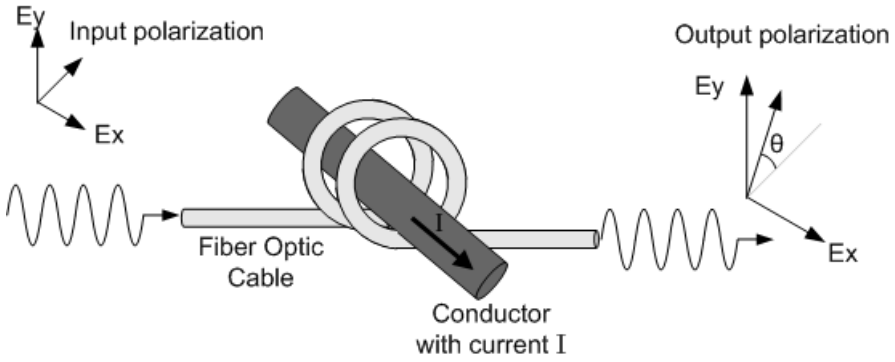

Fig. 4.25. Faraday effect [65]

The resulting states of the light, E_{y1} and E_{x1}, are calculated as complex numbers. The resulting phase shift between the two waves is the angle between the two complex numbers, and it is four times bigger than the single θ Faraday rotation [62], [66].

$$\phi = \angle E_{y1} - \angle E_{x1} \tag{4.41}$$

A Matlab program calculates the final states of the light waves and finds the final phase shift between them according to the input current. This program is integrated with Matlab Simulink and shown in Fig. 4.26. The program is given in Appendix B.

The model output (phase shift in degrees) is compared with the input signal (current in Amperes). Results show that the output signal is proportional with the input current signal and has the same characteristics. Fig. 4.27 shows the comparison. Results show that the output signal represents the current signal with different amplitude. The phase shift is normalized with the input current in order to make calculations properly. The input current and the normalized output phase shift are plotted together, and it is seen that they are overlapping. For this reason, this normalized output represents the input signal, and it can be used as an input for the electronics of the system. Since it is difficult to see the difference between the normalized output signal and the input current, it is not shown in a figure.

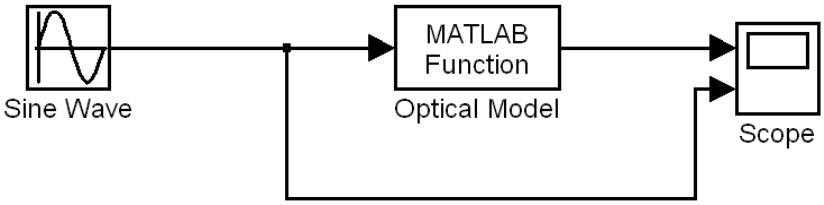

Fig. 4.26. Matlab simulation of optical model

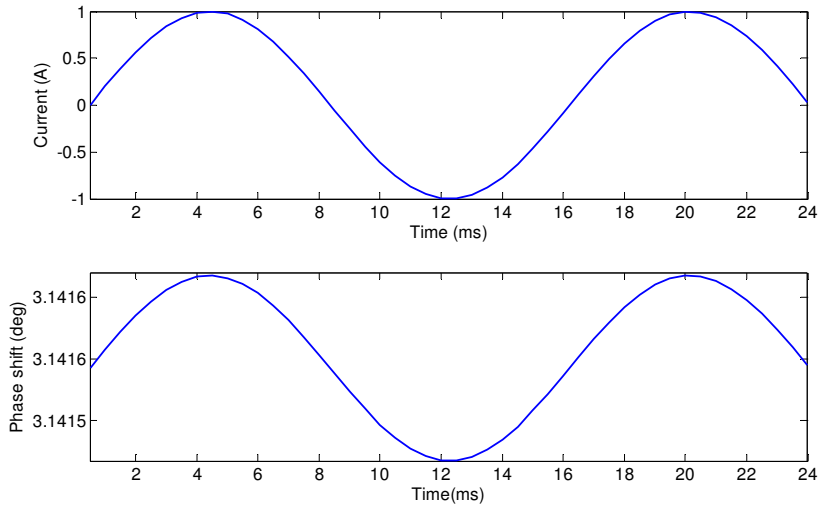

Fig. 4.27. Final phase shift variation by input current

Frequency characteristics of the optical CT were obtained and presented earlier. Since the optical part of the system is independent from the frequency [67], the obtained characteristics belong to electronics of the system. The electronics include a signal-processing unit that processes the information coming from the optical parts and generates output through filter circuits. The obtained frequency characteristic has a similar filter characteristic; therefore, it is used to model the electronics of the system. The transfer function estimated earlier (which can be in *s*-domain or *z*-domain) represents the electronics characteristics and are combined here with the optical model. Fig. 4.28 shows the complete developed model and its implementation in circuit simulation. The current in the circuit is sensed through the optical model, and the electronics generate an output signal that is compared with the input current signal. Fig. 4.29 shows the comparison. Results show that the optical CT model reproduces the input current successfully.

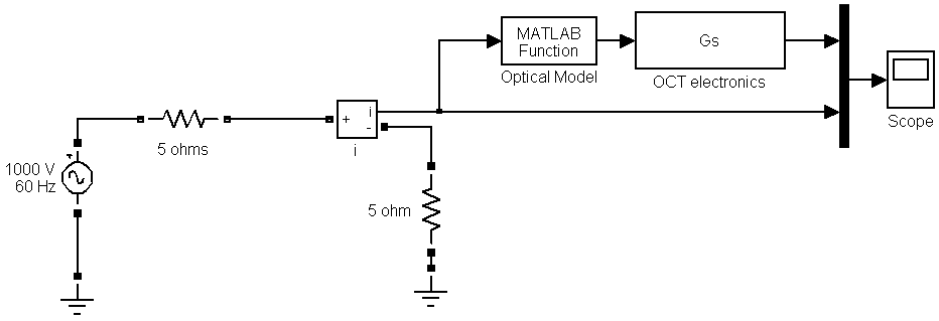

Fig. 4.28. Complete model and its implementation

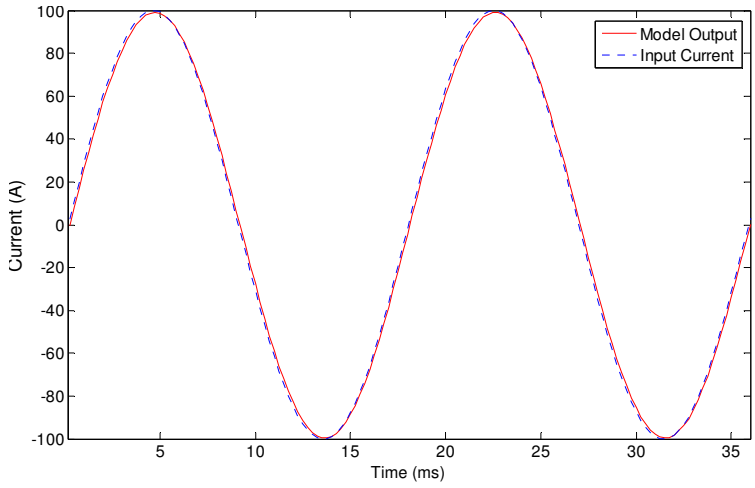

Fig. 4.29. Comparison of input current and model output

The complete model frequency response characteristics are compared with the experimental data. Same experimental frequencies are applied to the model and the magnitude and phase responses are obtained. Fig. 4.31 shows the comparison between experimental data and complete model outputs. 0.88% maximum difference is calculated in magnitude and 2.41 % maximum difference is calculated in phase.

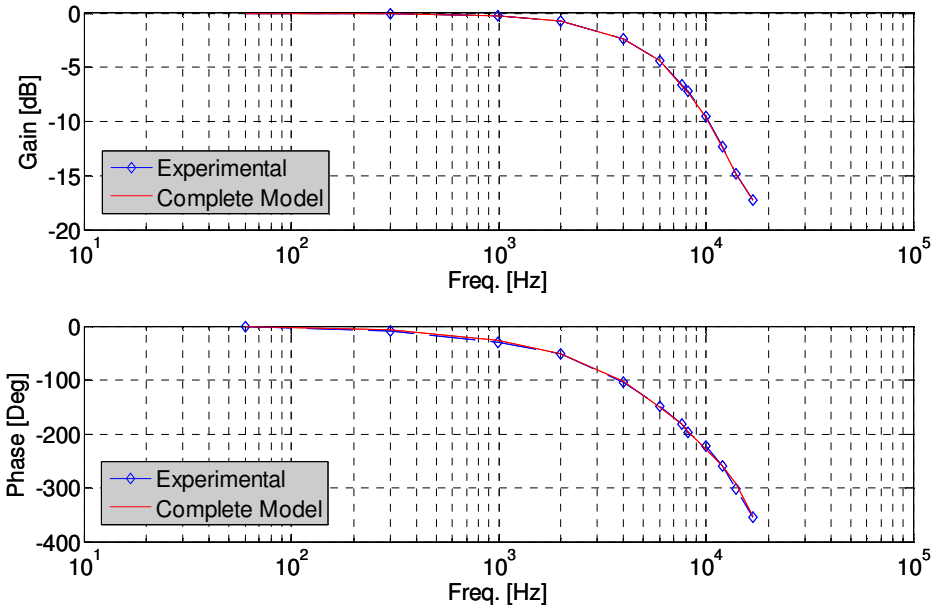

Fig. 4.30. Comparison of frequency characteristics of experimental data and complete model output

4.5 Analog Model for OVT Analog Output

The model for the optical VT is developed using the same method presented for the optical CT model development. The transformer is considered a black box, and a transfer function is approximated from the experimental frequency response. An analog circuit is developed from the developed transfer function. Digital representation of the analog output is developed from a *z*-domain transfer function. Finally, the complete model is presented using the Jones calculus method for optical elements and the developed transfer function for electronics.

4.5.1 Measurement of OVT Frequency Characteristics

According to the manufacturer's data and the literature review, the optical potential transformer used in the laboratory has a better frequency response than a magnetic VT. One of the out-

puts has the bandwidth of 0.001 Hz to 40 kHz, and the other output has 20 Hz to 5 kHz. In order to verify the specifications, the frequency response of the OVT is measured. The output of the OVT that has the frequency range of 20 Hz to 5 kHz is tested and a signal up to 14 kHz is applied. Results are given and used for model development. The following is a description of the test setup.

The OVT is supplied with variable-frequency voltage. The applied voltage and OVT output voltages are measured and recorded in order to make a comparison of the frequency response of the OVT. The test setup can be seen in Fig. 4.31.

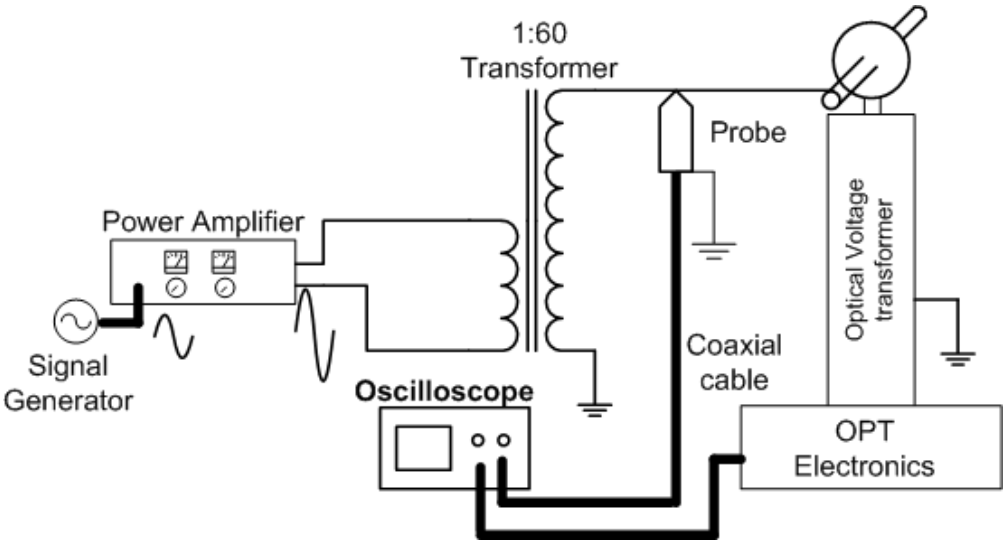

Fig. 4.31. OVT frequency response test setup

A signal generator, up to 1 MHz frequency, is used as a signal source. The variable-frequency output voltage of the signal generator is amplified by a 1,000 W power amplifier. The power amplifier is set to mono-mode and supplies a 1:60 ratio of voltage transformer. The secondary side of the transformer is connected to the OVT. The power amplifier drives around a 35 V signal through the transformer; this corresponds to 35x60=2,100 V applied to the OVT.

The frequency of the applied voltage varies between 60 Hz~14 kHz. The applied voltage is measured with a 1,000:1 high voltage oscilloscope probe at the secondary side of the 1:60 transformer. The probe is connected to the digital oscilloscope as channel 2. The other channel, input 1, is used to measure the output voltage of the OVT. Fig. 4.32 shows the scope recorded FR test data for an applied voltage and the OVT output voltage at 3 kHz frequency. The phase difference is

calculated by measuring the zero crossing points of the two sine waves with scope feature. The accuracy of the probe and oscilloscope is less than 2%.

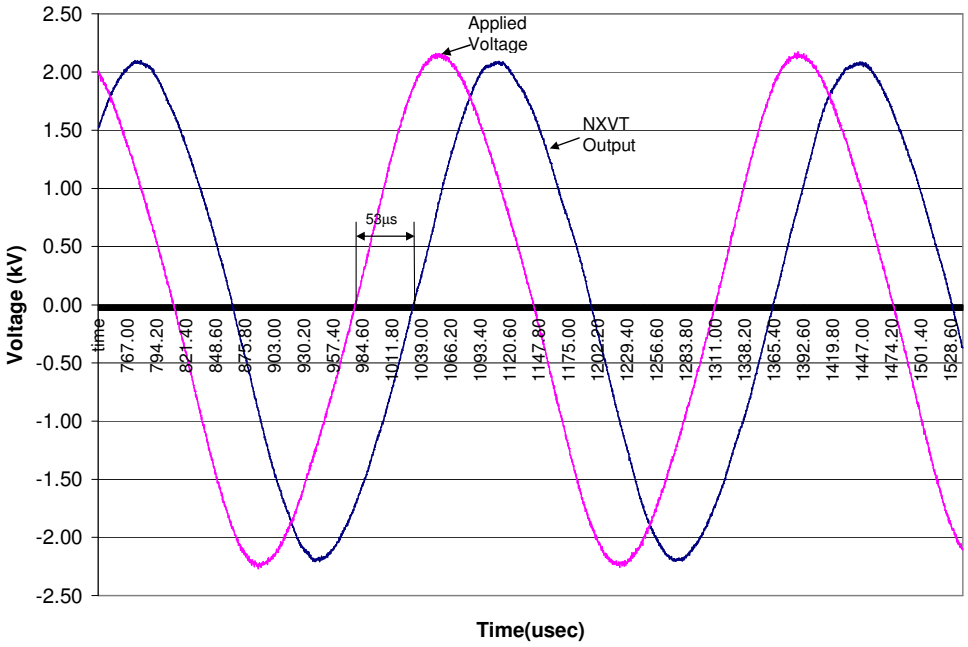

Fig. 4.32. Applied voltage and OVT output voltage at 3 kHz

The applied voltage is not kept constant while the frequency is varied in sixteen steps from 60 Hz to 14 kHz. The waveforms of both signals are recorded simultaneously. The rms values are manually recorded using the digital oscilloscope. The phase difference corresponding to the time difference between the zero crossings of the signals is determined and converted to degrees using a feature of the digital oscilloscope. Fig. 4.32 shows the signals at 3 kHz and demonstrates the method used for phase angle calculation. A digital oscilloscope noise filter is used during this measurement in order to reduce the noise of the signals. Table 4-8 shows the results of the measurements and calculated phase differences.

The time difference is measured as 53 µs from Fig. 4.32, and it shows that the OVT output is lagging. The phase angle algorithm and calculation are shown in (4.42).

$$Phase.lag[\text{deg}] = \frac{Time.lag[\text{sec}] \times 360}{\frac{1}{f[Hz]}} = \frac{53 \times 10^{-6} \times 360}{\frac{1}{3000}} \cong 57° \tag{4.42}$$

Fig. 4.33 shows that the amplitude gradually decreases as frequency increases after frequency of 3 kHz. Between DC and 3 kHz, the amplitude and phase angle are more or less independent from the frequency. Fig. 4.33 shows the frequency response characteristics. This corresponds to the OVT manufacturer's claim that the delay caused by the optical system is constant and independent from the frequency up to 5 kHz.

Table 4-8
Frequency characteristics of OVT test results

Freq (Hz)	*OVT (kV)*	*Applied Voltage (kV)*	*Normalized Amplitude*	*Phase (deg)*
60	2.038	2.011	1.000	-0.495
500	2.097	2.076	0.997	-10.62
1000	2.116	2.101	0.994	-19.13
2000	2.177	2.157	0.996	-38.49
3000	2.297	2.321	0.977	-58.05
4000	2.485	2.592	0.946	-76.96
5000	2.819	3.049	0.912	-96.35
6000	3.478	3.893	0.881	-114.7
7000	4.981	5.76	0.853	-132.5
8000	7.812	9.31	0.828	-149.1
9000	8.274	10.09	0.809	-166.4
9743	6.495	8.08	0.793	-179.9
11000	3.204	4.081	0.775	-200.1
12000	2.339	3.112	0.742	-217.3
13000	1.624	2.178	0.736	-233.9
14000	1.071	1.441	0.733	-252.1

The test is repeated by keeping the applied voltage constant while the frequency is varied in sixteen steps from 60 Hz to 14 kHz. The same testing procedure is applied, and it can be seen that amplitude-frequency and phase-frequency relations are similar to each other. The first method generated a higher voltage than the second method. The maximum generated voltage is 10 kV in method 1 and only 1.5 kV in the second method. The comparison of the results shows that the voltage does not have a significant effect on the frequency characteristics of the OVT.

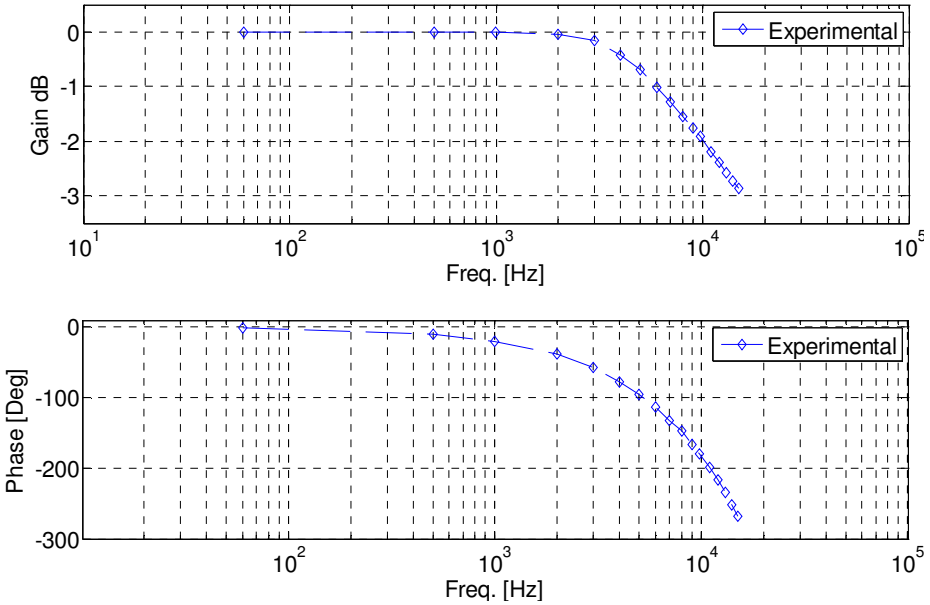

Fig. 4.33. Amplitude-frequency and phase angle-frequency characteristics of OVT

4.5.2 Developments of a Transfer Function using the Measured Frequency Spectrum

The same method used for OCT transfer function approximation is implied for the OVT circuit development. The frequency response data for each frequency value given in Table 4-8 show amplitude and phase responses in polar form. Using the frequency response data, numerator and denominator coefficients "b" and "a" of the transfer function *H(s)* are approximated by selecting different numbers of orders. The optimum number of order is found as 4 for numerator and 5 for denominator. Selecting the order of numerator and denominator as 4 and 5, and the iteration number 50, a transfer function for OVT is approximated as

$$H(s)=\frac{-4.141.10^{5}s^{4}+7.866.10^{10}s^{3}-7.911.10^{15}s^{2}+2.289.10^{20}s+8.875.10^{24}}{s^{5}+1.012.10^{6}s^{4}+1.641.0^{11}s^{3}+1.705.10^{16}s^{2}+7.006.10^{20}s+8.863.10^{24}} \qquad (4.43)$$

Fig. 4.34 shows Bode plot comparison of approximated transfer function and experimental frequency response data. The maximum differences are calculated as 1.52% in amplitude and 0.38% in phase. This plotted transfer function provides the frequency response of OVT for frequencies up to 14 kHz.

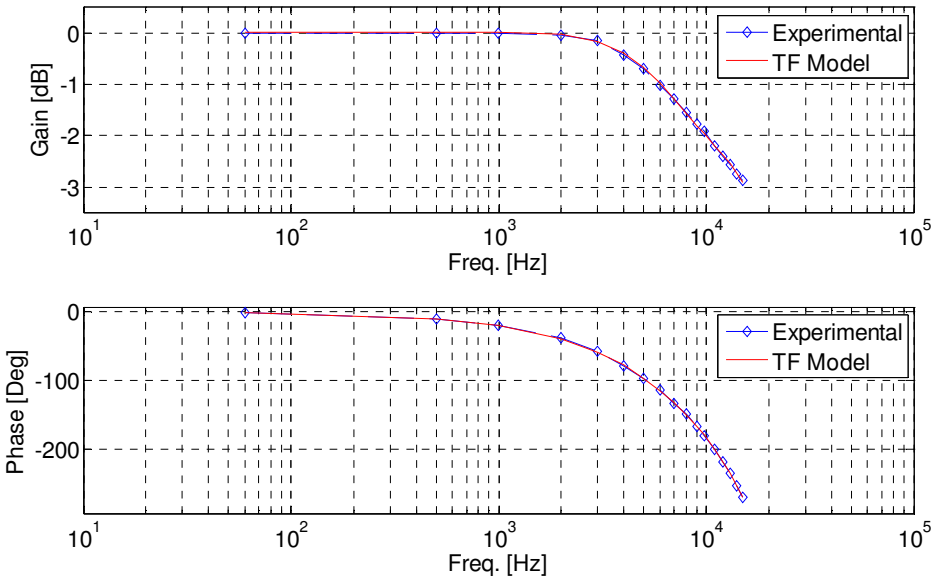

Fig. 4.34. Comparison of frequency responses of model and experimental results

4.5.3 Reconstruction of the Developed Transfer Function as a Sum of First Order Rational Functions and Their Circuit Implementations

The same method used for the developed OCT circuit models is used to develop the OVT circuit model. The approximated OVT transfer function is written in terms of rational functions using the real poles and complex conjugate poles. The transfer function has one real pole and two complex conjugate pole pairs as shown in Table 4-9. The reformed transfer function is as follows:

$$H(s)=\underbrace{\underbrace{\frac{(0.3672+j1.2814)\times10^5}{s-(-0.5503+j0.9237)\times10^5}+\frac{(0.3672-j1.2814)\times10^5}{s-(-0.5503-j0.9237)\times10^5}}_{\text{Complex conjugate pole pair}}+\frac{(-6.3306)\times10^5}{s-(-8.3906)\times10^5}+\frac{(1.6167)\times10^5}{s-(-0.3902)\times10^5}+\frac{(-0.1614)\times10^5}{s-(-0.2342)\times10^5}}_{\text{Real poles}} \tag{4.44}$$

Table 4-9
Poles and zeros of transfer function

Residues $[c_n]$ $(x10^5)$	*Poles* $[a_n]$ $(x10^5)$
0.3672+j1.2814	-0.5503+j0.9237
0.3672-j1.2814	-0.5503-j0.9237
-6.3306	-8.3906
1.6167	-0.3902
-0.1614	-0.2342

The real pole and complex conjugate pairs are implemented by using the method described in the OCT circuit development part. The real pole is implemented as RL, and complex poles are implemented as RLC circuits. The G multiplication factors are represented as VCVS where the ratios are the G values. Some of the G values are minus and are represented by changing the gain VCVS. The developed circuits are interconnected in parallel and form the final circuit model of OVT. Table 4-10 shows the circuit element values and VCVS gains. The program used for the calculations is presented in Appendix A

Table 4-10
Circuit parameters

L *(μH)*	*C* *(μF)*	*G*
L1=1.1918	C1=9.5211	G1= -0.7545
L2=25.627	C2=9.0857	G2= 4.1431
L3=42.705		G3= -0.6981
L4=9.5211		G4= 0.6673
L5=9.0857		G5= -1.6981

4.5.4 Validation of the Developed Equivalent Circuits

In order to validate the developed models, two types of comparisons are performed for transfer functions and circuit models. Both model outputs are compared with experimental test data. Results are presented in the same plots and the errors are given based on the experimental data. The types of comparisons are

1. Comparison of frequency response characteristics of transfer function and circuit models with experimental frequency response test results.

2. Transfer function and electrical circuit models supplied with an experimental impulse test signal, as presented in Chapter 3.

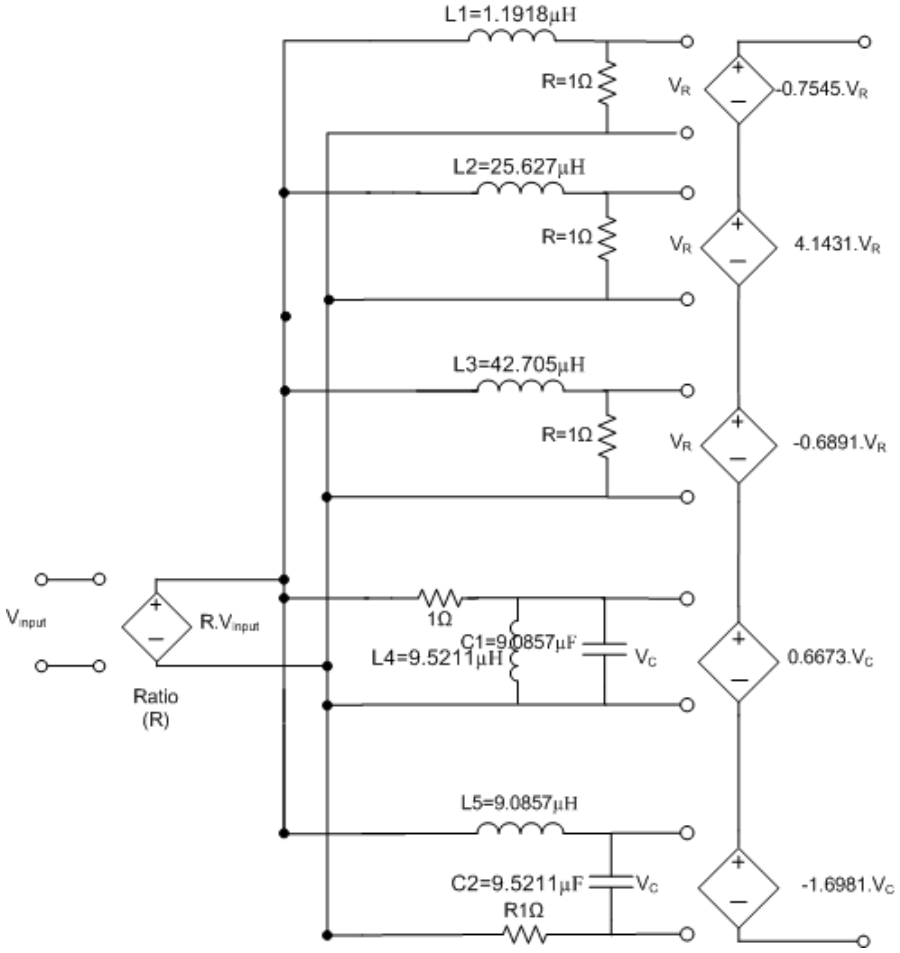

Fig. 4.35. OVT equivalent circuit model

Fig. 4.36 shows the frequency response comparison. It is seen that both the transfer function and circuit models follow the experimental test results. The errors are given in Table 4-11 in percentages based on the experimental results. The results are within the desired range and show that the models can represent the OVT in simulation studies.

Table 4-11
Errors between models and experimental results

Errors	*Amplitude*	*Phase*
Transfer function	1.52%	0.38%
Circuit Model	1.43%	0.79%

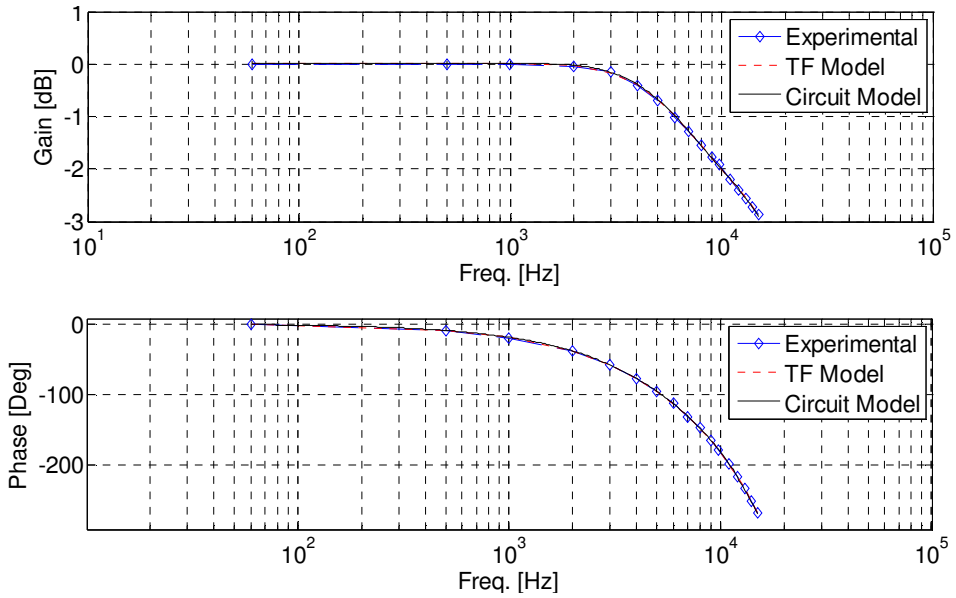

Fig. 4.36. Frequency response comparison of developed models

Fig. 4.37 shows the second comparison method result. An impulse signal is applied to OVT, and the output and input signals are recorded as presented in Chapter 3. The same signal is applied to the approximated transfer function. The *H(s)* transfer function is converted to *H(z)* discrete time transfer function, and the input signal is applied. The output of the *H(z)* transfer function is recorded. The same input signal is applied to the circuit model in PSpice simulation. The circuit output is recorded and plotted together with the experimental output and transfer function output. In Fig. 4.37, the model output tracks the experimental output. The transfer function output and the circuit model output are very close to each other. This shows that the developed circuit model from the transfer function is successful. Based on the experimental output signal, the maximum error for both models is 20%. Due to the noisy experimental test data, high errors observed in the simulations.

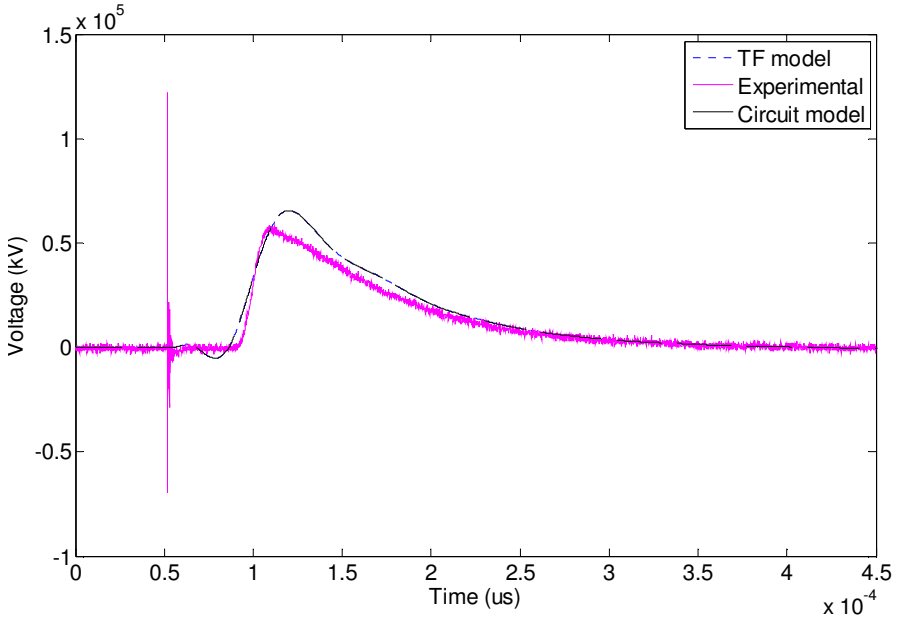

Fig. 4.37. Comparison of model output signals with experimental output signal

4.6 Digital Model for OVT Output

The bilinear method described in OCT digital model development part is used to represent the analog output of the optical VT in *z*-domain. Using the Matlab® "c2d" command, a new *H(z)* transfer function is developed. "Tustin" is used as a calculation method with a sampling time of 7.82 µsec. The frequency response of the *H(s)* and *H(z)* are compared with experimental data and shown in Fig. 4.38. It is seen that the two responses match and follow each other successfully. The residues and poles of the *H(z)* transfer function are calculated and presented in Table 4-12. By looking at the poles and zeros and the z-map of the transfer function, it is seen that all the poles are inside the unit circle and the system is stable. The transformed transfer function is

$$H(z)=\frac{-0.09573z^5+0.3912z^4-0.5213z^3+0.009585z^2+0.6319z-0.3858}{z^5-2.061z^4+1.304z^3+0.07308z^2-0.4377z+0.1515} \tag{4.45}$$

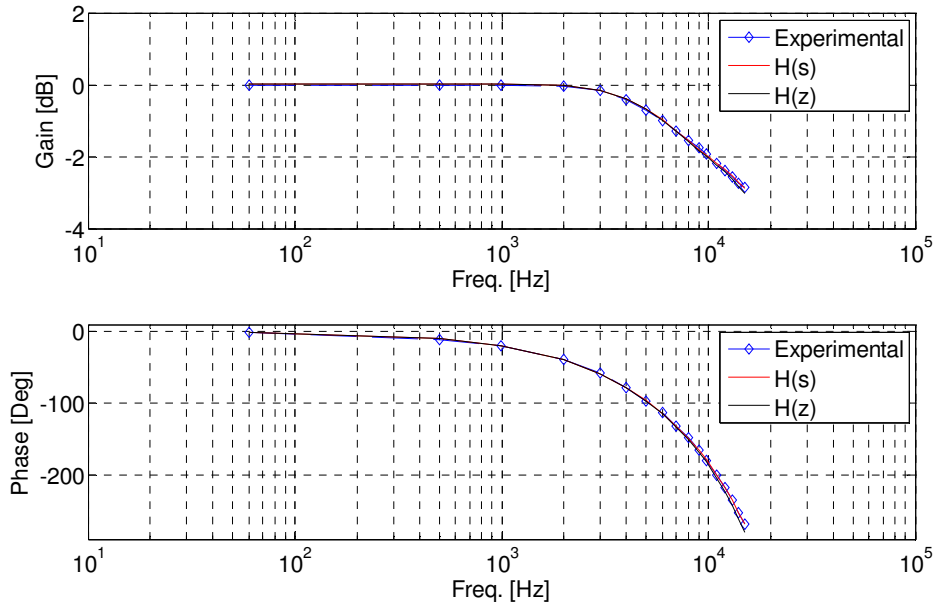

Fig. 4.38. Comparison of *H(s)* and *H(z)* frequency responses

Table 4-12
Errors between models and experimental results

Residues	*Poles*	*Constant*
-0.1058	0.8324	-0.0957
0.9510	0.7355	
-0.1905+j0.6197	0.5127+j0.4492	
-0.1905-j0.6197	0.5127-j0.4492	
-0.2703	-0.5324	

4.6.1 Realization of the Developed Digital Model

Direct form II is used to realize the *H(z)* transfer function of OVT analog output. The first step of realizing the filter is making the transfer function into a difference equation. The transfer function is the ratio of the output z transform to the input z transform. The *H(z)* transfer function is divided by the highest order of z and rewritten as

$$\frac{Y(z)}{X(z)} = \frac{-0.09573 + 0.3912z^{-1} - 0.5213z^{-2} + 0.009585z^{-3} + 0.6319z^{-4} - 0.3858z^{-5}}{1 - 2.061z^{-1} + 1.304z^{-2} + 0.07308z^{-3} - 0.4377z^{-4} + 0.1515z^{-5}} \tag{4.46}$$

then perform cross-multiplication yields

$$X(z)(-0.09573+0.3912z^{-1}-0.5213z^{-2}+0.009585z^{-3}+0.6319z^{-4}-0.3858z^{-5})=$$
$$Y(z)(1-2.061z^{-1}+1.304z^{-2}+0.07308z^{-3}-0.4377z^{-4}+0.1515z^{-5}) \quad (4.47)$$

Taking the inverse transform yields

$$\begin{aligned}&-0.09573x[n]+0.3912x[n-1]-0.5213x[n-2]+0.009585x[n-3]+0.6319x[n-4]\\&-0.3858x[n-5]=y[n]-2.061y[n-1]+1.304y[n-2]+0.07308y[n-3]\\&-0.4377y[n-4]+0.1515y[n-5]\end{aligned} \quad (4.48)$$

and finally, by solving for y[n]

$$\begin{aligned}y[n]=&-0.09573x[n]+0.3912x[n-1]-0.5213x[n-2]+0.009585x[n-3]\\&+0.6319x[n-4]-0.3858x[n-5]+2.061y[n-1]-1.304y[n-2]-0.07308y[n-3]\\&+0.4377y[n-4]-0.1515y[n-5]\end{aligned} \quad (4.49)$$

Using the direct form II, the block diagram in Fig. 4.39 is built for the digital model. This block diagram is tested in Matlab Simulink and compared with the *H(z)* transfer function output. Block diagram follows the transfer function output and the represents the transfer function successfully.

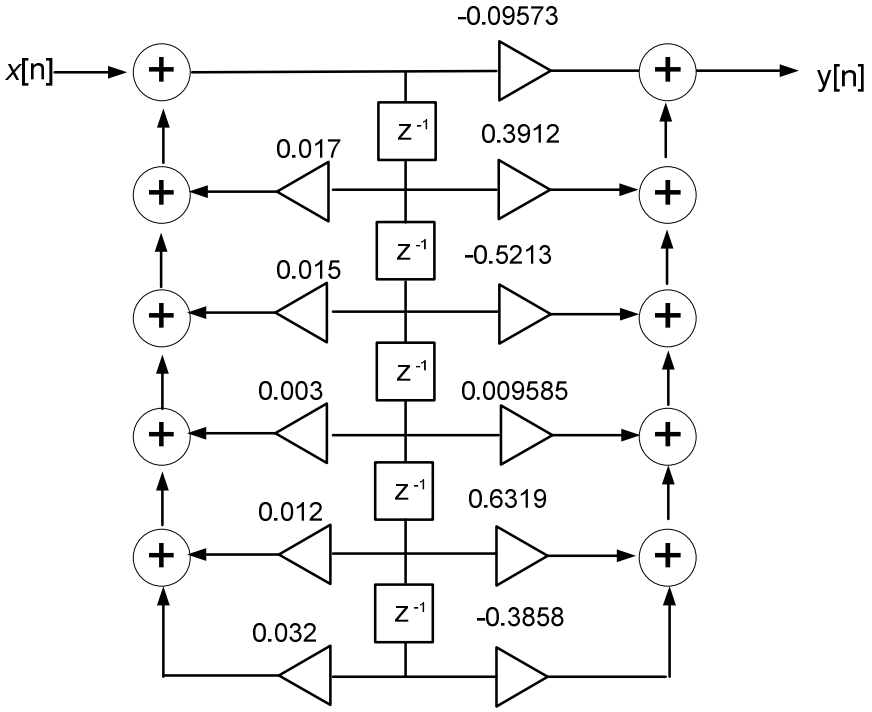

Fig. 4.39. Digital representation of analog output

4.7 Complete Model for OVT Analog Output

As presented earlier in Chapter 3, three Pockels cell-based sensors are placed in the inner tube of the optical voltage transformer (OVT). Two electrodes are placed at the ends of this structure: a high voltage electrode at the top (connected to the line) and a ground electrode at the bottom [32], [36]. The voltage on the line creates an electric field between the line and the ground [41]. This field is used by Pockels cells-based sensors to measure the voltage using the quadratic method as presented in [42] as follows:

$$V = -\sum_{i=1}^{N} \alpha_i E_x(x_i) \tag{4.50}$$

where E_x represents the electric field, which depends upon the sensor location, and α_i represents weights.

The light signal from a light emitting diode is sent from the NxtPhase opto-electronics through the fiber optic cable and travels up the unit's column. Light enters Pockels cells that are strategically located between the two electrodes. While light passes through the sensors, the electric field, created by line-to-ground voltage, changes the polarization of the light from circular to elliptical that is rotated 45 deg. These changes at the three sensors are collected and processed by electronics to calculate the line-to-ground voltage of the line [32], [43]. Detected sensor signals are connected to opto-electronics in the control room through a fiber optic cable. These signals are processed, and analog and digital outputs are generated as a NXVT output signal [32].

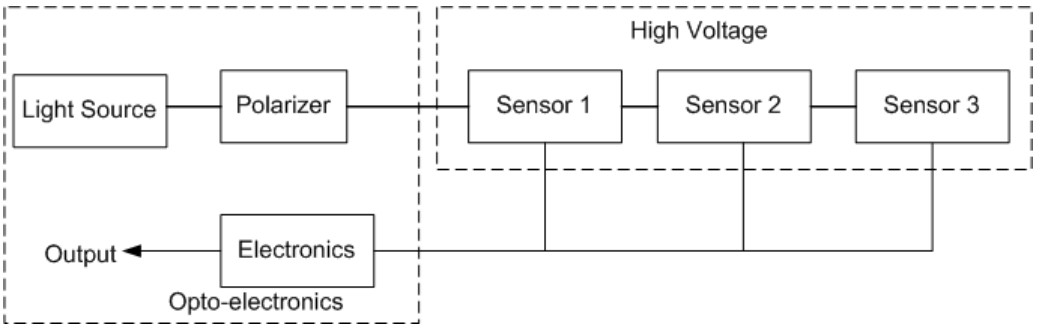

Fig. 4.40. Optical VT block diagram

4.7.1 Optical Modeling

The model for optical VT is developed in the same way as the method used for developing the OCT model. The optical elements, polarizer, and three Pockels cells are modeled using the Jones calculus method. A Pockels cell can be considered as a rotator, and the Jones matrix of 45 degree-rotated Pockels cell can be derived as in [59]

$$\begin{pmatrix} \cos(\frac{\gamma}{2}) & i\sin(\frac{\gamma}{2}) \\ i\sin(\frac{\gamma}{2}) & \cos(\frac{\gamma}{2}) \end{pmatrix} \tag{4.51}$$

where the γ is the rotation angle of the wave after passing the Pockels cell and is represented as

$$\gamma = \frac{2\pi n_0^3 r_{22} V}{\lambda_0} = \pi \frac{V}{V_\pi} \tag{4.52}$$

where

n_0^3: refractive index

r_{22}: electro-optic coefficient

V : electric field/voltage

V_π: half-wave electric field/voltage

λ_0: free space optical wavelength

The half-wave voltage is presented in [68] as 240 V. The voltage V is calculated as the voltage across the crystals. The locations of the crystals in the inner tube are given in [34], and the voltages that the crystals are subject to are calculated according to their locations and used as the weighting factor. The phase rotation angle of the γ is in radian and should be < 0.1 radian. In order to increase the sensor sensitivity, a constant is chosen properly as a multiplication factor [68]. For simulations, 10^{-4} is used as a constant.

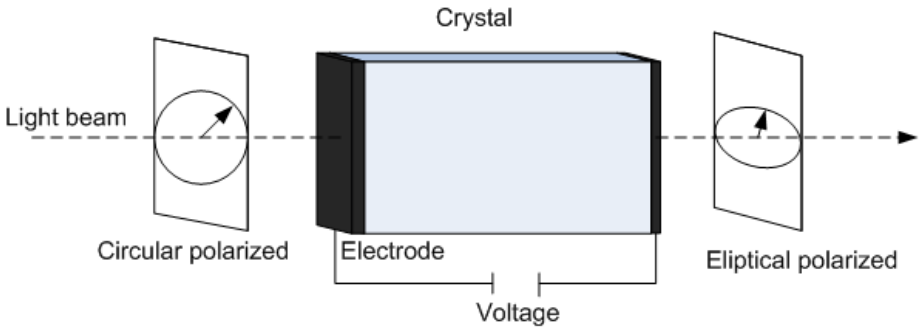

Fig. 4.41. Pockels effect

4.7.2 Complete Optical Voltage Transformer Model

Based on the operational principle of the voltage transformer, the sensor output states are calculated using the Jones matrixes of the optical elements as follows:

$$\begin{aligned} E_1 &= M_{pockel1} E_c \\ E_2 &= M_{pockel2} E_c \\ E_3 &= M_{pockel3} E_c \end{aligned} \tag{4.53}$$

where E_1, E_2, and E_3 are the final states of each sensor's output, E_c is circular polarized light vector, and $M_{pockel1}, M_{pockel2}$ and $M_{pockel3}$ are the Pockels matrixes of each crystal that depend upon the voltage across each crystal. The matrices presented in Table 4-7 are used for the calculations, and the following calculations are performed

$$\begin{aligned} E_1 &= \begin{pmatrix} \cos(\frac{\gamma_1}{2}) & i\sin(\frac{\gamma_1}{2}) \\ i\sin(\frac{\gamma_1}{2}) & \cos(\frac{\gamma_1}{2}) \end{pmatrix} \frac{1}{\sqrt{2}} \begin{bmatrix} 1 \\ i \end{bmatrix} \\ E_2 &= \begin{pmatrix} \cos(\frac{\gamma_2}{2}) & i\sin(\frac{\gamma_2}{2}) \\ i\sin(\frac{\gamma_2}{2}) & \cos(\frac{\gamma_2}{2}) \end{pmatrix} \frac{1}{\sqrt{2}} \begin{bmatrix} 1 \\ i \end{bmatrix} \\ E_3 &= \begin{pmatrix} \cos(\frac{\gamma_3}{2}) & i\sin(\frac{\gamma_3}{2}) \\ i\sin(\frac{\gamma_3}{2}) & \cos(\frac{\gamma_3}{2}) \end{pmatrix} \frac{1}{\sqrt{2}} \begin{bmatrix} 1 \\ i \end{bmatrix} \end{aligned} \tag{4.54}$$

The resulting states of the light are analyzed by calculating the intensity of light. The Wollaston principle is used to simulate photo detectors, the x, y components of the light are extracted, and the Hermitian calculation is performed in (4.55).

According to the quadratic method used for voltage calculation, the total intensity of the light can be presented as the minus of summation of the three intensities. A Matlab program calculates the final intensity according to the input voltage. This program is integrated with Matlab Simulink and shown in Fig. 4.42. The program is given in Appendix D.

$$I_1 = \frac{(E_{1ox}^{+} E_{1ox}) - (E_{1oy}^{+} E_{1oy})}{(E_{1ox}^{+} E_{1ox}) + (E_{1oy}^{+} E_{1oy})}$$

$$I_2 = \frac{(E_{2ox}^{+} E_{2ox}) - (E_{2oy}^{+} E_{2oy})}{(E_{2ox}^{+} E_{2ox}) + (E_{2oy}^{+} E_{2oy})}$$

$$I_3 = \frac{(E_{3ox}^{+} E_{3ox}) - (E_{3oy}^{+} E_{3oy})}{(E_{3ox}^{+} E_{3ox}) + (E_{3oy}^{+} E_{3oy})} \tag{4.55}$$

$$I_T = -(I_1 + I_2 + I_3) \tag{4.56}$$

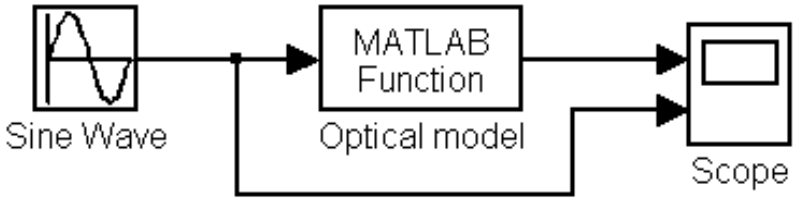

Fig. 4.42. Matlab simulation of optical model

The model output is compared with the input signal (voltage). Results show that the output signal is proportional with the input voltage signal and has the same characteristics. The output signal represents the voltage signal with different amplitude. The model output is normalized with the input voltage in order to make calculations properly. The input voltage and the normalized model output phase are plotted together, and it is seen that they are overlapping. For this reason,

this normalized output represents the input signal, and it can be used as an input for the electronics of the system. Fig. 4.45 shows the normalized output with input voltage, and it can be seen that difference between the normalized output signal and the input voltage match properly.

The complete model is developed the same way the optical CT complete model was developed. The complete model includes the optical model part, and the electronic frequency characteristics of the optical VT are obtained, and those presented earlier are used as the characteristic of the optical VT. Fig. 4.43 shows the complete model and its implementation in Matlab. The model tested in Matlab and results are compared with experimental frequency response data. The final model output shows that the optical VT model reproduces the input current successfully. 2.45 % error in amplitude and 2.47 % error in phase are calculated between the model output and experimental values.

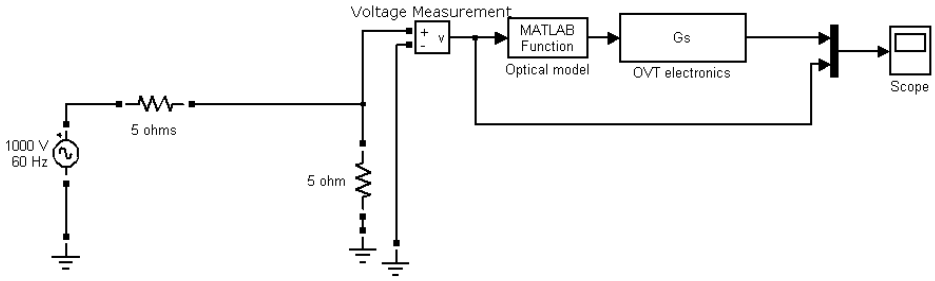

Fig. 4.43. Complete model for OVT

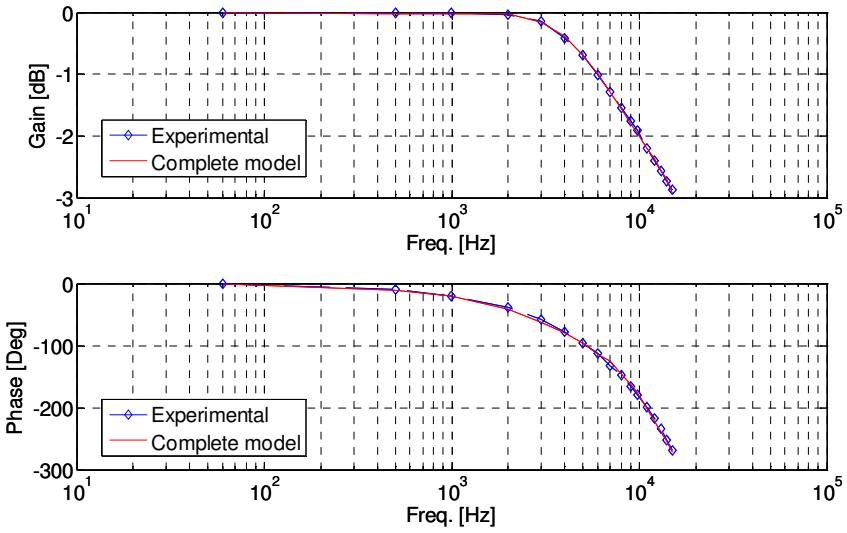

Fig. 4.44. Complete model and experimental frequency response comparison

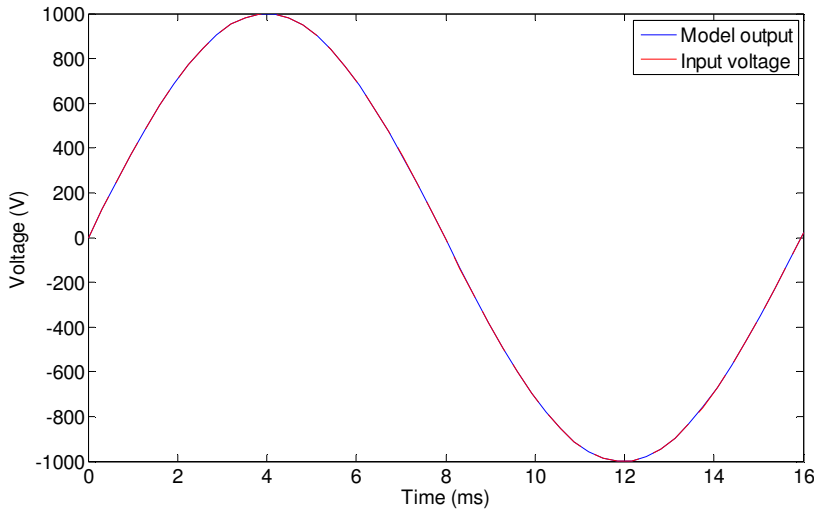

Fig. 4.45. Model and input voltage comparison

4.8 Conclusion

In this chapter, a methodology for developing different models for optical instrument transformer analog output is presented. Three types of models are presented: an analog circuit model, digital model, and complete model. For the analog model, transformers are considered as a black box, and frequency response characteristics of the transformers are obtained experimentally. Transfer functions for the systems are approximated from the frequency response data using a complex curve fitting method. Developed transfer functions and experimental results are compared and found to have 0.41% error for OCT and 1.52% error for OVT. Using the rational function representation of transfer functions, transfer functions are divided into complex conjugate poles and real poles. For each pole, RLC circuit elements are selected, and the final circuit model is developed by connecting them in parallel. The developed models are tested with a PSpice simulation program.

Digital representation of the analog model is developed by transforming the *s*-domain transfer function into a *z*-domain transfer function with errors of around 0.5% and 1.5% for amplitude and phase, respectively. Realization of the digital is performed using block diagrams that include unit delay, adder, and multiplier elements. Models are verified in Matlab Simulink and

compared with the *H(z)* transfer function output. Block diagram follows the transfer function output and the represents the transfer function successfully.

Third and the last model is the complete model of the transformers. This model represents the optics and the electronics of the system separately. The Jones calculus method is used to model the optical elements. The final state of the light, which gives information about the current and voltage signals, is calculated by matrix multiplications. This calculated information is processed by the electronics that is represented by the previously developed transfer functions. The complete model is developed and tested in Matlab® Simulink. Results show that the developed models successfully represent the optical transformers with accuracy of less than 1.5%. Simulation results show that the models are valid and produce the desired output signals.

CHAPTER 5

INVESTIGATION OF DIGITAL OUTPUT CHARACTERISTICS OF OPTICAL CURRENT TRANSFORMER

5.1 Introduction

The electric power system uses a rapidly increasing number of digital systems. Power system protection is one of the main application areas of digital systems in the power industry. Unlike the conventional instrument transformers, optical voltage and current transformers have a merging unit (MU) that inherently generates digital outputs. This increases the data transmission quality, provides reliable communication, and increases flexibility and functionality [69]-[73]. The digital output signals of optical transformers supply the digital protection system through a process bus based on IEC 61850-9-2 standard [74]. The protection relay accepting digital input based on the IEC standard is required to receive the measurement values from the instrument transformers. Fig. 5.1 shows the typical arrangement of the instrument transformers, relay, and circuit breaker necessary for the protection of a power line.

The performance of the conventional protection system is very well evaluated and defined and has been since the beginning of the power system. However, the performance of the digital systems is still being investigated. Many studies have been performed on process bus communication in the literature [75]-[78]. However, all-digital protection systems, which include different electronic instrument transformers connected to different digital relays through an IEC 61850-9-2 process bus, have not been studied in detail.

This chapter presents:

- The development of a test facility for a digital protection system and regeneration of a typical power system fault
- The discovery of four different types of time inverse characteristics of a digital relay
- An investigation of the effect of fault current with DC bias on relay tripping
- The investigation of the compatibility of an optical current transformer and a digital relay from different manufacturers
- Frequency response characteristics of OCT digital output

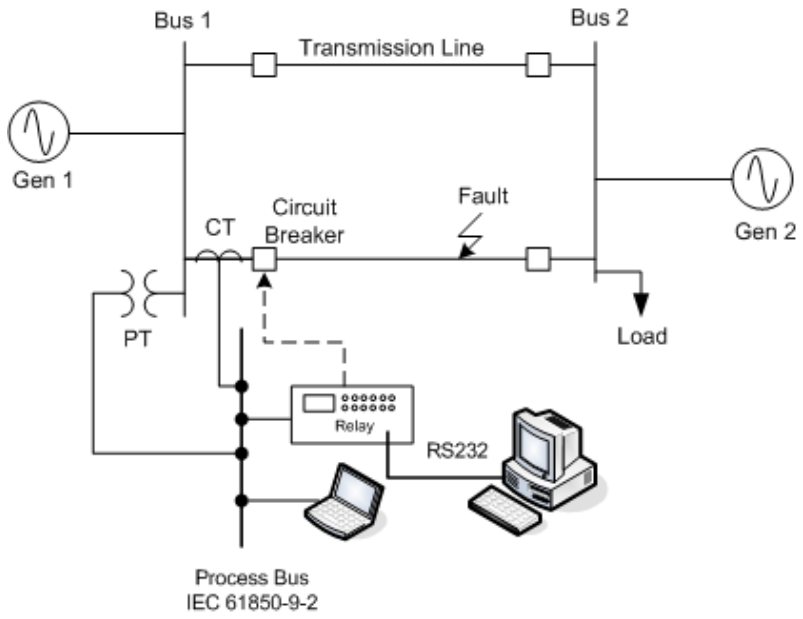

Fig. 5.1. Typical power system digital protection system

5.2 Testing of All-Digital Protection Systems

In order to test the digital protection system using optical instrument transformers inter-connected by an IEC 61850-9-2 process bus, a dedicated test facility is developed. Fig. 5.2 shows the one-line diagram used to test the all-digital over-current protection, and Fig. 5.3 shows the picture of the test system. The major components in the system are

- The current generator of the test setup
- NxtPhase optical current transformer (OCT), with Merging Unit (MU)
- AREVA digital relay
- A computer
- The current generator test setup consisting of three parts

The load current generator: The local 120 V network, through a regulating transformer, supplies the secondary 5 A windings of two 800 /5 A ring type current transformers connected in parallel. An insulated conductor passes through the ring of the current transformers to generate the load

current. A regulating transformer controls the magnitude of the load current, between 0-60 A. The conductor carries the load current thread through the optical current transformer ring.

The short circuit current generator: Three ring types of 600 A/5 A current transformers generate the fault current. The 5 A secondary winding of the current transformers are connected in parallel and supplied by a three phase regulating transformer. The regulating transformer controls the amplitude of the short circuit current. The electronic switch permits the selection of the fault initiation time between zero and 180 degrees on the source voltage wave. The maximum generated current in the primary circuit is 1,200 A.

The phase angle between the load current and the short circuit current during the fault is changed by supplying the regulating transformer of the short circuit current generator from the line-to-line voltage of phase AB, BC, or CA. For example, the change from AB to BC produces a 120-degree phase shift. Changing the amplitude of the supplied line-to-line voltage changes the generated current amplitude and the phase angle of the generated short circuit current.

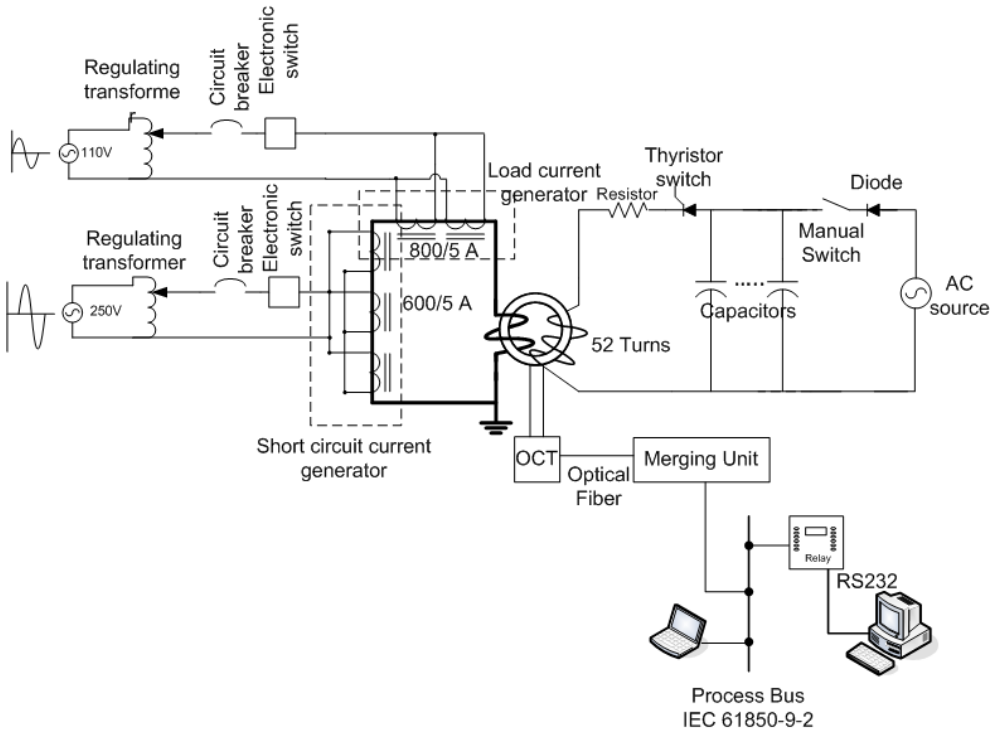

Fig. 5.2. The test setup for the all-digital over-current protection

DC offset generation: A DC component of the fault current can be simulated by the use of the DC bias current circuit, which discharges a charged capacitor through a few turns on the optical current transformer. The electronic switch, which discharges the capacitor, is synchronized with the initiation of the short circuit current. The total current that the OCT measures is the sum of the short circuit current and the DC discharged current. The magnitude of the DC offset is controlled by varying the voltage of the capacitor's DC power charging supply. The decay rate of the DC component can be controlled by varying the circuit parameters in the DC bias current circuit.

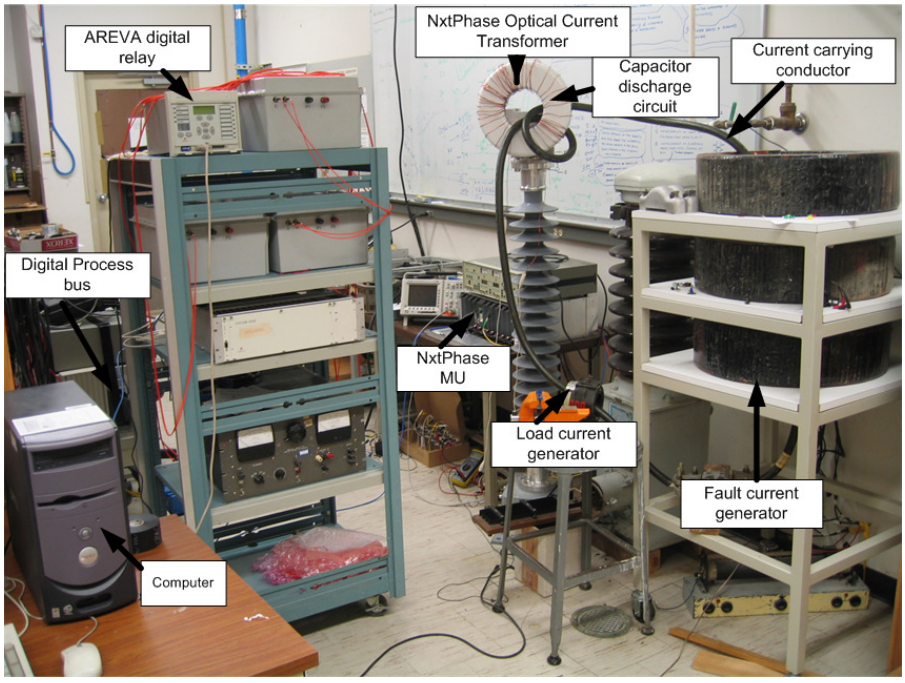

Fig. 5.3. Picture of the test setup for the all-digital over-current protection

The current generator of the test facility supplies the NxtPhase optical current transformer (OCT) with different over-currents. The digital output of the OCT merging unit is connected to the digital communication bus, which supplied both the AREVA digital relay and a computer. The computer records the data sent to the digital relay. The short circuit current carrying conductor is turned twice on the OCT sensor head to increase the applied current. The maximum applied current became 2,200 A. The specifications of the AREVA digital relay are

- AREVA Micom P440 relay:

- Nominal voltage: 24-125 VDC /110-250 VAC
- Operate range: 19-300 DC / 24-265 VAC
- Digital inputs: (Vmin/Vmax Tresholds) 24 /27, 30 /34, 48 /54, 110 /125, 220 /250
- Output contacts: maximum 46
- Setting groups: 4(2)
- Fault records: 5
- Event records: 250-512
- Disturbance record: 75 s maximum
- IEC 61850: Yes

The following tests are performed to verify the proper operation of an all-digital protection system. The test procedure is:

- The digital relay is set to the inverse over-current protection mode by selecting an inverse time delayed characteristic and threshold current.
- The relay is set to a high threshold current to prevent tripping.
- The high current generator, together with the DC offset current generator, is activated to produce a fault current.
- The relay records the fault current but does not trip it because of the high threshold setting. The relay record is reviewed to verify that the fault current is the desired value.
- The relay threshold current is adjusted to the selected value.
- The DC bias capacitors are re-charged to provide the DC offset current, and the high current generator is reactivated to produce the fault current again.
- The laptop connected to the processing bus records the fault current using an Ethernet network analyzer program.

- The fault current activates the relay, which produces an alarm signal or even a tripping signal.
- The circuit switches off, and the disturbance records are downloaded from the relay.
- Results are analyzed.

5.2.1 Digital Relay Settings and Characteristics

The AREVA Micom P440 relay has different features that can be adjusted to the desired functions. This relay can operate both as a distance relay and as an over-current relay. In over-current mode, it can operate as a directional over-current relay without time delay, with definite time delay, or with inverse time delay. Because of not having an optical voltage transformer with digital output, the relay in distance protection or directional over-current mode is not tested. The tests are limited to the investigation of relay operation in over-current mode with definite time delay or with inverse time delay. The relay has four different inverse time delayed characteristics;

- IEC E Inverse Curves
- IEC S Inverse Curves
- IEC V Inverse Curves
- IEEE V Inverse Curves

The AREVA relay has four over-current elements. The first two elements, with adjustable threshold currents of I1 and I2, can operate with definite time delay, with inverse time delay, or without time delay. The two other elements, with threshold currents of I3 and I4, can operate only in instantaneous or definite time delayed tripping mode. According to the relay specifications [79], the relay in inverse time delayed mode calculates the time delay by the following formula:

$$t = T \times \left(\frac{K}{(I / Is)^{\propto} - 1} + L \right) \tag{5.1}$$

where:

t = operation time

K = constant

I = measured current

Is = current threshold setting

α = constant

L = ANSI/IEEE constant (zero for IEC)

T = time multiplier setting

In general, if the fault or primary current is less than the threshold current, the relay output is zero. When the fault current exceeds the threshold current, the relay produces an alarm signal and calculates the required delay time using (5.1) or adjusting the delay time according to the required definite time delay. After the delay time, the relay produces a trip signal if the fault current is on. If the fault is cleared by another relay before the delay time is over, the relay will not operate; it will be reset automatically.

Since the OCT and the relay are from different manufacturers, there is a current transformer ratio mismatch in the relay settings. This mismatch is experimentally corrected using a magnetic current transformer and the relay reading. During the test of the protection circuit, the applied current amplitude is varied, and the relay response is evaluated by analyzing the disturbance records. The threshold current is adjusted to 100 A. The maximum peak current is 2200 A, which corresponded to 22 times the threshold current.

5.2.2 Short Circuit Simulation

The relay is set to the over-current protection mode using the IEC E inverse characteristics with a 100 A threshold or pick up current. Any value above 100 A trips the relay, which produces an alarm signal. Fig. 5.4 shows the relay operation when the fault current is only 101 A rms with a high DC bias current. The instantaneous value of the fault current is above 100 A, and as a result the relay gives an alarm signal and calculates the delay time, which is significantly more than 60 cycles because of the inverse time delayed characteristics. The figure shows that this current is switched off by the high current generator after 60 cycles; consequently, the relay does not produce a trip signal. However, the relay records the disturbance as shown in Fig. 5.4. The record

includes the current signal and trip signal. The figure shows only the current signal but not the trip signal.

The test is repeated using the same current; however, the current is not switched off after 60 cycles but maintained for about 10.5 seconds. Results show that the relay produces a square shape-tripping signal after about 10.1 seconds. The fault duration is 10,540 ms, and the tripping signal length is 1,687. This makes the tripping time around 10,540-1,687 = 8,853 ms = 8.8 s.

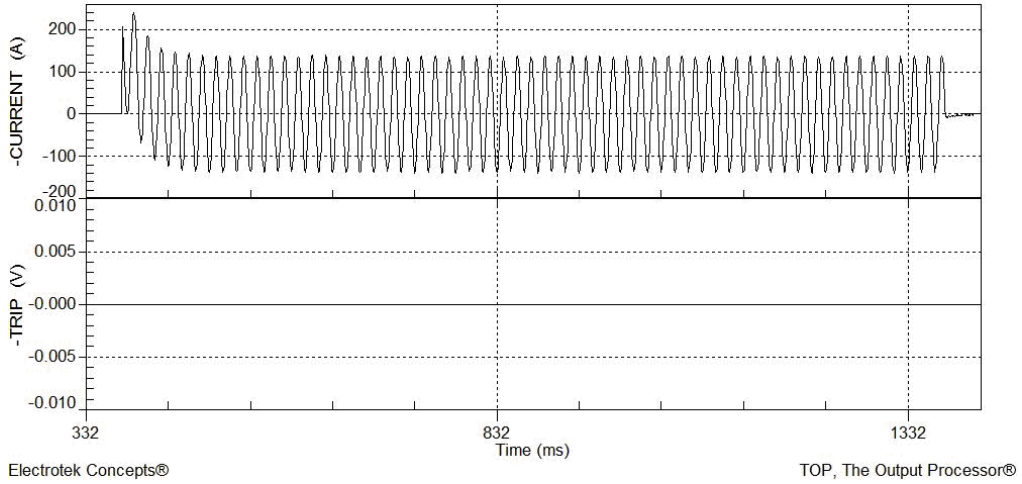

Fig. 5.4. 100 A continuous current

The applied fault current is increased to 500 A rms. It is applied for 60 cycles in order to trip the relay. The relay trips at 95.7 ms after fault initiation, which is much shorter than the 100 A fault tripping time. Fig. 5.5 shows the relay record of the fault current and the square shape of the tripping signal. The figure shows that the relay trips after around the 6th cycle of the fault, and it end when the fault current becomes zero. This is the same as with the 100 A tripping.

The applied fault current is increased to 2,200 A rms, which is 22 times the threshold current value of 100 A. The relay trips in a very short time after the fault initiated. It trips after 15.4 ms and in the first cycle of the fault.

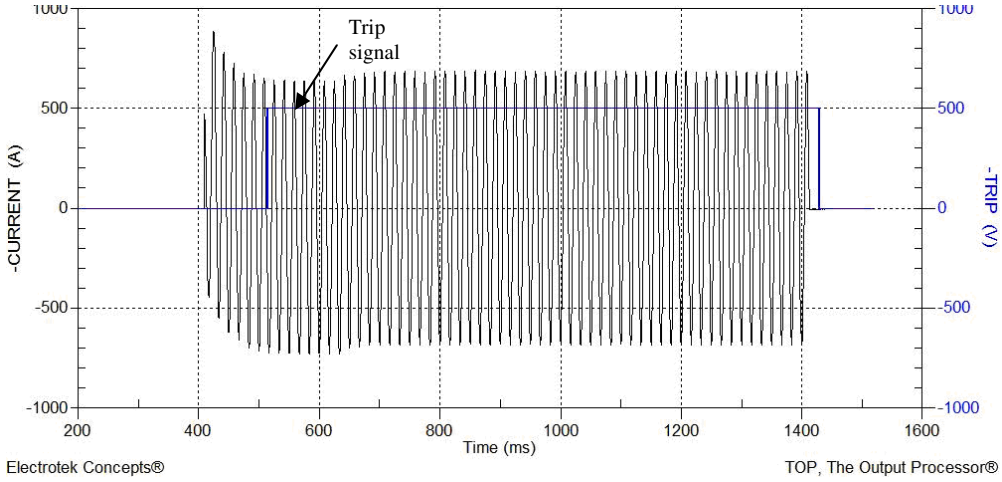

Fig. 5.5. 500 A fault simulation

The same methodology and steps described above are repeated for the four time inverse characteristics. For each characteristic, the relay tripping time is recorded in three ways: calculating the tripping time by using the computer recorded data sine waves, using the information about the fault on the relay LCD, and calculating the tripping time with the equation given in (5.1).

Three calculated curves are plotted together to show the four characteristics; this is shown in Fig. 5.6, Fig. 5.7, Fig. 5.8, and Fig. 5.9. Calculation of the tripping time from the recorded sine wave is almost identical to the relay reading values. However, the calculation of the tripping time by using (5.1) is significantly different from the other two curves.

The below figures show that in the IEC curves the calculated and the recorded readings match; however, in the IEEE inverse characteristic curves, the calculated values do not match the relay readings and records.

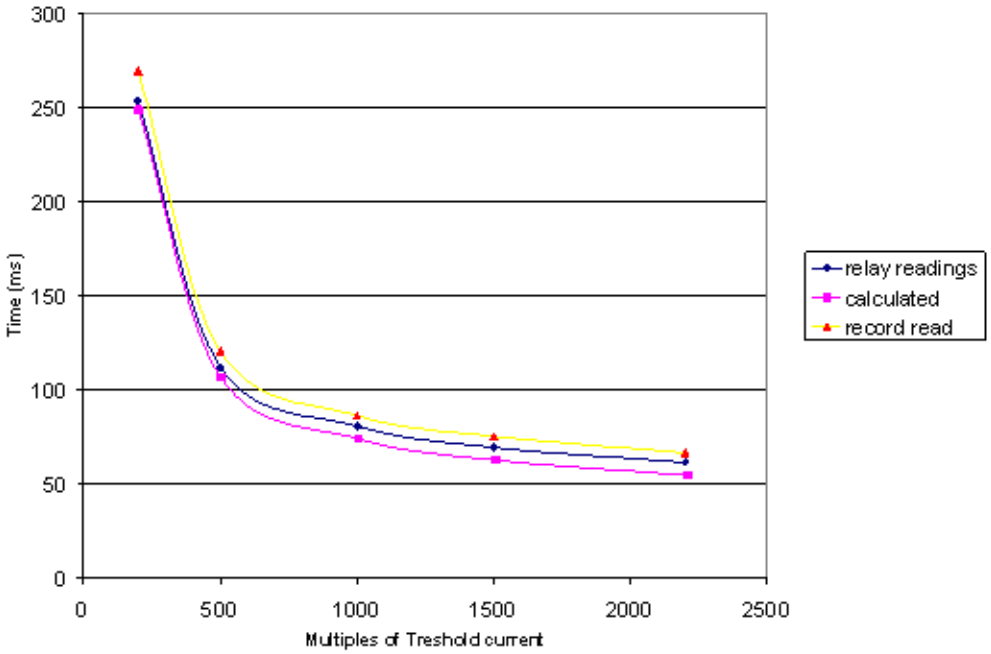

Fig. 5.6. IEC S inverse characteristic

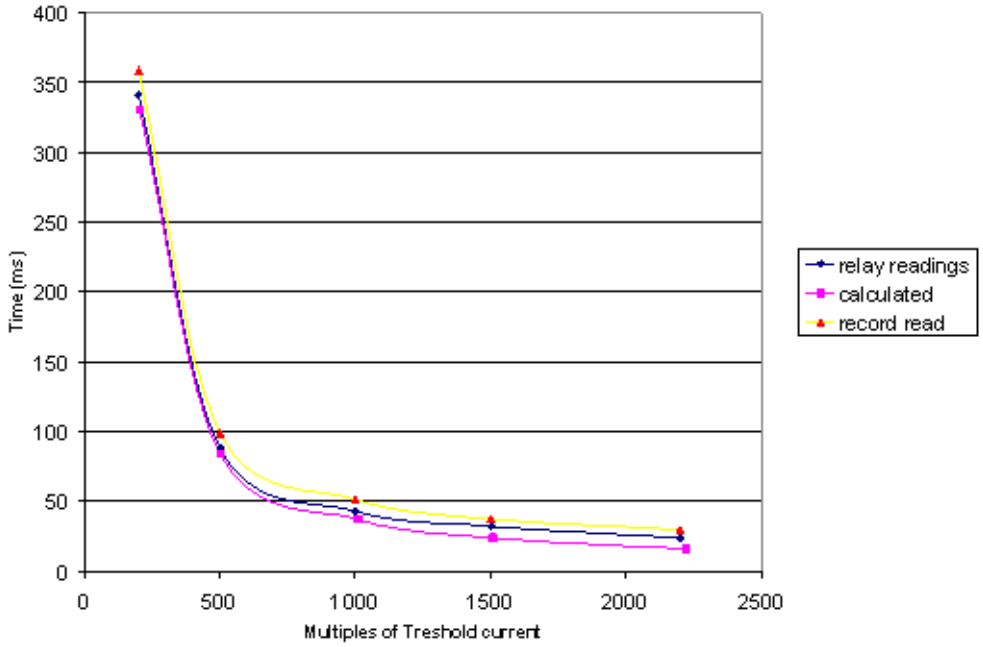

Fig. 5.7. IEC V inverse characteristic

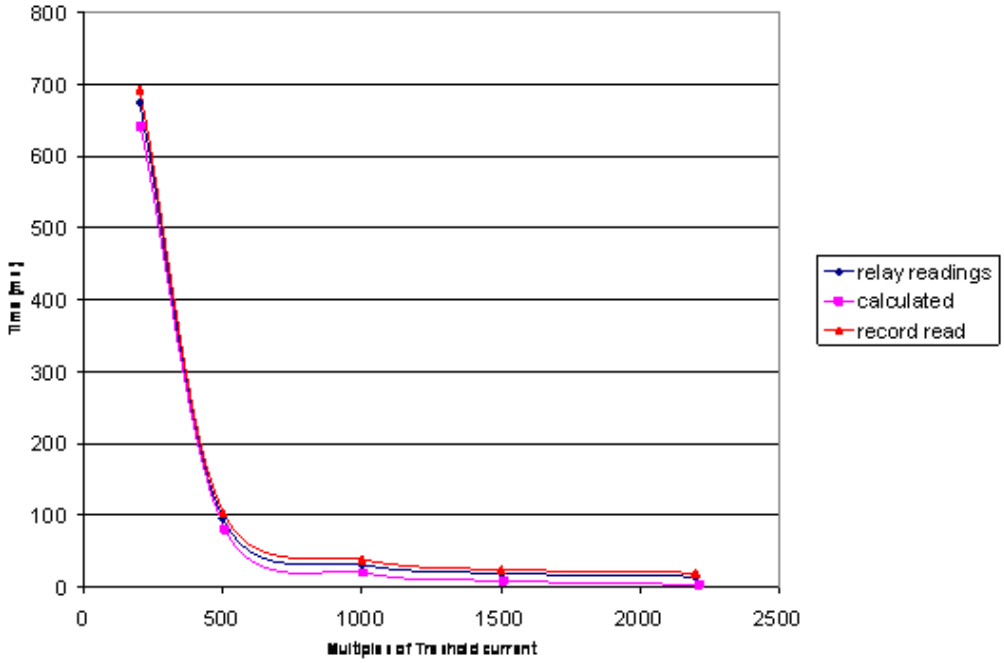

Fig. 5.8. IEC E inverse characteristic

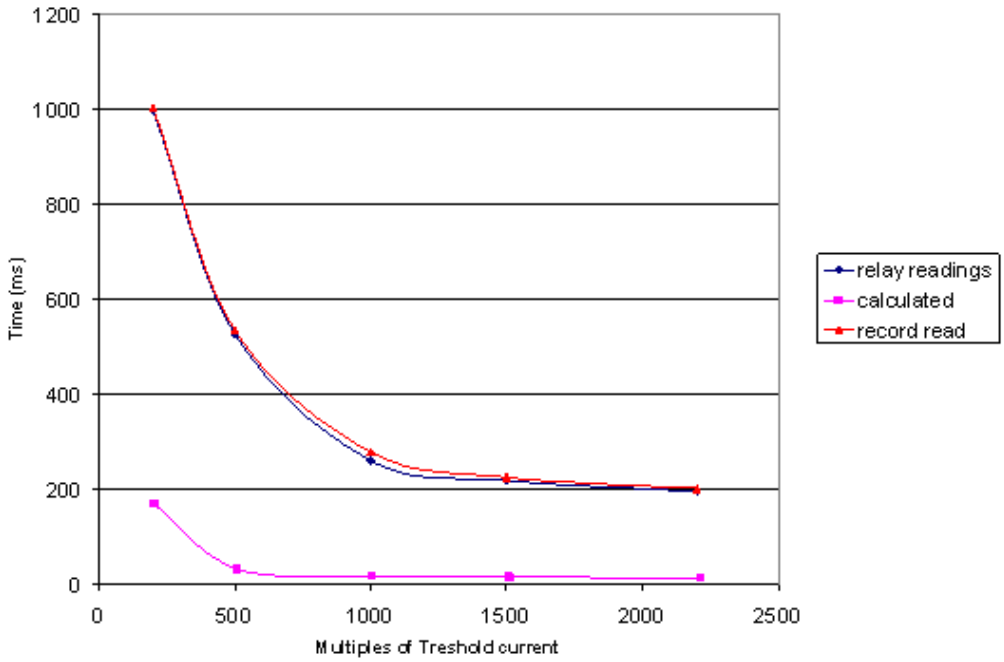

Fig. 5.9. IEEE V Inverse characteristic

5.2.3 DC Bias Effect on Trip/Alarm

When a fault occurs in a power system, a DC offset will appear due to the inductance and resistance of the system components. The effect of the DC offset is investigated earlier in [13]. In the first few cycles, the current value increases, but after the DC component attenuates, the current becomes constant. In order to find the DC offset's effect on tripping, three different values of DC bias levels are applied to the relay along with a 500 A rms fault current. The fault current and relay tripping times are plotted in the same figures after the tripping times are calculated.

Fig. 5.10 a and b show the recorded data of a consistent fault current with 0% and 25% DC offset currents. The recorded and analyzed results show that the relay tripping is almost the same for 0%, 10%, 15%, and 25% of the DC offset current. The relay tripped after the 6th cycle in each case.

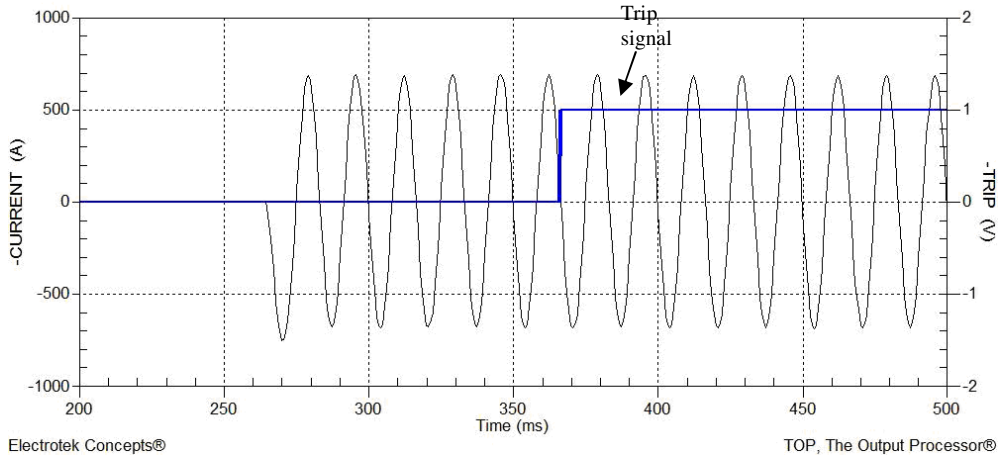

a)

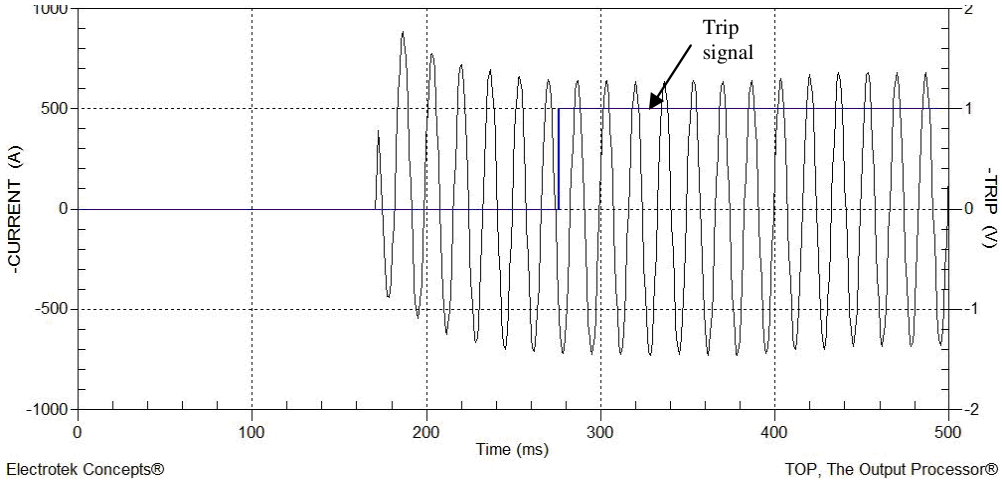

b)

Fig. 5.10. DC offset effect

5.2.4 The Effect of the Impulse Current on the Trip/Alarm

Switching transients frequently produce an impulse type transient current superimposed on the small AC load current. An impulse current is generated by discharging the capacitor used for the DC offset current generation, and the effect of this impulse current on relay operation is investigated. Fig. 5.11 shows the applied impulse current and the tripping signal.

The experimental results show that the digital relay gives an alarm signal if the impulse current is above the threshold value. The applied maximum impulse current is 400 A, which is above the threshold current, and its duration is 100 millisecond. Fig. 5.11 shows that the relay does not trip and gives only an alarm signal. This is an important result because the relatively short duration switching surge is not a fault, so it should not trip the relay.

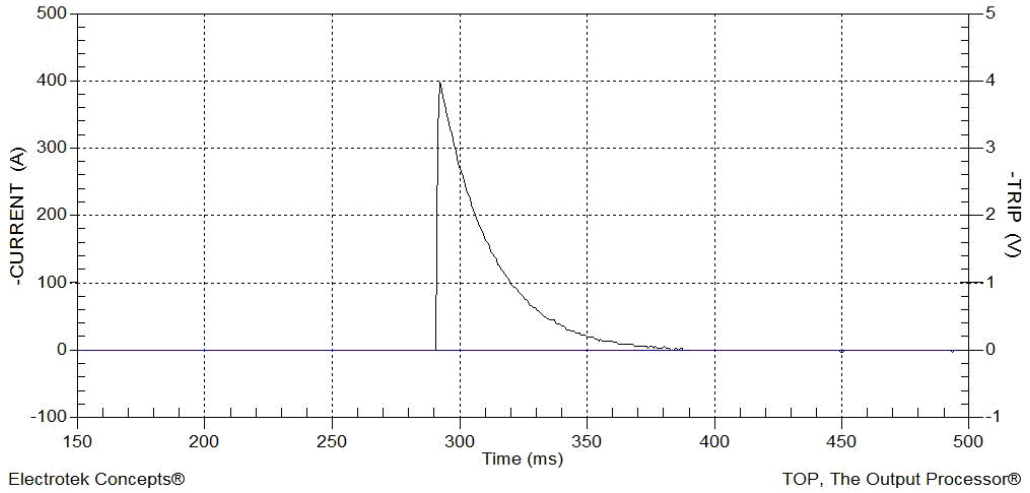

Fig. 5.11. Impulse current test

5.2.5 The Load Current and Short Circuit Current Simulation

All the experiments are performed without a load current to verify that the load current does not affect the relay operation. A new test is performed using a 60 A load current and a fault current of 700 A with DC offset. The relay is set to 100 A of the threshold current. The experiment is conducted using the test setup described in Chapter 5, section 2. The relay gives an alarm because the fault current is over the threshold value, and after a certain delay, it generates a trip signal.

The disturbance recorded by the relay is downloaded. Results show the recorded sine wave current and relay tripping decision. The relay trips according to the characteristics described in the previous sections. The test demonstrates that the load current has no effect on the relay operation if it is less than the threshold value.

5.3 Frequency Response Test of OCT Digital Output

One of the features of the OCT systems is having an optional digital output, which permits easy and safe transfer of the sampled values to protection devices. The purpose of the tests is to understand the digital data characteristics when the IEC 61850 standard is used, particularly the frequency bandwidth.

Fig. 5.12 shows the OCT block diagram based on IEC 60044-8 standard. The signal processing unit digitizes the current sensor produced light signal and the obtained digital signal is sent to both the D/A converter and to the Merging unit.

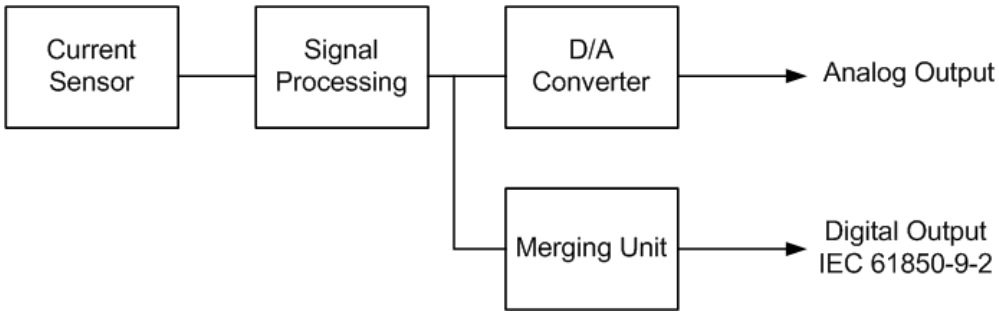

Fig. 5.12. OCT block diagram

The D/A converter generates a low energy analog signal. The merging unit re-samples the signal and generates a digital output in Ethernet format. This signal is transmitted through the Ethernet network to the protection and metering units. The process following the protocol is described in the IEC 61850-9-1 and 9-2 standards [40], [80].

Fig. 5.13 shows the test arrangement used for testing the digital output characteristics. A similar test setup was used earlier to investigate the analog output frequency response presented in Chapter 3. A signal generator, up to 1MHz frequency range, is used as a signal source. The variable frequency output voltage of the signal generator is amplified by a 1,000 W stereo amplifier. The loop current is kept constant at 4 A while the frequency is varied from 60 Hz to 4.8 kHz in steps of five. The total current going through the OCT sensor head is 4A x 55 = 220 A. The waveform of the output signal is captured and recorded at each frequency. Fig. 5.14 shows the test results for frequency-amplitude characteristics of OCT digital output.

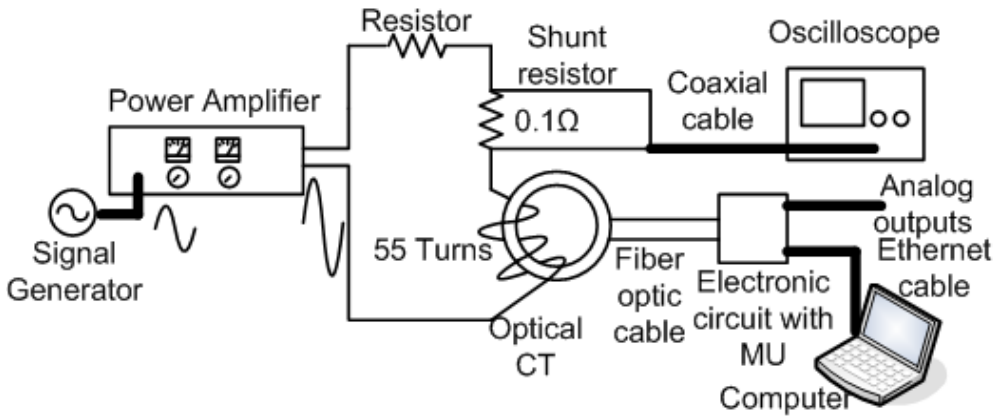

Fig. 5.13. Digital output test setup

The test results show that the 3-dB bandwidth of the OCT's 61850-9-2 digital output interface was about 2.4 kHz. On the other hand, as presented in Chapter 3, the analog output bandwidth is close to 20 kHz. The difference between the bandwidths of the analog and digital signals is mainly due to the sampling frequencies involved.

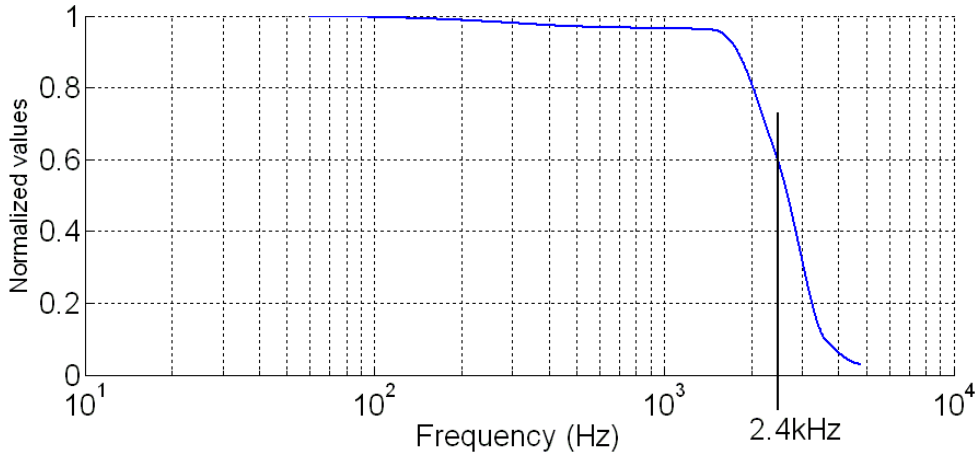

Fig. 5.14. Frequency-amplitude characteristics of OCT digital output

The test results and the merging unit specifications show that the merging unit has a sampling rate of 80 samples /cycle. The power frequency of 60 Hz corresponds to 4,800 samples in one sec. Fig. 5.15 shows the 60 Hz signal recording of the digital output. The UCA guide [81] to implementing IEC 61850-9-2 defines two sampling rates: 80 samples and 256 samples per cycle. These rates in a 60 Hz system correspond to 4,800 Hz and 15,360 Hz samples per second (sps), respectively [81]. Any input signal with a frequency higher than 2.4 kHz and 7,680 Hz is aliased

and has incorrect outputs. Test records confirm that the signal up to 2.4 kHz has perfect sine waves with correct sampling. Fig. 5.15 shows the 2.4 kHz signal recording of the digital output that has only two samples in one cycle corresponding to the 4,800 sps rate. However, signals above the 2.4 kHz are aliased, and the waveforms have distortions. Fig. 5.16 shows the recorded signal for 4.8 kHz. It has four samples per cycle that are randomly distributed and aliased. Please note that in this case, to observe aliasing, the digital output of the OCT merging unit is not filtered by an anti-aliasing filter.

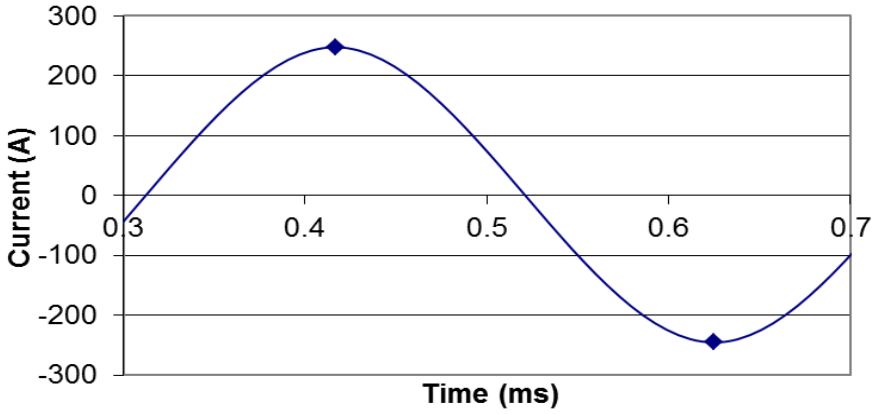

Fig. 5.15. Digital output for 2.4 kHz with two-sampled value

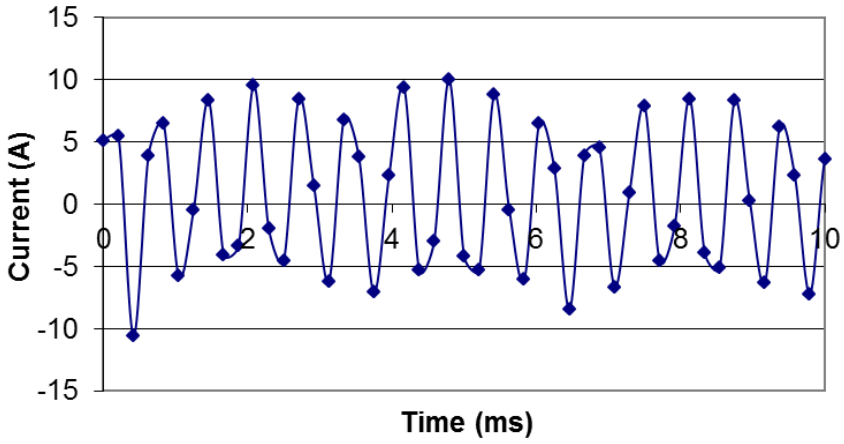

Fig. 5.16. Digital output for 4.8 kHz with two-sampled value

The test results show that the bandwidth of the OCT is limited to 2.4 kHz, as expected from Nyquist theorem, due to the sampling rate of the merging unit. On the other hand, the analog signal has a higher bandwidth since the D/A converter for analog output processes the data at a much higher rate. In this case, the OCT D/A is supplied at 333,000 samples per second with digital data that was filtered (anti-aliasing) at an effective 3-dB bandwidth of 20 kHz.

The choice of the sampling/communication rate depends on the application as well as the total capacity of the communication system. The best choice is a compromise: high data rates (large bandwidth) may enable more applications but also loads (or overloads) the communication system. For example, 80 and 256 samples per cycle prescribed in [81] load a 100 MB/s Ethernet network to about 5 to 12 % [82], respectively. Considering that most common relays and meters use internal sampling rates less than 128 samples per cycle, the prescribed values in the UCA guide [81] appear to be sufficient for most applications, without unnecessarily overburdening the communication network with excessive data.

The phase characteristic of the merging unit output is not measurable due to the time latency of data transmission. According to the standard, merging unit output can have up to 3ms delay. This delay does not allow for measuring of the phase response characteristics of the digital output. Hence, a model for digital output cannot be developed without the complete frequency response characteristics.

5.4 Conclusion

In conclusion, the all-digital over-current protection operated well and the all-digital system is suitable to protect an electric power system where over-current protection is needed.

The different manufacturers (AREVA and NxtPhase) provided a current transformer and digital relay that can work together; however, significant mismatch is discovered between the current values measured by the digital relay and by the NxtPhase optical current transformer when AREVA software is used. The mismatch requires correction from both manufacturers' software.

The details of the findings are as follows:

- The all-digital over-current protection system is tested using a realistic high current, which supplies the primary side of the optical CT.
- A dedicated test facility is developed that generates high current and high voltage to simulate the current and voltage that occurs in the power network.
- All digital protection system is tested in inverse over-current mode. The system operates well and clears the faults with proper delay. However, though the relay measures the current dependent time delay accurately, the calculated time delay from the manufacturer's equation is different. This suggests that a software review should be done.
- The test results show that the load current and short duration impulse currents do not produce any tripping signal.
- The DC offset current does not affect the tripping time adversely
- Because of the lack of equipment, the all-digital protection system is not tested in distance protection mode, and the directional over-current relay proper operation is not verified.
- The digital output signal bandwidth (2.4 kHz) is significantly lower than the analog signal bandwidth (20 kHz).
- The lower digital signal bandwidth is due to the re-sampling of the digital signal 80 times /60Hz period.

CHAPTER 6

CONCLUSIONS AND FUTURE WORK

6.1 Conclusions

Developing models for optical instrument transformers first requires a detailed study to collect information about the devices. Characteristics of the devices define the selection of model development method. In this study, a comprehensive study about the performances and characteristics of the optical systems under different conditions is investigated. Test results give insight about the devices to develop models.

Experimental comparison of the performance of magnetic and optical instrument transformers is presented. Optical systems have protection and metering outputs. The optical VT has only one setting, which can be used for metering or protection. The conventional instrument transformers have one output, 1 A or 5 A in the case of CT, and 69 V or 115 V in case of VT. The optical instrument transformers have three outputs:

- Digital
- Low energy analog (LEA) Optical CT = 4 V, Optical VT= 4 V
- High energy analog (HEA) Optical CT = 1 or 5 A Optical VT =69 /120 V

These outputs gained, for the optical systems, a wide variety of applications. However, traditional systems have only analog outputs. Optical systems output has an inherent white noise which does not have too much effect on metering and protection applications. The saturation of the magnetic instrument transformers has an effect on protection systems. On the other hand, optical systems have no saturation. A small phase shift (less than 1 degree) is observed between the two transformers. This is because the OCT optical system has a 40 μs inherent delay. For the OVT, the delay is 40 μs as well. The measurement accuracy of the optical current systems is investigated, and the manufacturer specification of 0.2% is verified. The rms difference between the two transformers is less than 2% in the 200A-750A range. For the optical voltage transformers, the difference between the two VTs is less than 1% under the rated voltage but increases rapidly above the rated voltage due to saturation of magnetic VT. The transient performance of OCT is measured, comparing the reproduction of short circuit current and direct measurement of fre-

quency characteristics. The results show around 2.3% differences in peak short circuit current reproduction. The OCT response is tested using DC pulse. The OCT signal showed 68 μs delay and the rise time of the pulse appeared increased. The transient performance of NxtPhase provided OVT is evaluated, comparing the VTs response to short-circuit produced voltage drop in the field, a lightning impulse test, and direct measurement of frequency characteristics. The results show that the comparison of magnetic VT and optical VT shows around less than 0.25% differences in rms voltages. The comparison of instantaneous voltage values shows less than 1.8% differences. The lightning impulse test shows that the magnetic VT and the OVT HEA output do not reproduce the lightning impulse. The LEA output reproduced the impulse fairly well.

A methodology for developing a model for transformers is presented, and three different models are developed for analog outputs of transformers. The analog output is represented with a transfer function that is developed from the frequency response characteristics of the transformers. A complex curve fitting method is used for approximation. Frequency responses of developed transfer functions are compared with experimental results, and 0.41% difference in amplitude and 1.11% difference in phase are found for OCT. In amplitude, 1.52% phase difference is found and 0.38% for OVT. Electrical circuit models for the optical instrument transformers are developed from approximated transfer functions. Transfer functions are represented by rational functions in terms of residues and poles. A network synthesis method is used to develop circuit models from each rational function. The equivalent circuit consists of RLC and VCVS elements. Developed models are tested by using simulation programs like Matlab, PSpice and EMTP. Differences are found as 1.43% in amplitude and 0.72% in phase for OCT, and 1.43% in amplitude and 0.79% in phase for OVT. Results are analyzed and compared with the traditional instrument transformers model results. Results show that the developed models can successfully be used for simulations.

A digital model for analog output is developed. The transfer function used for analog model is transformed to digital model transfer function using bilinear transformation method. Developed two transfer functions and experimental frequency responses are compared, and the difference is found within 1.5%.

A complete model for analog output is developed as the third model. The physics and the operational principle of the optical systems are investigated. Optical transformers consist of two parts: the optical sensing part and the electronics part that processes the information coming from the optics. The optical sensing part of the transformers uses Farady and Pockels effects to sense the current and voltages through fiber optic cable. A polarized light beam goes through the fiber optic cable and enters the magnetic and electrical fields. Each step and components of this optical sensing process are modeled by the Jones calculus method. These developed mathematical models of optical sensing parts are incorporated with the second part of the transformers, the electronics. Electronics consist of the analog to digital converters and filter circuits. The previously developed transfer functions are used at this stage to model the electronics. The information that was experimentally collected is used to model the electronics since the characteristics of the optical parts of the transformers are independent from frequency. The final model combines the two parts, the optical and electrical models.

Digital output of the OCT is analyzed. The amplitude-frequency characteristic of the OCT is obtained. It is seen that OCT has a bandwidth limit of 2.4 kHz, which is very little comparing to its analog output. The lower digital signal bandwidth is due to the re-sampling of the digital signal 80 times/60 Hz period. Phase-frequency characteristic of the transformer is not obtained due to the latency of the data transmission. The standard defines the latency up to 3ms that makes the measurements complex if no real time stamp of data exists. A dedicated test facility that generates high current and high voltage to simulate the current and voltage that occurs in the power network is developed. All digital protection system is tested in inverse over-current mode. The system operated successfully and cleared the faults with proper delay. The DC offset current does not affect the tripping time adversely.

6.2 Future Work

The goal of this research is to compare magnetic instrument transformers' and optical instrument transformers' performances and develop models for optical instrument transformers. Tests are performed only with one specific manufacturer's transformers. Tests can be repeated

with other commercially available transformers. Digital output of optical current transformer is investigated. Digital output of optical voltage transformer can also be investigated. Phase response characteristics of digital output can be analyzed. Developed models are only for the analog output models. Digital output of both optical current and voltage transformer can be developed. However, this requires a better understanding of IEC 61850 standards. All the developed models can be incorporated with digital relays, and testing of protection system can be simulated.

REFERENCES

[1] B. D. Jenkins, "Introduction to Instrument Transformers," George Newnes, London, 1967, page 4.

[2] A. P Steer, S. J. Turner, P. R. B. Farrie, R. P Tatam, A. N. Tobin, J. D. C. Jones, D. A. Jackson, "Optical fiber current sensor for circuit protection," in *Proc. IEEE Fourth International Conf. Developments in Power Protection,* 1989, pp. 296-300.

[3] T. Sawa, K. Kurosawa, T. Kaminishi, T. Yokota, "Development of optical instrument transformers," *IEEE Trans. on Power Delivery*, vol. 5, pp.884-891, April 1990.

[4] Y. C. L. Frankie, C. K. C. Wilson, M. S. Demokan, "Fiber-optic current sensor developed for power system measurement," in *Proc. International Conference on Ad-vances in Power System Control, Operation and Management (APSCOM)*, 1991, pp. 637-643.

[5] A. Cruden, J. R. McDonald, I. Andonovic, D. Uttamchandani, R. Porrelli, K. Allan, "Current measurement device based on the Faraday effect," in *Proc. IEEE Fifth International Conference on Developments in Power System Protection*, 1993, pp. 69-72.

[6] A. Cruden, Z. J. Richardson, J. R. McDonald, L. Andonovic, "Optical crystal based devices for current and voltage measurement," *IEEE Transactions on Power Delivery*, vol.10, pp. 1217-1223, July 1995.

[7] T. D. Maffetone, T. M. McClelland, "345 kV substation optical current measurement system for revenue metering and protective relaying," *IEEE Trans. Power Delivery*, vol. 6, pp. 1430-1437, Oct. 1991.

[8] P. G. Zhang, D. Irvine-Halliday, "Faraday effect optical current sensor," in *Proc. Canadian Conference on Electrical and Computer Engineering*, 1996, pp. 871-875.

[9] J. G. Werthen, A. G. Andersson, S. T. Weiss, H. O. Bjorklund, "Current measurements using optical power," in *Proc. IEEE Transmission and Distribution Conference*, 1996, pp. 213-218.

[10] Y. Nie, X. Yin, Z. Zhang, "Optical current transducer used in high voltage power system," *in Proc. IEEE/PES Transmission and Distribution Conference and Exhibition 2002 Asia Pacific*, 2002, pp. 1849-1853.

[11] M. Willsch, T. Bosselmann, "Optical current sensor application in the harsh environment of a 120 MVA power generator," in *Proc. Optical Fiber Sensors Conference Technical Digest*, 2002, pp. 407-410.

[12] W. C. Michie, A. Cruden, P. Niewczas, W. I. Madden, J. R. McDonald, M. Gauduin, "Harmonic analysis of current waveforms using optical current sensor," *IEEE Trans. on Instrumentation and Measurement*, vol. 51, 2002. pp. 1023-1026

[13] J. D. P Hrabliuk, "Optical current sensors eliminate CT saturation," in *Proc IEEE Power Engineering Society Winter Meeting*, New York, 2002, pp. 1478-1481.

[14] J. D. P. Hrabliuk, “Interfacing optical current sensors in a substation,” in *Proc. IEEE Power Engineering Society Summer Meeting,* 2001, pp. 147-155.

[15] G. Nicholson, “Reliability considerations: optical sensors for the control and measurement of power,” in *Proc. IEEE/PES Transmission and Distribution Conference and Exposition*, 2001, pp. 122-126.

[16] J. Blake, “Fiber optic current sensor calibration,” in *Proc. IEEE Transmission and Distribution Conference and Exposition*, Atlanta, 2001, pp. 127-130.

[17] F. Rahmatian, P. P. Chavez, “SF6-Free 550 kV Combined optical voltage and current transducer system,” in *Proc. IEEE Transmission and Distribution Conf.* 2003, pp. 379-382.

[18] J. N. Blake, A. H. Rose, “Fiber-Optic current transducer optimized for power metering applications,” in *Proc. IEEE Transmission and Distribution Conf.*, 2003, pp. 405-408.

[19] C. Jinling, L. Hongbin, L. Yanbing, W. Xiaowei, “A novel optical current transformer based on comparative measurement,” in *Proc. IEEE 41st International Conf. Universities Power Engineering*, Newcastle, 2006, pp. 837-840.

[20] C. Qingqian, H. Hou, D. You, Y. Xianggen, Y. Zhandong, “Research on improvements of using electronic current transformer on distance protection,” in *Proc. IEEE 42nd International Conf. Universities Power Engineering*, Brighton, 2007, pp. 267-272.

[21] F. Rahmatian, J. N. Blake, “Applications of high-voltage fiber optic current sensors,” in *Proc. IEEE Power Engineering Society General Meeting*, Montreal, 2006, pp. 1-6.

[22] C. Li, X. Cui, T. Yoshino, “Measurement of AC Electric Power Based on Dual Transverse Pockels Effect,” *IEEE Trans. on Instrumentation and Measurement*, vol. 50, October 2001, pp. 1375-1380.

[23] T. W. Cease, J. G. Driggans, S. J. Weikel, “Optical voltage and current sensors used in revenue metering system,” *IEEE Trans. on Power Delivery,* vol. 6, October 1991, pp. 1374-1379

[24] T. W. Cease, P. M. Johnston, “A magneto-optic current transducer,” *IEEE Trans. on Power Delivery,* vol. 5, April, 1990. pp. 548-555.

[25] L. H. Christensen, “Design, construction, and test of a passive optical prototype high voltage instrument transformer,” *IEEE Trans. on Power Delivery*, vol. 10, July 1995, pp. 1332-1337.

[26] K. Kurosawa, S. Yoshida, E. Mori, G. Takahashi, S. Saito, “ Development of an optical instrument transformer for DC voltage measurement,” *IEEE Trans. on Power Delivery*, vol. 8, October 1993, pp.1721-1726.

[27] P. Bauerschmidt, R. Lerch, "Optical voltage sensor based on a quartz resonator," in *Proc. IEEE Ultrasonics Symposium*, 1996, pp. 383-387.

[28] V. N. Filippov, A. N. Starodumov, Y. O. Barmenkov, and V. V. Makarov, "Fiber-Optic voltage sensor based on a Bi 12 TiO 20 crystal ," *Trans. Applied Optics*, , vol. 39, 2000, pp. 1389-1393.

[29] J. C. Santos, M. C. Taplamacioglu, K. Hidaka, "Pockels high-voltage measurement system," *IEEE Trans. Power Delivery,* vol. 15, January 2000, pp. 8-13.

[30] C. Li, X. Cui, "An optical voltage and current sensor with electrically switchable quarter waveplate," *Trans. Sensors and Actuators A: Physical*, vol. 126, January 2006, pp. 62-67.

[31] P. G. Zhang, D. Irvine-Halliday, " A practical hybrid optical fiber based high voltage sensor," *Canadian Conf. on Electrical and Computer Engineering*, 1996, pp. 888-890.

[32] F. Rahmatian, P. P. Chavez, and N. A. F. Jaeger, "138 kV and 345 kV wide-band SF6-free optical voltage transducers," *IEEE PES Winter Power Meeting*, January 2002, pp. 1472-1477.

[33] F. Rahmatian, P. P. Chavez, and N. A. F. Jaeger, "A 230 kV optical voltage transducer using multiple electric field sensors," *IEEE Trans. on Power Delivery*, vol. 17, Apr. 2002, pp. 417-422.

[34] F. Rahmatian, P. Chavez, and N. A. F. Jaeger, "Wide-Band 138 kV distributed-sensor optical voltage transducer: Study of accuracy under pollution and other field disturbances," *IEEE PES Summer Meeting*, 2001, pp.156-161.

[35] F. Rahmatian, D. Romalo, S. Lee, A. Fekete, S. Liu, N. A. F. Jaeger, and P. P. Chavez, "Optical voltage transducers for high-voltage applications," in *Proc. EPRI Optical Sensor Systems Workshop*, January 26-28, 2000.

[36] F. Rahmatian, P. P. Chavez, and N. A. F. Jaeger, "Resistively shielded optical voltage transducer," in *Proc. IEEE Transmission & Distribution Conference*, 2001, pp. 117-121.

[37] K. Bohnert, P. Gabus, and H. Brändle, "Fiber-optic current and voltage sensors for high-voltage substations," *invited paper at 16th International Conference on Optical Fiber Sensors*, 2003, Nara Lapan Technical Digest, pp. 752-754.

[38] J. Blake, W. Williams, C. Glasow, R. Bergh, K. Fetting, E. Hadley, G. Sanders, "Optical current transducers for high voltage applications," *Intelligent Processing and Manufacturing of Materials 3rd International Conference*, Vancouver, July 29, 2001.

[39] Instrument Transformers IEC Standard 60044, 2002.

[40] Communication networks and systems in substations, IEC61850-9-1, 2003.

[41] P. P. Chavez, F. Rahmatian, , and N. A. F. Jaeger, "Accurate voltage measurement with electric field sampling using permittivity-shielding," *IEEE Trans. Power Delivery*, vol. 17, Apr. 2002. pp. 362-368.

[42] P. P. Chavez, N. A. F. Jaeger, F. Rahmatian, "Accurate voltage measurement by the quadrature method," *IEEE Trans. Power Delivery*, vol. 18, January 2003. pp. 14-19.

[43] NxtPhase T&D Corporation, available at: http://www.nxtphase.com

[44] F. Rahmatian, P. P. Chavez, and N. A. F. Jaeger, "A wide-band SF6-free optical voltage transformer," *3rd EPRI Sensor Systems Workshop*, Pittsburgh, 2001.

[45] J. Bak-Jensen, B. Bak-Jensen, S. D. Ilfkkelsen, C. C. Jensen, "Parameter identification in potential transformer modeling," *IEEE Trans. Power Delivery*, vol. 7, January 1992. pp. 70-76.

[46] A. Morched, L. Mad, J. Ottevangers, "A high frequency transformer model for the EMTP," *IEEE Trans. Power Delivery,* vol. 8, July 1993. pp. 1615-1626.

[47] M. Kezunovic, Y. Guo, "Modeling and simulation of the power transformer faults and related protective relay behavior," *IEEE Trans. Power Delivery*, vol. 15, January 2000. pp. 44-50.

[48] A. O. Soysal, A. Semlyen, "Practical transfer function estimation and its applications to wide frequency range representation of transformers," *IEEE Trans. Power Delivery*, vol. 8, July 1993. pp. 1627-1637.

[49] M. I. Samesima, J. D. de Oliveira, E. M. Dias, "Frequency response analysis and modeling of measurement transformer under distorted current and voltage supply," *IEEE Trans. Power Delivery*, vol. 6, October 1991, pp. 1762-1768.

[50] J. Pleite, E. Olias, A. Barrado, A. Lazaro, R. Vazquez, "Frequency response modeling for device analysis," in *Proc. IEEE Annual Conf. on Industrial Electronics Society*, 2002, pp. 1457-1462.

[51] M. Wu, X. Cui, "Wide frequency model for transfer function of potential transformer in substation," in *Proc. IEEE International Symposium on Electromagnetic Compatibility*, 2003, pp. 327-330.

[52] J. D. Greeene, C. A. Gross, "Nonlinear modeling of transformers," *IEEE Trans. Industry Applications,* vol. 24, May 1988, pp. 434-438.

[53] User's Guide Version 7 on Signal Processing Toolbox Matlab.

[54] E.C. Levi, "Complex-Curve Fitting," *IRE Trans. on Automatic Control*, vol.AC-4, 1959, pp.37-44.

[55] X. Zhang, G. Liang, Q. Xie, H. Sun, "Modeling of the transfer function windings under VFT based on transfer function," in *Proc. IEEE Power System Technology*, 2006, pp.1-4.

[56] Series and Parallel Transfer Functions, available at: http://ccrma.stanford.edu/~jos/fp/Series_Parallel_Transfer_Functions.html

[57] M. J. Roberts, "Signals and Systems, Analysis Using Transform Methods and MAT-LAB®," McGraw-Hill, 2004, page 839.

[58] Digital filter realizations, lecture notes, available at: http://www.kemt.fei.tuke.sk/Predmety/KEMT421_DF/_materialy/Lectures/df_lesson_08.pdf

[59] E. Collett, "Polarized Light in Fiber Optics," SPIE Press, 2003, page 379.

[60] A. Yariv, P. Yeh, "Optical Waves in Crystals," Wiley, New York, 1983, page 121.

[61] D. Goldstein, "Polarized Light," Marcel Dekker, 2003, page 211.

[62] S. Zhou, X. Zhang, "Simulation of linear birefringe reduction in fiber-optical current sensor," *IEEE Photonics Technology Letters*, vol. 19, October 2007, pp. 1568-1570.

[63] X. Li, G. Wang, Z. He, "Establishment and theoretical analysis of mathematical model for dual-mode fiber optic current sensor," in *Proc. IEEE International Conf. on Mechatronics and Automation,* 2009, pp. 4272-4276.

[64] W. Zhengping, K.Chong, H. Zongjun, Z. Xueyuan, "Faraday mirror-typed optical current transformers and its theoretical analysis," *Trans. Optics&Laser Technology*, vol. 39, , March 2007, pp. 368-371.

[65] T. Bosselmann, "Electric and magnetic field sensing for high voltage applications," in *Proc. SPIE*, 1997, pp. 305-316.

[66] J. Blake, P. Tantaswadi, R. T. de Carvalho, "In-line sagnac interferometer current sensor," *IEEE Trans. Power Delivery*, vol. 11, January 1996, pp. 116-121.

[67] M. Berwick, J. D. C. Jones, D. A. Jackson, "Alternating-current measurement and noninvasive data ring utilizing the Faraday effect in a closed-loop fiber magnetometer," *Optics Letters*, vol. 12, April 1987, pp. 293-295.

[68] F. Rahmatian, N. A. F. Jaeger, "An integrated optics sensor for high-voltage measurement application ," in *Proc. Canadian Electrical and Computer Engineering Conference*, 1993, pp. 672-675.

[69] M. Kezunovic, L. Portillo, G. Karady, S. Kucuksari, "Impact of Optical Instrument Transformer Characteristics on the Performance of Protective Relays and Power Quality Meters,"

in *Proc Transmission & Distribution Conference and Exposition: Latin America*, 2006, pp. 1-7.

[70] A. Apostolov, B. Vandiver, "Functional testing of IEC 61850 based protection relays," in *Proc. 60th Annual Conference for Protective Relay Engineers,* 2007, pp. 333-340.

[71] H. Hou, T. Xu, D. You, X. Yin, W. Chen, B. Wang, X. He, "Research on protection equipment with digital interface based on IEC-61850," in *Proc. IEEE Power Engi-neering Society General Meeting*, 2007, pp.1-5.

[72] V. Skendzic, A. Guzma, "Enhancing power system automation through the use of real-time ethernet," in *Proc. Power Systems Conference: Advanced Metering, Protection, Control, Communication, and Distributed Resources*, 2006, pp. 480-495.

[73] R. E. Mackiewicz, "Overview of IEC 61850 and benefits," in *Proc. IEEE Power Systems Conference and Exposition,* 2006, pp. 623-630.

[74] Communication networks and systems in substation-Part 9-2: Specific communica-tion service mapping (SCSM) - Sampled analog values over ISO 8802-3, IEC Std. 61850.

[75] A. Apostolov, F. Auperrin, R. Passet, M. Guenego, F. Gilles, "IEC 61850 process bus based distributed waveform recording," in *Proc. IEEE Power Engineering Society General Meeting*, 2006, pp. 1-6.

[76] H-J. Herrmann, J. Andreas, "Impact of decentralized transformer electronics on the protection relay design," in *Proc. IEEE Developments in Power System Protection*, 2004, pp.136-139.

[77] G-S. Kim, H-H. Lee, "A study on IEC 61850 based communication for intelligent electronic devices," in *Proc. IEEE International Symposium on Science and Technology*, 2005, pp.765-770.

[78] M. Desjardine, P. Forsyth, R. Mackiewicz, "Real time simulation testing using IEC 61850," *International Conference on Power Systems Transients (IPST'07)*, 2007.

[79] AREVA Micom P441 Relay Manual.

[80] Communication networks and systems in substations, IEC61850-9-2, 2004.

[81] UCA International Users Group Guide, "Implementation guideline for digital inter-face to instrument transformers using IEC 61850-9-2," Rev 3, Aug. 2005.

[82] V. Skendzic, I. Ender, G. Zweigle, "IEC 61850-9-2 Process Bus and Its Impact on Power System Protection and Control Reliability," available at: http://www.selinc.com/techpprs/6275_Process%20Bus_VS_20070226.pdf.

APPENDIX A

DEVELOPMENT OF MODEL FOR OPTICAL CURRENT TRANSFORMER

```
%%%%% Transfer function model development  %%%%%%

clear
clc

%%%%%  Experimental values  %%%%%

        %Hz             %Magnitude        %Phase
Bode = [
        60              1                -0.86
        300             0.992074         -7.78
        1000            0.971343         -29.2118
        2000            0.924321         -52.42
        4000            0.763616         -104.54
        6000            0.601726         -149.47
        7670            0.466982         -181.13
        8200            0.435284         -197.05
        10000           0.335722         -223.20
        12000           0.242624         -259.78
        14000           0.181836         -301.54
        16800           0.137844         -353.95 ];

w     = (2*pi)*Bode(:,1);  %rad/sec
mag   = Bode(:,2);
phase = Bode(:,3)*(pi/180);
H = mag .* exp(j*phase);

[b,a] = invfreqs(H,w,3,5,[],50,0.001); % TF coefficients
Gs=tf(b,a) %developed TF

figure
bode(Gs)

%%%%%%Bode plot comparison of develeoped TF and exp measurements
%%%%%%%%

% Experimental frequencies applied to TF

Freq=[377;1885;6283;1.257*10^4;2.513*10^4;3.77*10^4;4.819*10^4;5.
152*10^4;6.283*10^4;7.54*10^4;8.796*10^4;1.056*10^5];
[mag,phase] = bode(Gs,Freq);
mag = mag(:); phase = phase(:);

% Experimental valeues in db and degree
Mag_Exp_dB=[0;-0.06912;-0.2525;-0.6835;-2.342;-4.412;-6.614;-
7.225;-9.48;-12.3;-14.81;-17.21];
Phase_Exp_deg=[-0.86;-7.78;-29.2118;-52.42;-104.54;-149.47;-
181.13;-197.05;-223.2;-259.78;-301.54;-353.95];
FreqExp=Freq*60/377; %Convert to Hz

Mag_Model_dB=db(mag);
Phase_Model_deg=phase-720;
```

```
FreqModel=Freq*60/377; %Convert to Hz

% Comparison plot

figure
subplot(2,1,1)
set(gca,'FontSize',16)
  semilogx(FreqExp, Mag_Exp_dB,'--d',FreqModel, Mag_Model_dB,
'r')
  ylabel('Gain [dB]'); xlabel('Freq. [Hz]');grid on

Caxes = copyobj(gca,gcf);
set(Caxes, 'color', 'none', 'xcolor', 'k', 'xgrid', 'off', 'ycol-
or','k', 'ygrid','off');
    subplot(2,1,2)
set(gca,'FontSize',16)
  semilogx(FreqExp,Phase_Exp_deg,'--d',FreqModel,
Phase_Model_deg,'r' )
  ylabel('Phase [Deg]'); xlabel('Freq. [Hz]'); grid on

Caxes = copyobj(gca,gcf);
set(Caxes, 'color', 'none', 'xcolor', 'k', 'xgrid', 'off', 'ycol-
or','k', 'ygrid','off');


%%% difference ( errors)  %%%%%
M_dif=Mag_Model_dB-Mag_Exp_dB;
P_dif=Phase_Model_deg-Phase_Exp_deg;

% percentage
M_dif_error= 100*max(M_dif)/min(Mag_Exp_dB)
P_dif_error= 100*max(P_dif)/min(Phase_Exp_deg)

% error plot  %%

figure
subplot(2,1,1)
set(gca,'FontSize',16)
  semilogx(Freq, M_dif, 'r')
  ylabel('Gain dB'); xlabel('Freq. [rad/sec]'); %grid
subplot(2,1,2)
set(gca,'FontSize',16)
semilogx(Freq,P_dif,'r' )
  ylabel('Phase [Deg]'); xlabel('Freq. [rad/sec]'); %grid


  %%%%%%%% circuit parameters %%%%%%


[r,p,k]=residue(b,a)  % residues and poles
```

```
figure
pzmap(Gs)

c1r=real(r(1,:)); c1im=imag(r(1,:));
c2r=real(r(2,:)); c2im=imag(r(2,:));
c3r=real(r(3,:)); c3im=imag(r(3,:));
c4r=real(r(4,:)); c4im=imag(r(4,:));
c5r=real(r(5,:)); c5im=imag(r(5,:));


p1r=-real(p(1,:)); p1im=-imag(p(1,:));
p2r=-real(p(2,:)); p2im=-imag(p(2,:));
p3r=-real(p(3,:)); p3im=-imag(p(3,:));
p4r=-real(p(4,:)); p4im=-imag(p(4,:));
p5r=-real(p(5,:)); p5im=-imag(p(5,:));

% Circuit elements calculation
H11=2*((c2r*p2r-p1im*c2im)/(p2r^2+p2im^2))
L11=1/(2*p2r)
C11=(2*p2r)/(p2r^2+p1im^2)
H11_2=(c2r)/(p2r)



H22=2*(c4r*p4r-p3im*c4im)/(p4r^2+p4im^2)
L22=1/(2*p4r)
C22=(2*p4r)/(p4r^2+p3im^2)
H22_2=c4r/p4r

H33=c5r/p5r
L33=1/p5r

H44=k


%%%%%%%%%%%%%%%%%%%% transfer function check %%%
[r,p,k]=residue(b,a)
TF1=tf(r(1,:),[1 -p(1,:)])
TF2=tf(r(2,:),[1 -p(2,:)])
TF3=tf(r(3,:),[1 -p(3,:)])
TF4=tf(r(4,:),[1 -p(4,:)])
TF5=tf(r(5,:),[1 -p(5,:)])
TFF=TF1+TF2+TF3+TF4+TF5

TF12=TF1+TF2
TF34=TF3+TF4


%%%%%%%%%%%%%%%%%%%%%%%%%%%%%%%%%%  Results

% Comparison Pspice
```

```
% frequency response circuit model

OCTmodeldata = xlsread('OCT_model_pspice.xls');

octMfreq=OCTmodeldata(:,1);
octMfreq=octMfreq(1:246);


octMamp=OCTmodeldata(:,2);
octMamp=octMamp(1:246);

octMphase=OCTmodeldata(:,3);
octMphase=octMphase(1:246);

%%%%%%BODE PLOT COMPARISON exp, transfer functiom, circuit model
%%
figure
subplot(2,1,1)
set(gca,'FontSize',16)
  semilogx(FreqExp, Mag_Exp_dB,'--d',...
           FreqModel, Mag_Model_dB, '-.r',...
           octMfreq, octMamp,'-k')%,octMfreq_Cad, oct-
Mamp_Cad,'g')
  ylabel('Gain [dB]'); xlabel('Freq. [Hz]');grid on
  legend

  subplot(2,1,2)
set(gca,'FontSize',16)
semilogx(FreqExp,Phase_Exp_deg,'--d',...
         FreqModel, Phase_Model_deg,'-.r',...
         octMfreq, octMphase,'-k') %,octMfreq_Cad,
octMphase_Cad,'g' )
  ylabel('Phase [Deg]'); xlabel('Freq. [Hz]'); grid


 %Errors: exp is base

 %TF
 TFamp_diff=Mag_Model_dB-Mag_Exp_dB;
 TFphase_diff=Phase_Model_deg-Phase_Exp_deg;

 TFamp_error= 100*max(TFamp_diff)/min(Mag_Exp_dB)
 TFphase_error=100*max(TFphase_diff)/min(Phase_Exp_deg)


 %Circuit

 Cramp_diff=-1.273-(-1.52);%manuel found. exp avarge of two
points taken
```

```
 Crphase_diff=-76.57-(-79.14);%manuel found. exp avarge of two
points taken

 Cramp_error= 100*min(Cramp_diff)/min(Mag_Exp_dB)
 Crphase_error=100*min(Crphase_diff)/min(Phase_Exp_deg)

%%%%%%%%%%%%%%%%%%%%

%%%%%% test signal comparison   %%%%%%

  %%%%% Load data%%%%%%
  %Sampling time 1.00E-05

  %exp
input=load('OCTSTEPinput.txt');
output=load('OCTSTEPoutput.txt');
time_exp=load('time_exp_oct.txt');
time_exp=time_exp*10^-5;

%circuit model
circuitout=xlsread('OCTstepCircuitoutput.xls');
time_cr=circuitout(:,1);
crout=circuitout(:,2);

%TF out
Gz=c2d(Gs,0.00001,'tustin')
TFMoutput= lsim(Gz,input);

%Comparison

figure
plot(time_exp,TFMoutput)
hold on
plot(time_exp,output,'m')
plot(time_cr,crout,'--k')

%%% Error based on exp signal
% considering crout=TFMoutput. because crout has more number than
the
% others we can not substract them since the matrix dimensions
are not
% equal.

errorModels=output-TFMoutput;
errorModels=100*max(errorModels)/max(output)

%%%%  END  %%%%%
```

APPENDIX B

DEVELOPMENT OF OPTICAL MODEL FOR OPTICAL CURRENT TRANSFORMER

```
function P = opModelct(I)
%Jones vector
Ex=[1 0]'; % x polarized light
Ey=[0 1]'; % y polarized light

%Faraday rotation angle
V=4.68*10^-6; % Verdet constant of fiber optic cable [rad/A]
N=2; % number of fiber optic cable turns around conductor
Theta=1/2*4*V*N*I; % rotation angle

%Jones matrices
Mq_f=1/sqrt(2)*[1  -i;-i  1]*exp(i*pi/2);  % Forward  quarter  wave
plate
Mcoil_f=[cos(Theta) -sin(Theta);...
             sin(Theta)  cos(Theta)]; % Forward Faraday rotator
Mm=[-1 0;...
     0 1]; % Mirror
Mcoil_b=[cos(Theta) sin(Theta);...
            -sin(Theta) cos(Theta)]; % Back Faraday rotator
Mq_b=1/sqrt(2)*[1 i;i 1]*exp(i*pi/2); % Back quarter wave plate
Mp_y=[0 1]; % Linear polarizer, y
Mp_x=[1 0];% Linear polarizer, y

%Final states of lights

Eyy=Mp_y*Mq_b*Mcoil_b*Mm*Mcoil_f*Mq_f*Ex; % Final state of x po-
larized light
Exx=Mp_x*Mq_b*Mcoil_b*Mm*Mcoil_f*Mq_f*Ey; % Final state of y po-
larized light
P1=angle(Eyy)-angle(Exx); %angle between the two final states of
the lights
P=(I/P1)*1/0.3183; %Normalization (0.3183 is the maximum of P1)
end
```

APPENDIX C

DEVELOPMENT OF MODEL FOR OPTICAL VOLTAGE TRANSFORMER

```
%%%%% Transfer function model development  %%%%%%
clear
clc
%%%%%  Experimental values  %%%%%

        %Hz             %Magnitude        %Phase
Bode = [
        60              1              -0.804
        500             1.003          -10.24
        1000            0.999          -19.86
        2000            1.004          -38.13
        3000            0.983          -57.58
        4000            0.953          -78.57
        5000            0.923          -96.15
        6000            0.890          -113.6
        7000            0.862          -132.2
        8000            0.837          -147.9
        9000            0.816          -166
        9743            0.802          -179.5
        11000           0.776          -199.6
        12000           0.759          -217.1
        13000           0.744          -234.6
        14000           0.730          -252.4
        15000           0.719          -268.99 ];



w     = (2*pi)*Bode(:,1);%rad/sec
mag   = Bode(:,2);
phase = Bode(:,3)*(pi/180);
H = mag .* exp(j*phase);


[b,a] = invfreqs(H,w,4,5,[],50); % TF coefficients
Gs=tf(b,a)%developed TF
figure
bode(Gs)

%%%%%%Bode plot comparison of develeoped TF and exp measurements
%%%%%%%%

% Experimental frequencies applied to TF

Freq_Hz=[60;500;1000;2000;3000;4000;5000;6000;7000;8000;9000;9743
;11000;12000;13000;14000;15000];
Gain=[1;1;0.999;0.995;0.983;0.953;0.923;0.890;0.862;0.837;0.816;0
.802;0.776;0.759;0.744;0.73;0.719];
PhaseExp=[-0.804;-10.24;-19.86;-38.13;-57.58;-78.57;-96.15;-
113.6;-132.2;-147.9;-166;-179.5;-199.6;-217.1;-234.6;-252.4;-
268.99];
%
Freq=2*pi*Freq_Hz ; %rad/sec
```

```
[mag,phase] = bode(Gs,Freq);
mag = mag(:); phase = phase(:);

%%%%%%BODE PLOT COMPARI-
SON%%%%%%%%%%%%%%%%%%%%%%%%%%%%%%%%%%%%%%%%%%%%%%%%%%%%%%%%%%%
% Experimental valeues in db and degree
Mag_Exp_dB=db(Gain);
Phase_Exp_deg=PhaseExp;
FreqExp=Freq*60/377; %Convert to Hz

Mag_Model_dB=db(mag);
Phase_Model_deg=phase-360-360;
FreqModel=Freq*60/377; %Convert to Hz

% Comparison plot
figure

subplot(2,1,1)
set(gca,'FontSize',18)
  semilogx(FreqExp, Mag_Exp_dB,'--d', FreqModel, Mag_Model_dB,
'r','LineWidth',2)
  ylabel('Gain [dB]'); xlabel('Frequency [Hz]');grid on

set(gca,'Xcolor',[0.5 0.5 0.5]);
set(gca,'Ycolor',[0.5 0.5 0.5]);

% Note the the X and Y ticks will be the same color as the grid
lines, if you still want the tick marks black, you can do the
following

Caxes = copyobj(gca,gcf);
set(Caxes, 'color', 'none', 'xcolor', 'k', 'xgrid', 'off', 'ycol-
or','k', 'ygrid','off');

set(gca,'XMinorGrid','off')
h = legend('Experimental','TF Model',2);

  subplot(2,1,2)
set(gca,'FontSize',18)
semilogx(FreqExp,Phase_Exp_deg,'--d', FreqModel,
Phase_Model_deg,'r','LineWidth',2 )
  ylabel('Phase [Deg]'); xlabel('Frequency [Hz]');grid on


set(gca,'Xcolor',[0.5 0.5 0.5]);
set(gca,'Ycolor',[0.5 0.5 0.5]);

% Note the the X and Y ticks will be the same color as the grid
lines, if you still want the tick marks black, you can do the
following
```

```
Caxes = copyobj(gca,gcf);
set(Caxes, 'color', 'none', 'xcolor', 'k', 'xgrid', 'off', 'ycol-
or','k', 'ygrid','off');

set(gca,'XMinorGrid','off')
h = legend('Experimental','TF Model',5);

%%% difference ( errors)  %%%%%
 M_dif=Mag_Model_dB-Mag_Exp_dB;
 P_dif=Phase_Model_deg-Phase_Exp_deg;
 % percentage
 M_dif_error= 100*min(M_dif)/min(Mag_Exp_dB)
 P_dif_error= 100*max(P_dif)/min(Phase_Exp_deg)

% error plot  %%
figure
subplot(2,1,1)
set(gca,'FontSize',16)
  semilogx(Freq, M_dif, 'r')
  ylabel('Gain [dB]'); xlabel('Freq. [rad/sec]'); %grid
subplot(2,1,2)
semilogx(Freq,P_dif,'r' )
  ylabel('Phase [Deg]'); xlabel('Freq. [rad/sec]'); %grid

%%%%%%%%%%%%%%%%%%%%%%%%
 %%%%%%%% circuit parameters %%%%%%

[r,p,k]=residue(b,a)% residues and poles

figure
pzmap(Gs)

c1r=real(r(1,:)); c1im=imag(r(1,:));
c2r=real(r(2,:)); c2im=imag(r(2,:));
c3r=real(r(3,:)); c3im=imag(r(3,:));
c4r=real(r(4,:)); c4im=imag(r(4,:));
c5r=real(r(5,:)); c5im=imag(r(5,:));


p1r=-real(p(1,:)); p1im=-imag(p(1,:));
p2r=-real(p(2,:)); p2im=-imag(p(2,:));
p3r=-real(p(3,:)); p3im=-imag(p(3,:));
p4r=-real(p(4,:)); p4im=-imag(p(4,:));
p5r=-real(p(5,:)); p5im=-imag(p(5,:));

% Circuit elements calculation
H11=c1r/p1r
L11=1/p1r

H55=c4r/p4r
L55=1/p4r
```

```
H66=c5r/p5r
L66=1/p5r

H22=2*((c3r*p3r-p2im*c3im)/(p3r^2+p3im^2))
L11=1/(2*p3r)
C11=(2*p3r)/(p3r^2+p2im^2)
H22_2=(c3r)/(p3r)

%%%%%%%%%%%%%%%%%%%% transfer function check %%%

TF1=tf(r(1,:),[1 -p(1,:)])
TF2=tf(r(2,:),[1 -p(2,:)])
TF3=tf(r(3,:),[1 -p(3,:)])
TF4=tf(r(4,:),[1 -p(4,:)])
TF5=tf(r(5,:),[1 -p(5,:)])
TFF=TF1+TF2+TF3+TF4+TF5

TF1
TF23=TF2+TF3
TF45=TF4+TF5

%%%%%%%%%%%%%%%%%%%%%%%%%%%%%%%%  Results

% Comparison Pspice

% frequency response circuit model
OVTmodeldata = xlsread('OVT_model_pspice.xls'); %OVT_model_pspice
ovtMfreq=OVTmodeldata(:,1);
ovtMfreq=ovtMfreq(1:241);
%ovtMfreq=ovtMfreq*377/60;

ovtMamp=OVTmodeldata(:,2);
ovtMamp=ovtMamp(1:241);



ovtMphase=OVTmodeldata(:,3);
ovtMphase=ovtMphase(1:241);

%%%%%%BODE PLOT COMPARI-
SON%%%%%%%%%%%%%%%%%%%%%%%%%%%%%%%%%%%%%%%%%%%%%%%%%%%%%%%%

figure
subplot(2,1,1)
set(gca,'FontSize',16)
  semilogx(FreqExp, Mag_Exp_dB,'--d',FreqModel, Mag_Model_dB,
'r',ovtMfreq, ovtMamp,'k')%,ovtMfreq_Cad, ovtMamp_Cad,'--g')
  ylabel('Gain [dB]'); xlabel('Freq. [Hz]');grid on


  subplot(2,1,2)
```

```
set(gca,'FontSize',16)
semilogx(FreqExp,Phase_Exp_deg,'--d',FreqModel,
Phase_Model_deg,'r',ovtMfreq, ovtMphase,'k')%,ovtMfreq_Cad, ovtM-
phase_Cad,'--g' )
  ylabel('Phase [Deg]'); xlabel('Freq. [Hz]'); grid

%%%%%%%%%%%%%%%%%%%%

 CM_dif= -1.917-(-1.958);
 CP_dif= -4.375-(-6.504);

 M_dif_error= 100*min(CM_dif)/min(Mag_Exp_dB)
 P_dif_error= 100*max(CP_dif)/min(Phase_Exp_deg)

%%%%%%%%%%%%%%%%%%%%%%%%%%%%%
%%%%%% test signal comparison   %%%%%%
%Sample Interval    1.00E-07

%%%%% Load data%%%%%%

%%% exp
input=load('Vinput.txt');
output=load('Voutput.txt');
time_exp=load('time_exp_ovt.txt');
time_exp=time_exp;


%%% circuit model
circuitout=xlsread('OVTresult_pspice.xls');
time_cr=circuitout(:,1);
crout=circuitout(:,2);

%Tf output
Gz=c2d(Gs,1.00E-07,'tustin')
Moutput= lsim(Gz,input);

%comparison
figure
plot(time_exp,Moutput)
hold on
plot(time_exp,output,'m')
plot(time_cr,crout,'--k')


err=6.55-5.32;
err=100*err/max(5.88)
%%%%%%%%%%%%%%%%%%%%%%%%%%%%%%%%%%%%
%%%%  END  %%%%%
```

APPENDIX D

DEVELOPMENT OF OPTICAL MODEL FOR OPTICAL VOLTAGE TRANSFORMER

```
function P = opModelvt_E(V)

%Jones vector of circular polarized light
Ec=1/sqrt(2)*[1;i];

%Volategs accross the crystals based on their locations
V1=V*1.232/1.525;
V2=V*0.748/1.525;
V3=V*0.206/1.525;

%rotation in Poeckels cell
alpha1=1/(240)*pi*V1*10^-4;
alpha2=1/(240)*pi*V2*10^-4;
alpha3=1/(240)*pi*V3*10^-4;

%Jones matrices of Pockels cells
Mpockel1=[cos(alpha1/2) i*sin(alpha1/2);...
         i*sin(alpha1/2)  cos(alpha1/2)];
%
Mpockel2=[cos(alpha2/2) i*sin(alpha2/2);...
         i*sin(alpha2/2)  cos(alpha2/2)];

Mpockel3=[cos(alpha3/2) i*sin(alpha3/2);...
         i*sin(alpha3/2)  cos(alpha3/2)];

%Final states of three lights
E1=Mpockel1*Ec;
E2=Mpockel2*Ec;
E3=Mpockel3*Ec;

%Intensities of each light
E1oxH=transpose(conj(E1(1,:)));
E1oyH=transpose(conj(E1(2,:)));
U1=(E1oxH-E1oyH)/(E1oxH+E1oyH);

E2oxH=transpose(conj(E2(1,:)));
E2oyH=transpose(conj(E2(2,:)));
U2=(E2oxH-E2oyH)/(E2oxH+E2oyH);

E3oxH=transpose(conj(E3(1,:)));
E3oyH=transpose(conj(E3(2,:)));
U3=(E3oxH-E3oyH)/(E3oxH+E3oyH);

%Final intensity
P1=-(U1+U2+U3);

%Normalization
P=P1/(1.8756*10^-6); %1.8756*10^-6 is the maximum of P1
end
```